Doctoral Thesis

Synthesis of Dimensional Organic Networks as Energy Materials

Seok-Jin Kim

Department of Energy Engineering

Graduate School of UNIST

2019

Synthesis of Dimensional Organic Networks as Energy Materials

Seok-Jin Kim

Department of Energy Engineering

Graduate School of UNIST

Synthesis of Dimensional Organic Networks as Energy Materials

A thesis/dissertation

submitted to the Graduate School of UNIST

in partial fulfillment of the

requirements for the degree of

Doctor of Philosophy

Seok-Jin Kim

06/12/2019 of submission

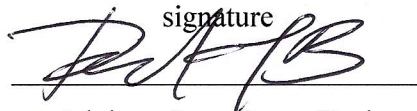Approved by
_____

Advisor

Jong-Beom Baek

Synthesis of Dimensional Organic Networks as Energy Materials

Seok-Jin Kim

This certifies that the thesis/dissertation of Seok-Jin Kim is approved.
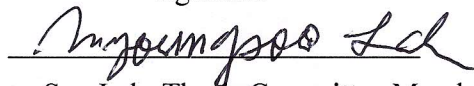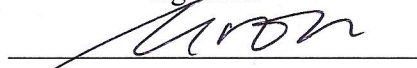
06/12/2019 of submission

signature

Advisor: Jong-Beom Baek

signature

Myoung Soo Lah: Thesis Committee Member #1

signature

Hoi Ri Moon: Thesis Committee Member #2

signature

Guntae Kim: Thesis Committee Member #3

signature

In-Yup Jeon: Thesis Committee Member #4;

Abstract

The study of chemical structure is crucial in chemistry and materials science. Materials structure can be classified in various ways, and the most familiar approach is to classify them according to the dimension of structure. For example, carbon composed of the same elements can be categorized into zero-dimensional (0D) fullerene, one-dimensional (1D) carbon nanotube, two-dimensional (2D) graphene, and three-dimensional (3D) diamond, but due to particular arrangements of atoms the properties are significantly different depending on the structural dimension. Bearing this in mind, many organic structures were created by designing the symmetry of the molecules and using the polymerization to control the size of the structure (bottom-up strategy). The synthesized organic structures showed applicability to various applications such as gas separation, storage, membrane, and catalysis, etc. depending on the structural dimension. However, covalently bonded organic structures are limited in some areas because they are thermally unstable and have low conductivity. This thesis presents the results of applying a fully-fused aromatic networks (FANs) structure to energy materials to overcome the aforementioned limitations. The fused-ring has no free torsional motion, allowing stable electron transfer and providing thermal and chemical stability. By using these properties, the iron particles were encapsulated in the 2D structure, which showed excellent activity as a semi-permanent oxygen reduction catalyst and the 3D structure exhibited high hydrogen storage with excellent thermal stability. In addition, a new type of 2D structure that introduces insights into how to design materials in organic structures for gas separation and storage. Based on these studies, it is shown that FANs can be a promising material for electrochemical catalysts, gas storage, separation by using advantage of excellent electron mobility and thermochemical stability. Furthermore, I also studied carbon material as a catalyst having excellent activity and good stability in the conversion of ethylbenzene into styrene.

I

Table of Contents

III

List of Figures

in air (solid line), in nitrogen (dot line). (b) in air, Fe@Aza-PON (dark red): The residual char yield of 27.70 wt% at 600 °C, which was associated with iron oxide (Fe_2O_3) and the corresponding amount of Fe is 19.39 wt%; Fe@TAB (dark blue): The residual char yield of 13.72 wt% and pure Fe is 9.06 wt%.

Figure 2.8. XPS spectra of Fe@Aza-PON. (a) Survey spectrum; inset is deconvoluted O 1s spectra. (b) C 1s spectra.

Figure 2.9. Nitrogen adsorption-desorption isotherms at 77 K. (a) Fe@Aza-PON-BH before heat-treatment. (b) Fe@Aza-PON after heat-treatment. Inset: pore size distribution was calculated by NLDFT.

Figure 2.10. (a, b) SEM images of Fe@Aza-PON at different magnification.

Figure 2.11. Schematic representation of the synthesis of Fe@TAB.

Figure 2.12. HR-TEM images of Fe@TAB. (a-f) Most of Fe particles are leached off by acid treatment (dark red arrows).

Figure 2.13. Electrochemical ORR performance in 0.1 M aq. KOH. (a) Rotating ring-disk electrode (RRDE) polarized curves recorded with Fe@Aza-PON, Pt/C and Fe@TAB (red: Fe@Aza-PON, black: Fe@TAB, blue: Pt/C) (b) Tafel plot, (c) the test for catalytic stability and (d) result for methanol poisoning.

Figure 2.14. Study of elemental composition changes and dependence of electrocatalytic performance on annealing temperature. (a) Element contents of Fe@Aza-PON with respect to annealing temperatures. Inset is a numerical percentage of each element. (b) XPS spectra of Fe@Aza-PON with respect to annealing temperatures. Inset: numerical percentage of each element. (c) CV curves of samples annealed at different temperatures in 0.1 M aq. KOH Condition (catalyst loading: 20 μg, scan rate: 10 mV s^{-1}). (d) Average onset potential *vs.* annealing temperature plots after three measurements (dark red dot).

Figure 2.15. Rotating ring-disk electrode (RRDE) voltammograms recorded with Fe@Aza-PON, Pt/C and Fe@TAB in 0.1 M aq. $HClO_4$ solution. (a) LSV curves. (b) Tafel plots (each 30 μg of catalyst amount is loaded, scan rate: 10 mV s^{-1} at 1600 rpm).

Figure 2.16. The electron transfer number with HO_2^- (or H_2O_2) concentration for Fe@Aza-PON, Fe@TAB, and Pt/C. (a) 0.1 M aq. KOH. (b) 0.1 M aq. $HClO_4$ (scan rate: 10 mV s^{-1}).

Figure 2.17. Current retention with respect to chronoamperometric cycling 0.1 M aq. $HClO_4$ solution. Inset: 100 000 cycles of Fe@Aza-PON (scan rate: 100 mV s^{-1}).

Figure 2.18. Rotating ring-disk electrode (RRDE) voltammograms after 10,000 cycles in both aq. KOH (0.1 M) and aq. $HClO_4$ (0.1 M) solutions. (a, c) LSV curves of Fe@Aza-PON. (b, d) LSV curves of

List of Tables

Nomenclature

0D	zero-dimensional
1D	one-dimensional
2D	two-dimensional
3D	three-dimensional
BET	Brunauer-Emmett-Teller
CMP	conjugated microporous polymer
CNT	carbon nanotube
COF	covalent organic framework
CON	cage-like organic network
CP/MAS	cross-polarization/magic angle spinning
DH	dehydrogenation
DMF	N,N-dimethylformamide
DOE	department of energy
DPDS	N,N'-(4,5-diamino-1,2-phenylene)dibenzenesulfonamide
DPH	diquinoxalino[2,3-a:2',3'-c]phenazine-2,3,8,9,14,15-hexaamine
DPHS	diquinoxalino[2,3-a:2',3'-c]phenazine-2,3,8,9,14,15-hexayl-hexabenzenesulfonamide
EA	elemental analysis
EB	ethylbenzene
EDX	energy-dispersive X-ray spectroscopy
FAN	fully-fused aromatic network
FFT	fast Fourier transform
FT-IR	Fourier transform infrared
GnPs	graphene nanoplatelets
HATN-HA	hexaazatrinaphthylene hexamine
HCP	hyper-cross-linked polymer
HKH	hexaketocyclohexane octahydrate
HOR	hydrogen oxidation reaction
IAST	ideal adsorbed solution theory
MOF	metal-organic framework

NLDFT	nonlocal density functional theory
ODH	oxidative dehydrogenation
OER	oxygen evolution reaction
OPM	organic porous material
ORR	oxygen reduction reaction
POF	porous organic framework
PON	porous organic network
PPM	porous polymeric material
PSA	pressure swing adsorption
RDE	rotating disk electrode
RRDE	Rotating ring-disk electrode
SEM	scanning electron microscopy
ST	styrene
TAB	tetraaminobenzene
TEM	transmission electron microscopy
TGA	thermogravimetric analysis
THA	triptycenehexaamine
XPS	X-ray photoelectron spectroscopy
XRD	X-ray diffraction

I. Synthesis of hexaazatrinaphthylene hexaamine: Potential candidate for functional organic materials

1.1 Abstract

C_3-symetric molecules with tri- and hexaamino functional groups have been an important building blocks for the synthesis of functional organic materials. However, large molecules containing mutifunctional amino groups are difficult to synthesize. Here, we report a facile method for the synthesis of diquinoxalino[2,3-a:2',3'-c]phenazine-2,3,8,9,14,15-hexaamine (DPH) in good yield. DPH can be useful for the synthesis of a variety of π-conjugated robust organic frameworks for gas storages, organic opto-electronics and catalysis.

1.2 Introduction

The C_3-symmetric hexaazatrinaphthylene molecule is an important building block for the synthesis of polynitrogenated heteocyclic systems[1] and covalent organic frameworks (COFs),[2-6] which can be used in gas storages,[7] opto-electronics,[8,9] and catalysis.[10] As crystalline network structures, extended conjugated hexaazatrinaphthylene hexamine (HATN-HA), which has C_3-symetry, could be utilized for the fabrication of two-dimensional (2D) COFs with new interesting properties.[11,12] The HATN-HA has rigid 2D structure and is advantageous in the synthesis of robust 2D COFs.[12,13]

The phenazine based diamine unit has been used to synthesize a variety of functional moieties, such as discotic liquid crystals,[14] pyrazine-containing acene-type molecular ribbons,[15] and amine-derived hexaazatrinaphthylenes.[16] Although it has been reported that the HATN-HA,[16] its detailed synthetic procedure and analyses have not been separately reported later. The HATN-HA is a potentially important substance as a building block for the synthesis of star-shaped quantum size molecules, conjugated 2D COFs and organogelators.[17] Hence, the synthesis of HATN-HA is of high interest for the researchers in the materials synthesis.

The *ortho*-diamino groups of HATN-HA can spontaneously react with keto groups to form fused aromatic rings such as quinoxilines,[18] benzimidazoles,[19] and benzotriazoles,[20] as well as coordinate with transition metals to yield 2D metal-organic frameworks (MOFs).[21] In this report, we introduce a new synthetic protocol for specific C_3-symmetric HATN-HA, diquinoxalino[2,3-a:2',3'-c]phenazine-2,3,8,9,14,15-hexaamine (DPH), which has hexaamino groups (three *ortho*-diamino groups).

The synthetic process starts with the protection of the 1,2-diaminobenzene[22] with benzenesulfonyl chloride in pyridine. The protected diaminobenzene (**1**) was nitrated using nitric acid (HNO$_3$) in acetic acid to give N,N'-(4,5-dinitro-1,2-phenylene)dibenzenesulfonamide (**2**).[23] The hydrogenation of (**2**) in the presence of palladium on activated carbon (Pd/C) to give N,N'-(4,5-diamino-1,2-phenylene)dibenzenesulfonamide (**3**).[24] This protected tetraamine (**3**) was reacted with

hexaketocyclohexane octahydrate (HKH) in acetic acid under nitrogen atmosphere to quantitatively afford benzenesulfonamide protected DPH (**4**, DPHS)[25] in pure form (**Figure 1.1**). The obtained DPHS was in greenish powder. Interestingly, the color change was obserevd after dissolution in different solvents, due to the interaction of DPHS with solvent molecule varies the length of π–conjugation. The SDPH was de-protected in concentrated sulfuric acid (H_2SO_4) at ambient temperature for 24 hours. After neutralizing crude product with 10% aq. potassium carbonate and washing with deoxygenated deionized water,[26] it recrystallized from dimethyformamide DMF/water mixture. Proton nuclear magnetic resonance (^{1}H-NMR) shows strong water peak due to its hygroscopic nature of final DPH.
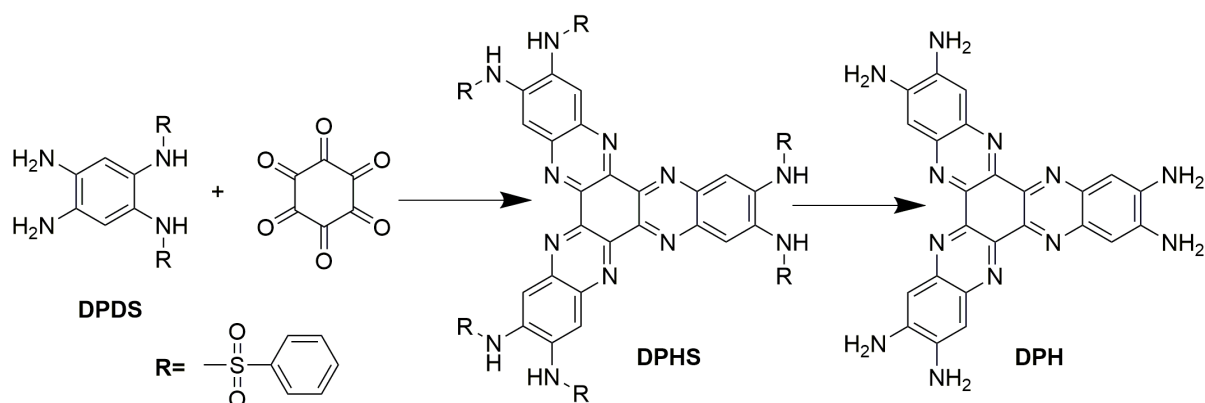
Figure 1.1. The synthesis scheme of DPH. (a) DPDS react with hexaketocyclohexane in the acetic acid solution, refluxed, 16 h, 90.5% of DPHS. (b) DPHS be stirred in concentrated sulfuric acid, 24 h, 93% of DPH.

The UV-vis spectrum of DPH in *N,N*-dimethylformamide (DMF) (left inset, **Figure 1**) shows the π-π* transition bands centered at 477 nm (**Figure 1.2**). When the solution was excited by UV lamp (350 nm), the strong photoluminescent (PL) peak was appeared at 530 nm, which corresponds to green color (right inset, **Figure 1.2**)

DPH is expected to have potential utility in the synthesis of discotic liquid crystals,[27] materials with low barrier to electron and hole transport for the possible application in organic electronics,[28] synthesis of macrocyclic structures,[29] donor-acceptor based organic materials, expanded conjugated electron deficient systems,[30] fluorescence sensors for heavy metals.[31] In addition, we expect that DHP can be extended to the formation of 2D COFs for various applications.[12,32,33]

In summary, we report the straight forward synthesis of *C₃*-symmetric hexaazatrinaphthylene hexamine (HATN-HA), specifically diquinoxalino[2,3-a:2',3'-c]phenazine-2,3,8,9,14,15-hexaamine (DPH), in good yield. We strongly believe that our versatile method for DPH will be highly useful step toward the synthesis of various functional materials.
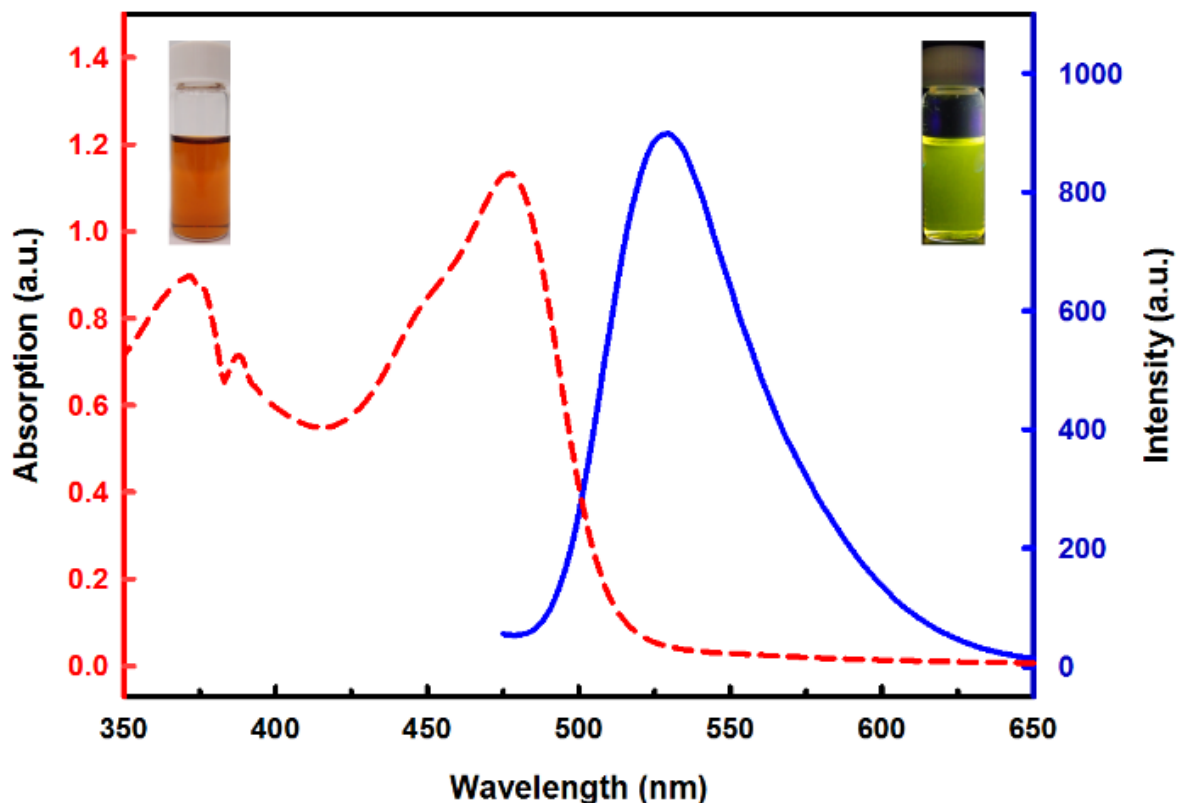
Figure 1.2. UV-vis spectra and PL spectra of DPH in DMF solvent at 25°C. The PL spectra is measured under 350 nm excitation energy.

1.3 Materials

All the reactions were maintained under inert (nitrogen, 99.999%) atmosphere. All the solvents, chemicals and reagents were purchased from Aldrich Chemical Inc., unless otherwise stated.

1.4 Synthesis procedure & analysis results from DPDS to DPH

1.4.1 N,N'-(4,5-diamino-1,2-phenylene)dibenzenesulfonamide (DPDS).

N,N'-(4,5-Dinitro-1,2-phenylene)dibenzenesulfonamide (7.2 g, 15 mmol) was placed in pressure bottle containing ethyl acetate (100 ml) with Pd/C (70 mg). The bottle was mounted on the hydrogenation apparatus and agitated under H_2 atmosphere (60 psi) for 24 h. After the completion of the reaction, Pd/C was filtered through pad of Celite and the filtrate was dried to afford DPDS powder in quantitative yield (98%). ^{1}H NMR (400 MHz, DMSO-d6) δ 4.52 (s,2H), 6.13 (s,1H),7.52 (t,2H), 7.62 (t,3H), 8.57 (s,1H); ^{13}C NMR δ 123.47, 125.94, 126.82, 128.30, 129.66, 133.25, 138.96. MS (MALDI-TOF): m/z (%) = 418 (17) [M][+], 218 (100) Anal. Calcd for $C_{18}H_{18}N_4O_4S_2$: C, 51.66; H, 4.34; N, 13.39; S, 15.32; O, 15.29. Found: C, 51.00; H, 4.34; N, 12.53; S, 15.49 (**Figure 1.3**).
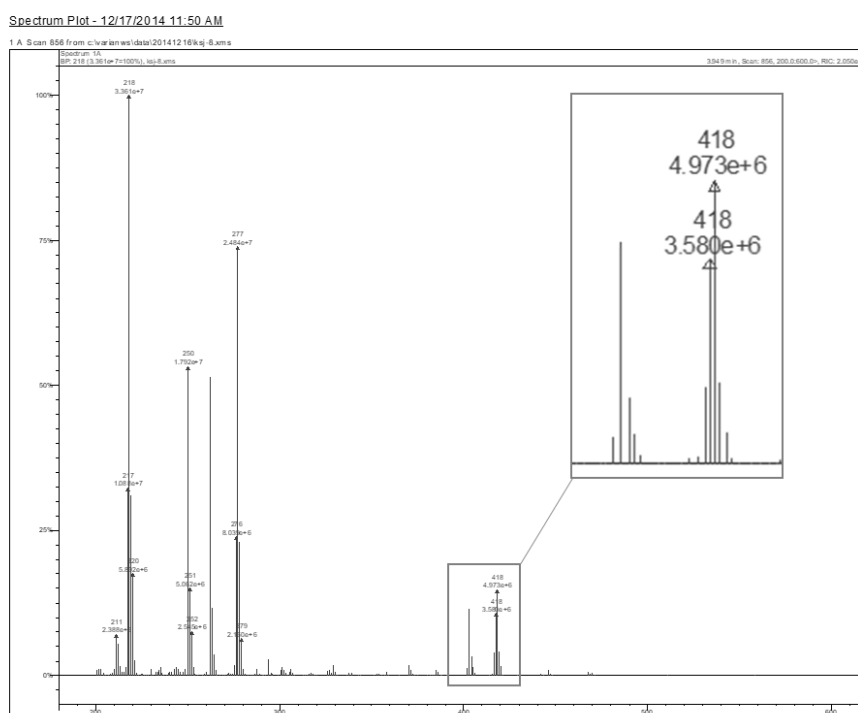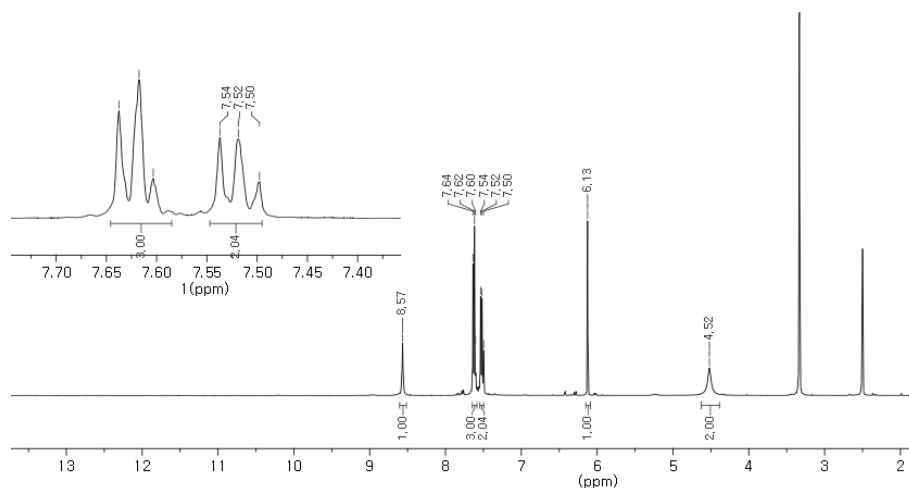
Figure 1.3. ^{1}H NMR (top), MALDI-TOF MS spectrum (bottom) of DPDS.

1.4.2   Diquinoxalino[2,3-a:2',3'-c]phenazine-2,3,8,9,14,15-hexayl-hexabenzenesulfonamide (DPHS).

4,5-Diamino-1,2-phenylene-dibenzenesulfonamide   (2.10   g,   5.0   mmol,   ~3   eq.)   and hexaketocyclehexane octahydrate (0.50 g, 1.60 mmol) was placed in three-necked round bottom flask containing deoxygenated acetic acid (45 mL). The mixture was heated under reflux for 16 h. After cooled to room temperature, the mixture was poured into the cold water. The powdery precipitates were collected by filtration. The air-dried solids were dissolved again in warm ethanol containing charcoal and the solution was filtered while it is warm. The product was filtered and dried in the vacuum oven overnight at 70 °C. (90.5 % yield) ^{1}H NMR (400 MHz, DMSO-d$_6$) δ 7.61 (m,2H), 7.67 (m,1H),7.92

4

(m,2H), 7.97 (m,1H); ^{13}C NMR δ 118.24, 126.93, 129.69, 133.69, 134.40, 138.92, 139.66, 143.05; MS (MALDI-TOF): m/z (%) = 1317 (100) [M+1]$^+$, Anal. Calcd for $C_{60}H_{42}N_{12}O_{12}S_6$: C, 54.79; H, 3.22; N, 12.78; S, 14.62; O, 14.60. Found: C, 53.90; H, 3.35; N, 12.53; S, 14.86; O, 13.05 (**Figure 1.4**).
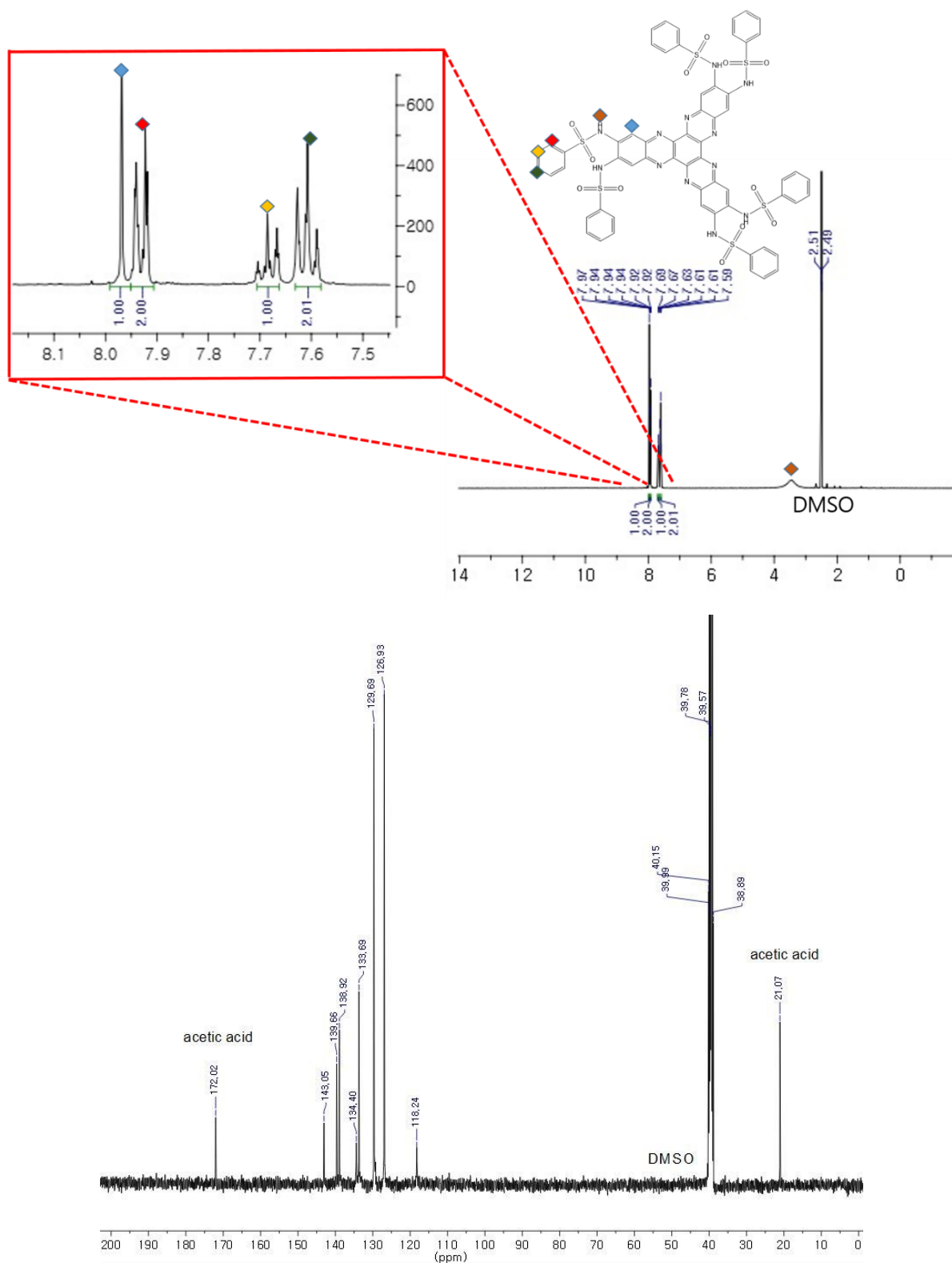
Figure 1.4. ^{1}H NMR (top), ^{13}C NMR (bottom) and MALDI-TOF MS spectrum of DPHS (MALDI-TOF MS is on the next page).

5
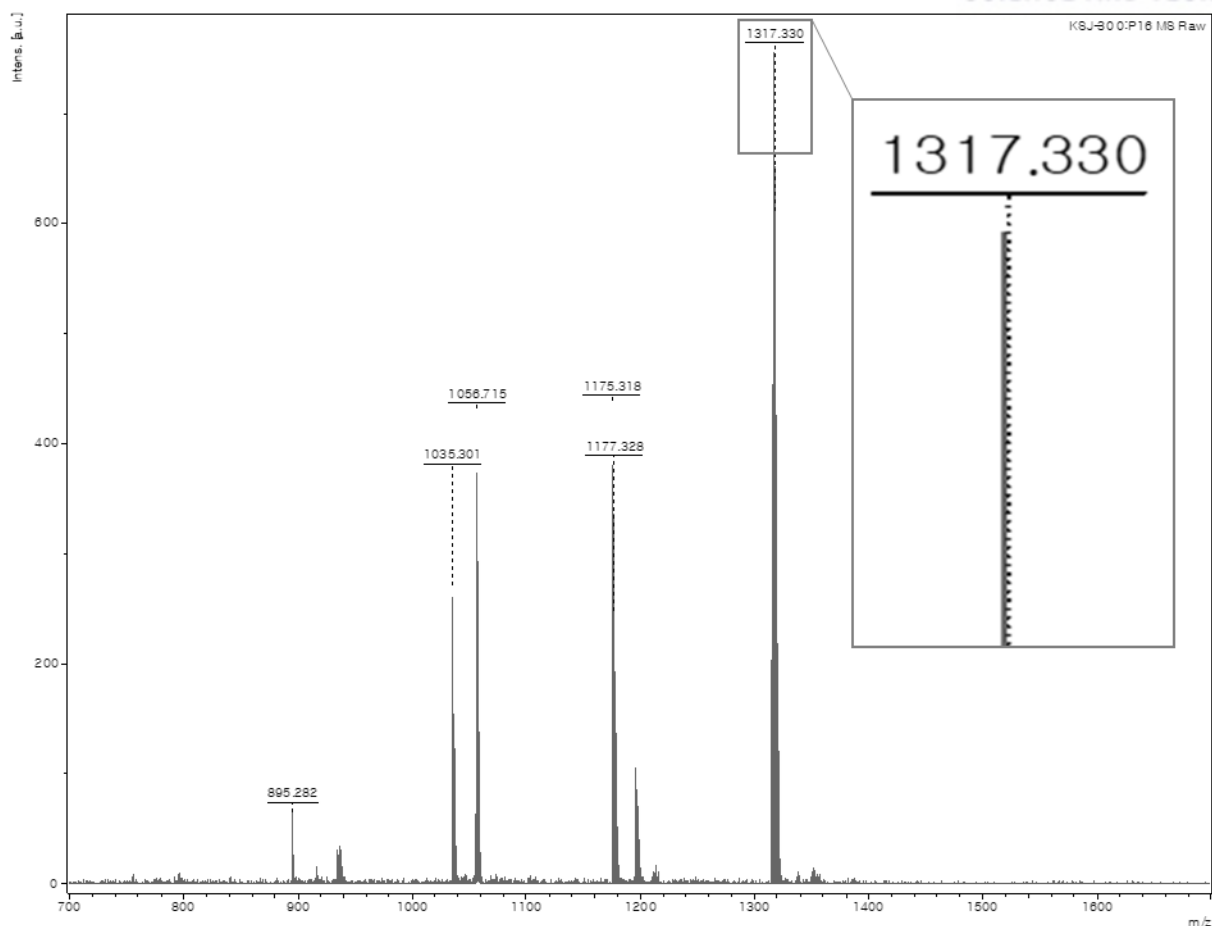
1.4.3 Diquinoxalino[2,3-a:2',3'-c]phenazine-2,3,8,9,14,15-hexaamine (hexaazatrinaphth- ylene hexamine) (DPH)

Diquinoxalino[2,3-a:2',3'-c]phenazine-2,3,8,9,14,15-hexayl-hexabenzenesulfonamide (1.0 g, 0.76 mmol) and concentrated H_2SO_4 (22 mL) were placed one-neck round bottom flask and stirred at room temperature for 24 h. The mixture was poured into ice (700 g). The precipitates were collected by filtration. The product was dispersed in 10% aq. potassium carbonate solution and stirred for 1 h. Then, the product was collected by filtration and repeatedly washed with deoxygenated deionized water (93% yield) ^{1}H NMR (400 MHz, DMSO-d_6) δ 6.12 (s,12H), 7.21 (s,6H); ^{13}C NMR δ 104.61, 138.78, 139.80, 142.91. MS (MALDI-TOF): m/z (%) = 475 (100) [M+1]$^+$. HRMS (ESI) m/z: [M+Na]$^+$ Calcd for $C_{24}H_{18}N_{12}Na$ 497.1675; Found 497.1671. Anal. Calcd for $C_{24}H_{18}N_{12} \cdot 3H_2O$: C, 54.54; H, 4.58; N, 31.80. Found: C, 54.41; H, 4.28; N, 30.66 (**Figure 1.5**).
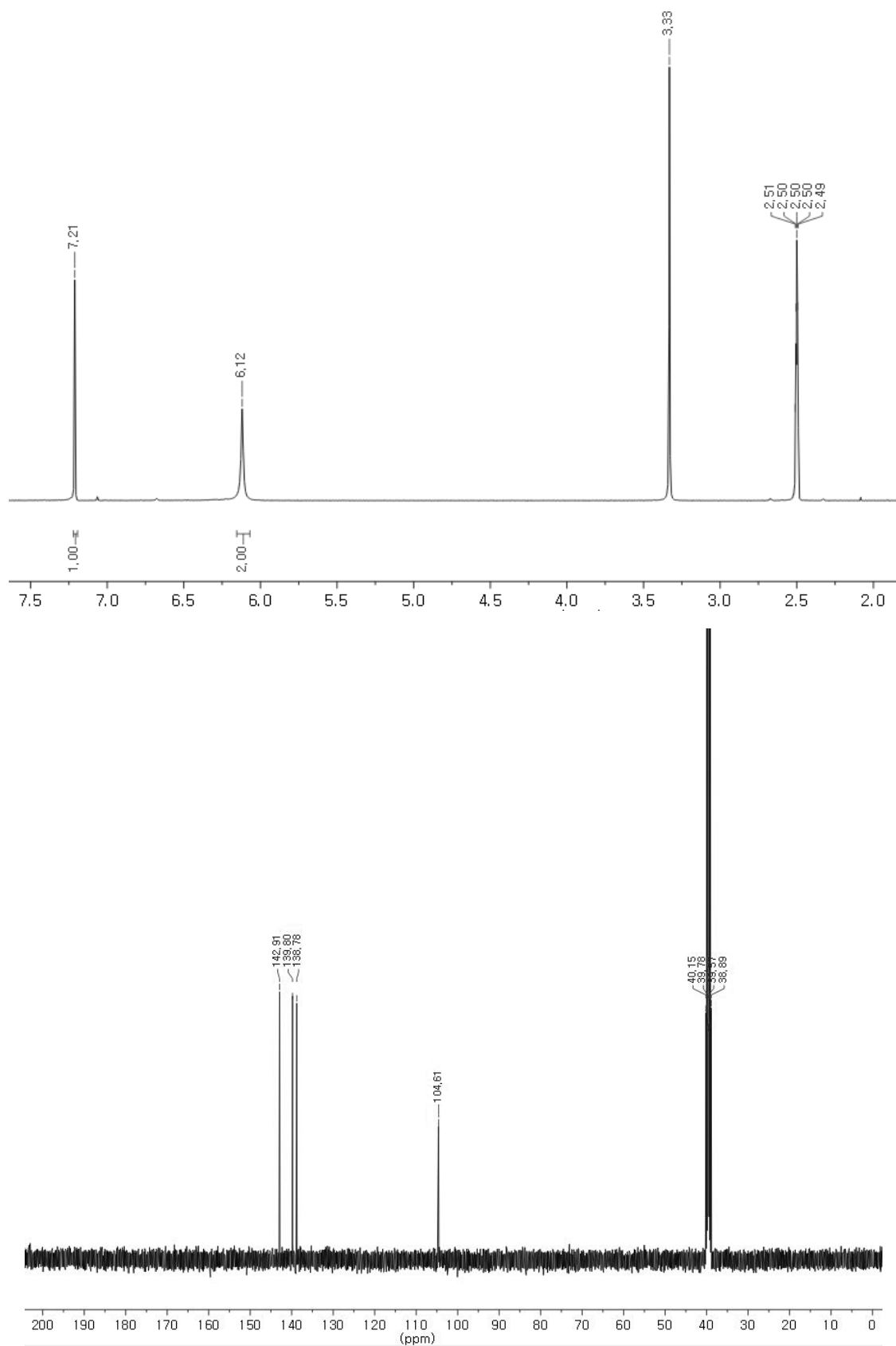
Figure 1.5. ^{1}H NMR (top), ^{13}C NMR (bottom) and MALDI-TOF MS spectrum of DPH (MALDI-TOF MS is on the next page).

7
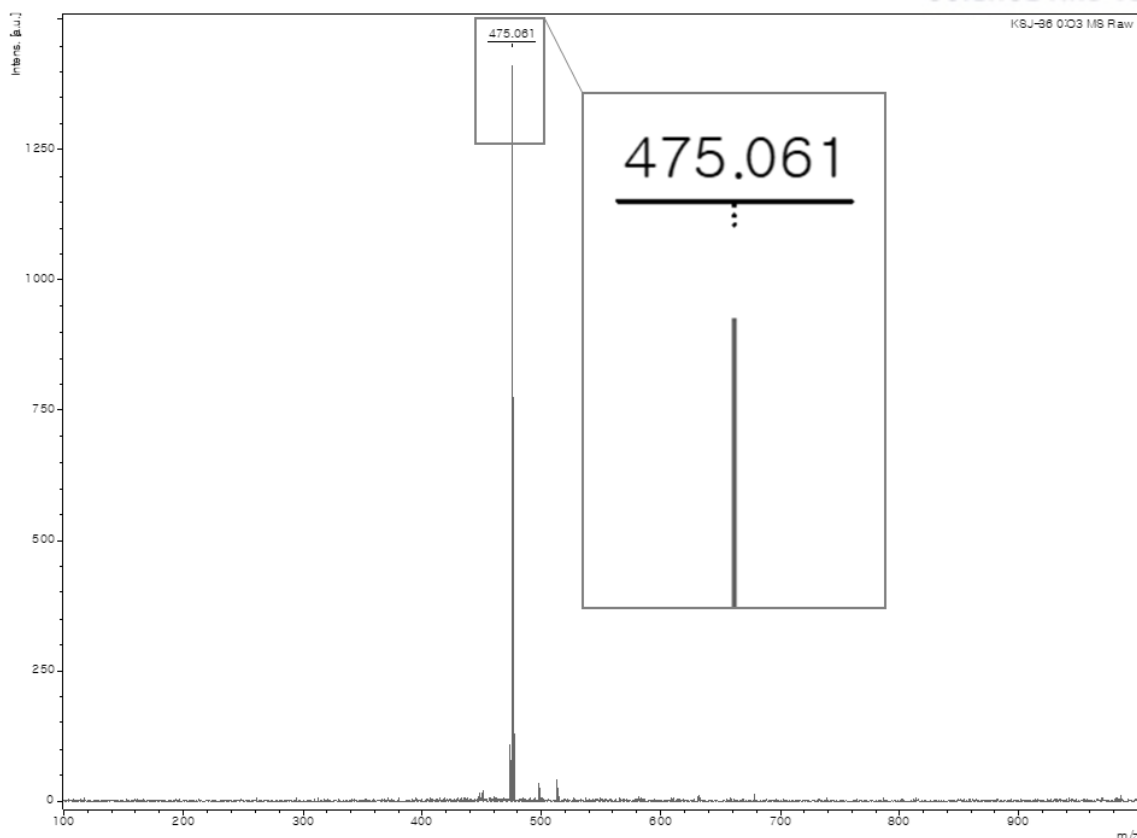
1.5 Synthetic procedure for DPDS preparation
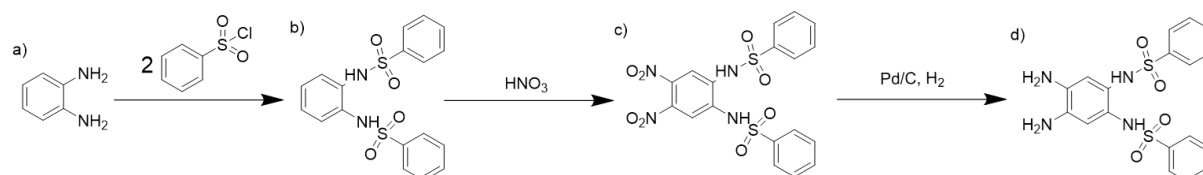
Figure 1.6. Scheme of synthesis DPDS (a) benzene-1,2-diamine. (b) N,N'-(1,2-phenylene)dibenzenesulfonamide. (c) N,N'-(4,5- dinitro -1,2-phenylene)dibenzenesulfonami- de. (d) N,N'-(4,5- diamino -1,2-phenylene)dibenzenesulfonamide.

1.5.1 N,N'-(1,2-phenylene)dibenzenesulfonamide

1,2-diaminobezene (20 g, 185 mmol) dissolved in pyridine (70 ml). The solution was added slowly to pyridine solution containing bezenesulfonyl chlroride (50 ml, 400 mmol). The mixture reacted for 5 hours under 100 ℃. Pour into water and recrystallize with ethanol. (96% yield)

^{1}H NMR (400 MHz, DMSO-d$_6$) δ 7.00 (m,2H), 7.53 (m,2H),7.61 (m,2H), 7.74 (m,2H), 9.39 (s,1H); ^{13}C NMR δ 123.47, 125.94, 126.82, 128.30, 129.66, 133.25, 138.96. MS (MALDI-TOF): m/z (%) = 388 (87) [M]$^+$, 247 (100) Anal. Calc. For C$_{18}$H$_{16}$N$_2$O$_4$S$_2$: C, 55.66; H, 4.15; N, 7.21; S, 16.51; O, 16.47; Found: C, 55.60; H, 4.15; N, 7.22; S, 16.73 (**Figure 1.7**).

N,N'-(1,2-phenylene)dibenzenesulfonamide
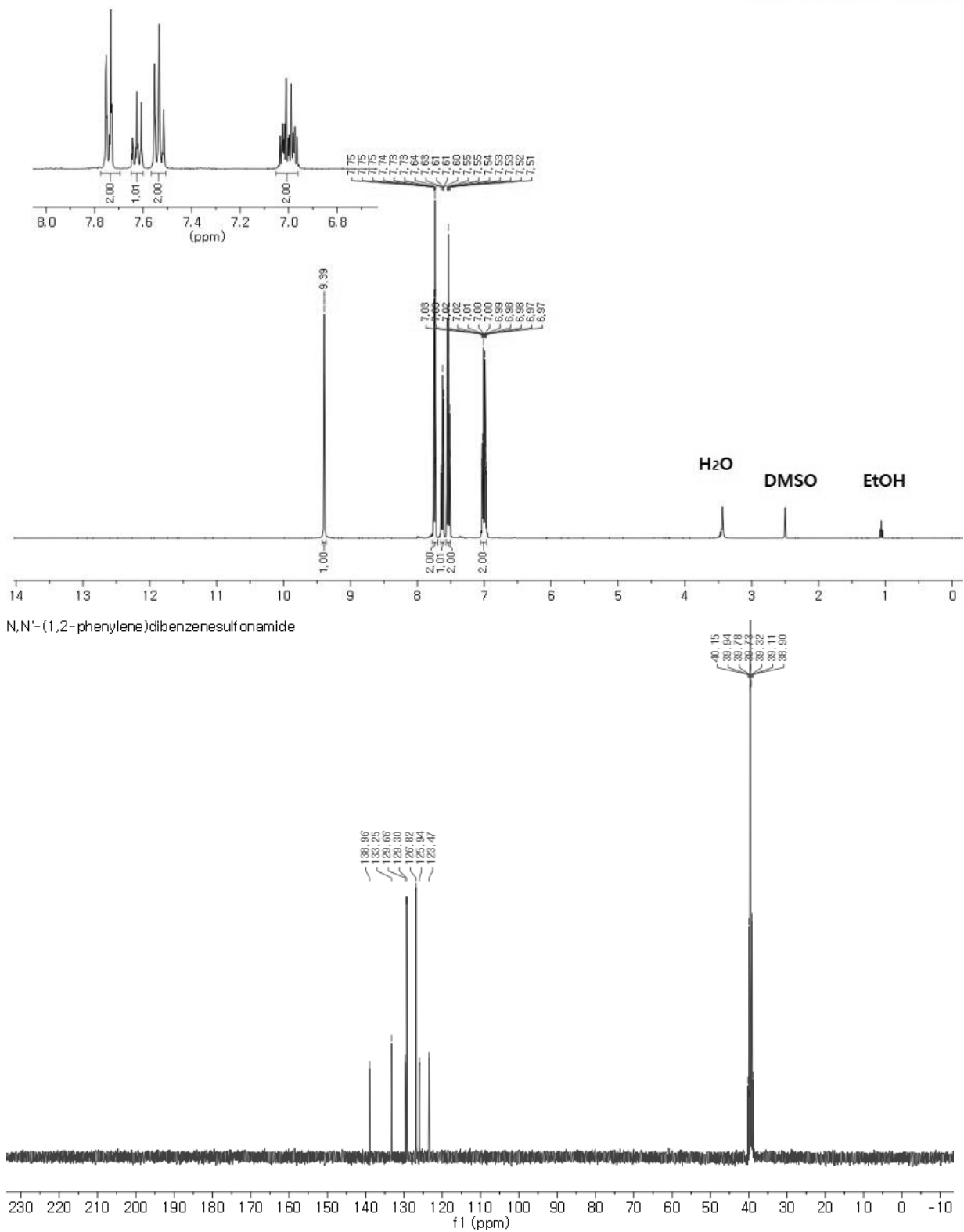
Figure 1.7. ^{1}H NMR (top), ^{13}C NMR and MALDI-TOF MS spectrum of DPDS (MALDI-TOF MS is on the next page).

Spectrum Plot - 12/17/2014 11:48 AM
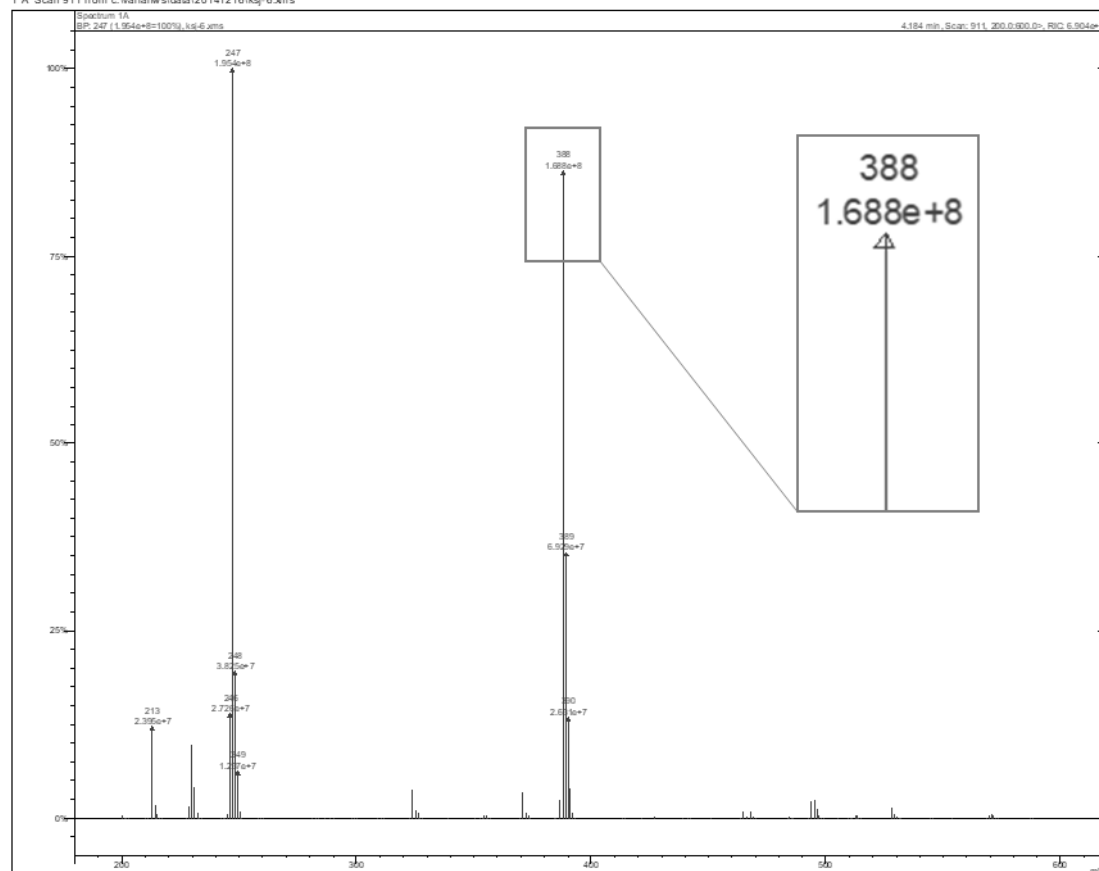
1.5.2 N,N'-(4,5-dinitro-1,2-phenylene) dibenzenesulfonamide.

1,2-Bis-(phenylenesulfonamido)benzene (20 g, 51 mmol) dissolved in acetic acid (160 ml). Drop nitric acid (7 ml) into previous solution and react for 30 min under 60°C. Then, pour into water and recrystallize with acetic acid. (89% yield) ^{1}H NMR (400 MHz, DMSO-d$_6$) δ 7.55 (m,2H), 7.65 (m,1H),7.69 (s,1H), 7.69 (m,2H), 7.77 (m,2H); ^{13}C NMR δ 115.79, 126.80, 129.56, 133.63, 134.07, 136.93, 138.96. MS (MALDI-TOF): m/z (%) = 478 (45) [M]$^+$, 337 (100) Anal. Calc. For C$_{18}$H$_{14}$N$_4$O$_8$S$_2$: C, 45.19; H, 2.95; N, 11.71; S, 13.40; O, 26.75; Found: C, 45.35; H, 2.93; N, 11.82; S, 14.28 (**Figure 1.8**).
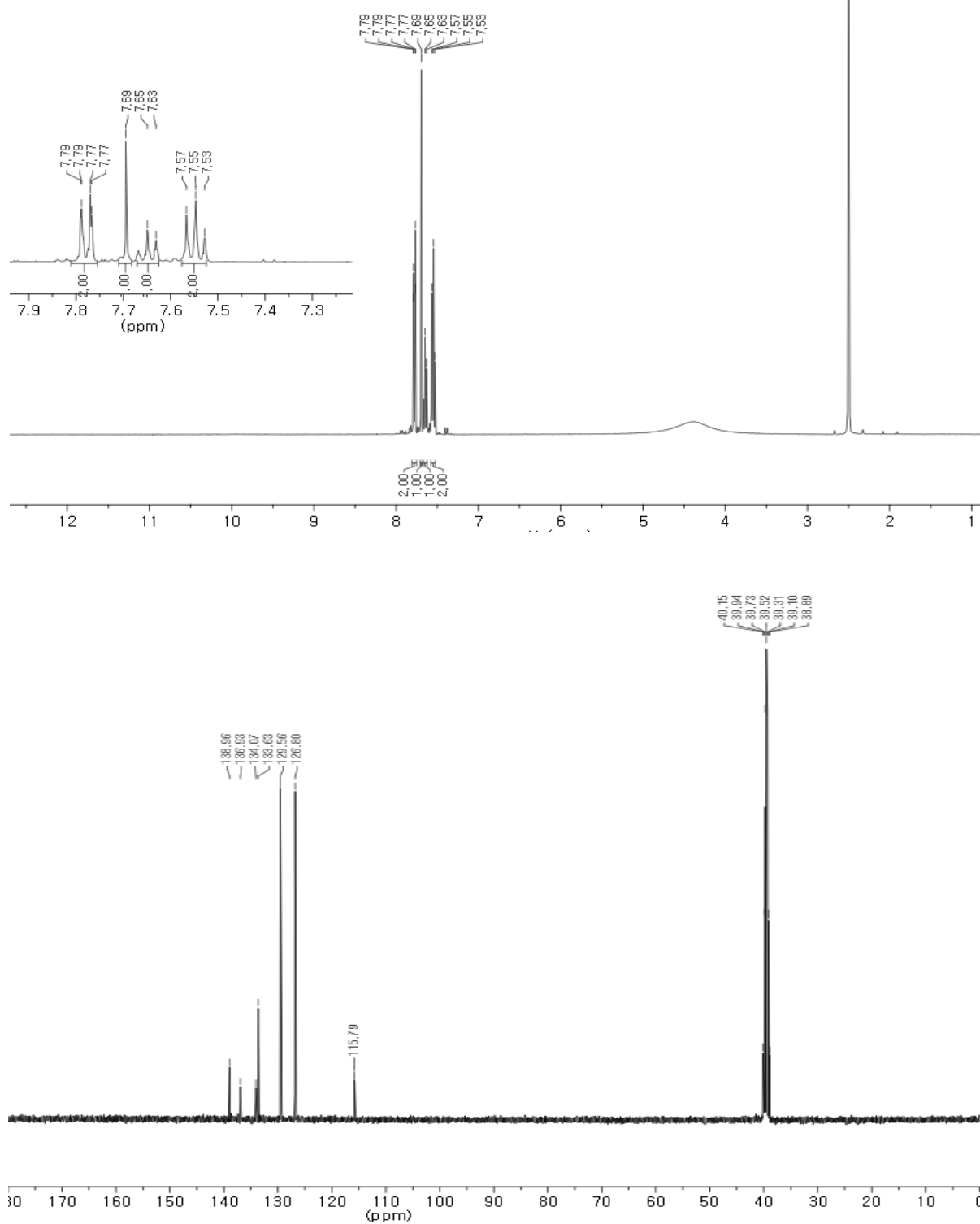
Figure 1.8. ^{1}H NMR (top), ^{13}C NMR (bottom) and MALDI-TOF MS spectrum of N,N'-(4,5-dinitro-1,2-phenylene) dibenzenesulfonamide (MALDI-TOF MS is on the next page).
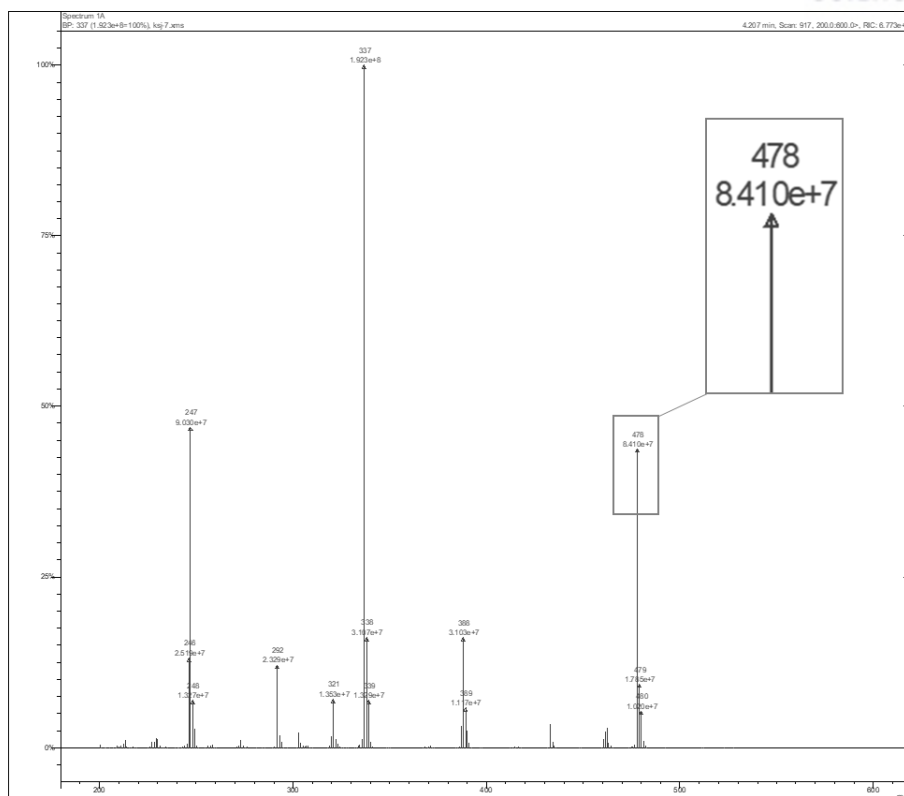
1.6 References

(1)   Mastalerz, M.; Sieste, S.; Cenic, M.; Oppel, I. M. *J. Org. Chem.* **2011**, *76*, 6389.

(2)   Ding, S. Y.; Wang, W. *Chem. Soc. Rev.* **2013**, *42*, 548.

(3)   Xu, H.; Jiang, D. *Nat. Chem.* **2014**, *6*, 564.

(4)   Cote, A. P.; Benin, A. I.; Ockwig, N. W.; O'Keeffe, M.; Matzger, A. J.; Yaghi, O. M. *Science* **2005**, *310*, 1166.

(5)   El-Kaderi, H. M.; Hunt, J. R.; Mendoza-Cortes, J. L.; Cote, A. P.; Taylor, R. E.; O'Keeffe, M.; Yaghi, O. M. *Science* **2007**, *316*, 268.

(6)   Wu, D. C.; Xu, F.; Sun, B.; Fu, R. W.; He, H. K.; Matyjaszewski, K. *Chem. Rev.* **2012**, *112*, 3959.

(7)   Furukawa, H.; Yaghi, O. M. *J. Am. Chem. Soc.* **2009**, *131*, 8875.

(8)   Dogru, M.; Handloser, M.; Auras, F.; Kunz, T.; Medina, D.; Hartschuh, A.; Knochel, P.; Bein, T. *Angew. Chem. Int. Ed.* **2013**, *52*, 2920.

(9)   Spitler, E. L.; Colson, J. W.; Uribe-Romo, F. J.; Woll, A. R.; Giovino, M. R.; Saldivar, A.; Dichtel, W. R. *Angew. Chem. Int. Ed.* **2012**, *51*, 2623.

(10)   Ding, S. Y.; Gao, J.; Wang, Q.; Zhang, Y.; Song, W. G.; Su, C. Y.; Wang, W. *J. Am. Chem. Soc.* **2011**, *133*, 19816.

(11)   Mahmood, J.; Lee, E. K.; Jung, M.; Shin, D.; Choi, H.-J.; Seo, J.-M.; Jung, S.-M.; Kim, D.; Li, F.; Lah, M. S.; Park, N.; Shin, H.-J.; Oh, J. H.; Baek, J.-B. *Proc. Natl. Acad. Sci. U.S.A.* **2016**, *113*, 7414.

(12)   Mahmood, J.; Lee, E. K.; Jung, M.; Shin, D.; Jeon, I.-Y.; Jung, S.-M.; Choi, H.-J.; Seo, J.-M.; Bae, S.-Y.; Sohn, S.-D.; Park, N.; Oh, J. H.; Shin, H.-J.; Baek, J.-B. *Nat. Commun.* **2015**, *6*.

(13)   Colson, J. W.; Woll, A. R.; Mukherjee, A.; Levendorf, M. P.; Spitler, E. L.; Shields, V. B.; Spencer, M. G.; Park, J.; Dichtel, W. R. *Science* **2011**, *332*, 228.

(14)   Lemaur, V.; Da Silva Filho, D. A.; Coropceanu, V.; Lehmann, M.; Geerts, Y.; Piris, J.; Debije, M. G.; Van de Craats, A. M.; Senthilkumar, K.; Siebbeles, L. D. A.; Warman, J. M.; Bredas, J. L.; Cornil, J. *J. Am. Chem. Soc.* **2004**, *126*, 3271.

(15)   Gao, B. X.; Wang, M.; Cheng, Y. X.; Wang, L. X.; Jing, X. B.; Wang, F. S. *J. Am. Chem. Soc.* **2008**, *130*, 8297.

(16)   Velazquez, D. G.; Orive, A. G.; Creus, A. H.; Luque, R.; Ravelo, A. G. *Org. Biomol. Chem.* **2011**, *9*, 6524.

(17)   Shao, J. J.; Chang, J. J.; Chi, C. Y. *Org. Biomol. Chem.* **2012**, *10*, 7045.

(18)   Bunz, U. H. F. *Chem. Eur. J.* **2009**, *15*, 6780.

(19)   Preston, P. N. *Chem. Rev.* **1974**, *74*, 279.

(20)   Pereira, C. M. P.; Stefani, H. A.; Guzen, K. P.; Orfao, A. T. G. *Lett. Org. Chem.* **2007**, *4*, 43.

(21)   Vagin, S. I.; Ott, A. K.; Hoffmann, S. D.; Lanzinger, D.; Rieger, B. *Chem. Eur. J.* **2009**, *15*, 5845.

(22)   Shang, X. F.; Li, X. J.; Xi, N. K.; Zhai, Y. T.; Zhang, J. L.; Xu, X. F. *Sensor. Actuat. B-Chem.* **2011**, *160*, 1112.

(23)   Shang, X. F.; Lin, H.; Lin, H. K. *J. Fluorine. Chem.* **2007**, *128*, 530.

(24)   Kleineweischede, A.; Mattay, J. *Eur. J. Org. Chem.* **2006**, 947.

(25)   Tehfe, M. A.; Lalevee, J.; Telitel, S.; Contal, E.; Dumur, F.; Gigmes, D.; Bertin, D.; Nechab, M.; Graff, B.; Morlet-Savary, F.; Fouassier, J. P. *Macromolecules* **2012**, *45*, 4454.

(26)   Arnold, F. E. *J. Polym. Sci., Part A: Polym. Chem.* **1970**, *8*, 2079.

(27)   Kestemont, G.; de Halleux, V.; Lehmann, M.; Ivanov, D. A.; Watson, M.; Geerts, Y. H. *Chem. Commun.* **2001**, 2074.

(28)   Hanyu, Y.; Sugimoto, T.; Ganbe, Y.; Masuda, A.; Honma, I. *J. Electrochem. Soc.* **2014**, *161*, A6.

(29)   Xu, Y.; Jin, S.; Xu, H.; Nagai, A.; Jiang, D. *Chem. Soc. Rev.* **2013**, *42*, 8012.

(30)   Guo, J.; Xu, Y.; Jin, S.; Chen, L.; Kaji, T.; Honsho, Y.; Addicoat, M. A.; Kim, J.; Saeki, A.; Ihee, H.; Seki, S.; Irle, S.; Hiramoto, M.; Gao, J.; Jiang, D. *Nat. Commun.* **2013**, *4*.

(31)   Mavrodi, D. V.; Blankenfeldt, W.; Thomashow, L. S. *Annu. Rev. Phytopathol.* **2006**, *44*, 417.

(32)   Kou, Y.; Xu, Y.; Guo, Z.; Jiang, D. *Angew. Chem. Int. Ed.* **2011**, *50*, 8753.

(33)   Liang, H.; He, Y.; Ye, Y.; Xu, X.; Cheng, F.; Sun, W.; Shao, X.; Wang, Y.; Li, J.; Wu, K. *Coord. Chem. Rev.* **2009**, *253*, 2959.

II. Two-Dimensional Polymer Encapsulated Zero-Valent Iron Nanoparticles as a Durable Oxygen Reduction Electrocatalyst

2.1 Abstract

Fe/Fe$_3$C and Fe-N-C based catalysts have gained considerable attentions as oxygen reduction reaction (ORR) catalysts owing to their high activity. However, their applications are mainly hindered by the poor stability, which originates from the non-uniform nanostructure, and low quality of crystallinity. Here, we introduce a synthetic strategy for a uniform, compact encapsulation through fully-aromatic two-dimensional (2D) porous organic networks (PONs). The catalyst was synthesized by *in-situ* encapsulating zero-valent iron (Fe^0) in 2D phenazine-based structure (denoted as Fe@Aza-PON). Compared to without PON (Fe@TAB) which was encapsulated by single monomer, Fe@Aza-PON showed superior catalytic performance (half-wave potential, 13 mV and Tafel slope, 60 mV dec^{-1}). Thanks to the structural advantages of PON, the catalytic activity is maintained even after 100,000 cycles with tolerance against contaminations (methanol and CO poisoning). In addition, Fe@Aza-PON demonstrates competitiveness in the hybrid Li-air cell as an outstanding alternative synthetic strategy for practical applications.

2.2 Introduction

To address pressing energy and environmental issues, fuel cells and metal-air cells, which are considered sources of future clean energy, have been intensively explored as alternatives to fossil fuels.[1,2] However, their development has been hampered by the sluggish cathodic oxygen reduction reaction (ORR), which is approximately six orders of magnitude slower than the corresponding anodic hydrogen oxidation reaction (HOR).

Among efforts to develop alternative ORR catalysts to replace precious platinum (Pt)-based ones, non-precious metal-doped carbon-based materials have been reported to contribute to significantly enhanced ORR activity. In addition, Fe/Fe$_3$C and Fe-N-C materials are regarded as promising ORR catalysts in alkaline media.[3-6] Based on these results, there have been a number of studies attempting to encapsulate Fe nanoparticles (Fe/Fe$_3$C) in carbon-based materials, such as carbon nanotubes (CNTs), graphene, and other carbonaceous materials.[7,8]

However, pure carbon-based materials are basically neutral and fail to provide abundant interaction sites for the protective encapsulation of unstable Fe nanoparticles.[8,9] To provide better interaction, a mixture of Fe precursor and nitrogen containing small molecules, such as melamine and porphyrin, have been pyrolyzed at high temperature to form Fe/Fe$_3$C and Fe-N-C catalysts.[6,10] Although they have demonstrated high electrocatalytic activity, comparable to Pt-based catalysts,[5,11-13] they still suffer from poor long-term stability for practical application, due most likely to defective encapsulation.

Heteroatom-containing two-dimensional (2D) porous organic networks (PONs) have also been explored as materials for energy conversion and storage.[14,15] In addition to having controllable pore dimensions and thereby tunable intrinsic properties,[15] their extended π-conjugated structure helps electron transport, for better conductivity and stronger dipole interaction for efficient electron/ion diffusion.[16]

Fused all aromatic PONs are regarded as promising materials for applications such as light harvesting,[17,18] heterogeneous catalysis,[19,20] and gas adsorption.[21-23] The 2D phenazine-based PONs (denoted as Aza-PONs) have also shown good performance in supercapacitors[24] and have been studied as catalysts for the production of hydrogen peroxide.[25] In addition, the pyridinic nitrogen (N) in the structure of Aza-PON can facilitate better oxygen diffusion onto the catalytically active sites.[26] For these reasons, in this study, Aza-PON was selected to encapsulate zero-valent Fe (Fe^0) nanoparticles for the synthesis of a stable Fe-based ORR electrocatalyst.

2.3 Results and discussion
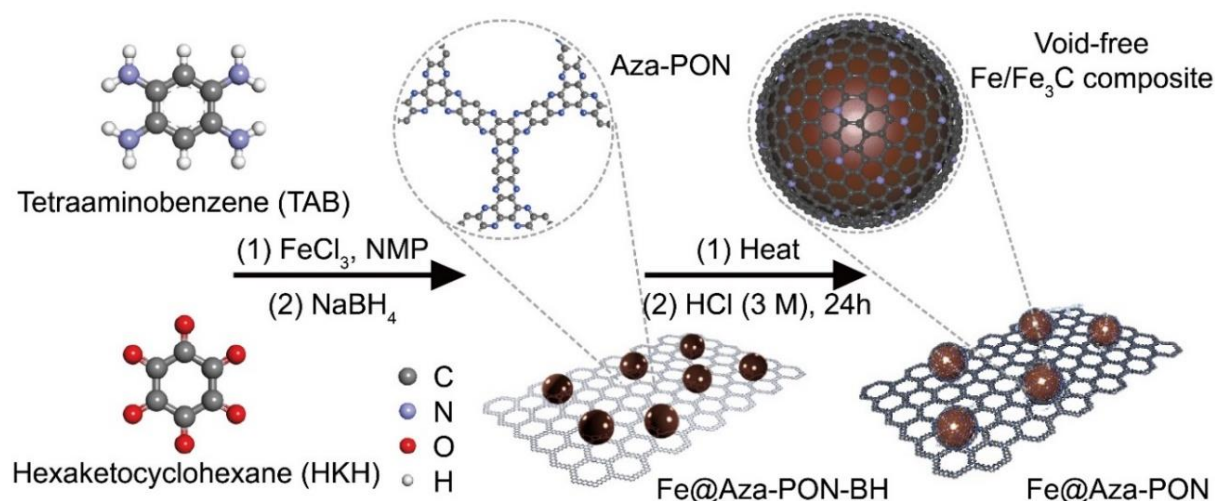
Figure 2.1. Schematic representation for the synthesis for the formation of Fe@Aza-PON.

Figure 2.1 shows the synthesis procedures for the Fe@Aza-PON. The reaction between 1,2,4,5-tetraaminobenzene (TAB) and hexaketocyclohexane (HKH) in the presence of iron(III) chloride ($FeCl_3$) forms Fe^{3+} sandwiched between Aza-PON sheets (Fe^{3+}@Aza-PON). The built-in nitrogenated holey phenazine units (fused aromatic $C_4=C_4N_2=C_4$ rings) in the Aza-PON structure can provide abundant coordination sites to stably sandwich Fe^{3+}. According to theoretical calculations,[27] the aromatic nitrogen in phenazine can coordinate with Fe^{2+}/Fe^{3+} and allows stability during the rest of the treatments (reduction of Fe^{3+} into Fe^0 with sodium borohydride ($NaBH_4$) and washing off free $FeCl_3$ with distilled water). The sandwiched Fe^{2+}/Fe^{3+} species can be completely reduced into zero-valent Fe (Fe^0) nanoparticles encased in nitrogenated graphitic layers after heat-treatment at 750 °C.

15
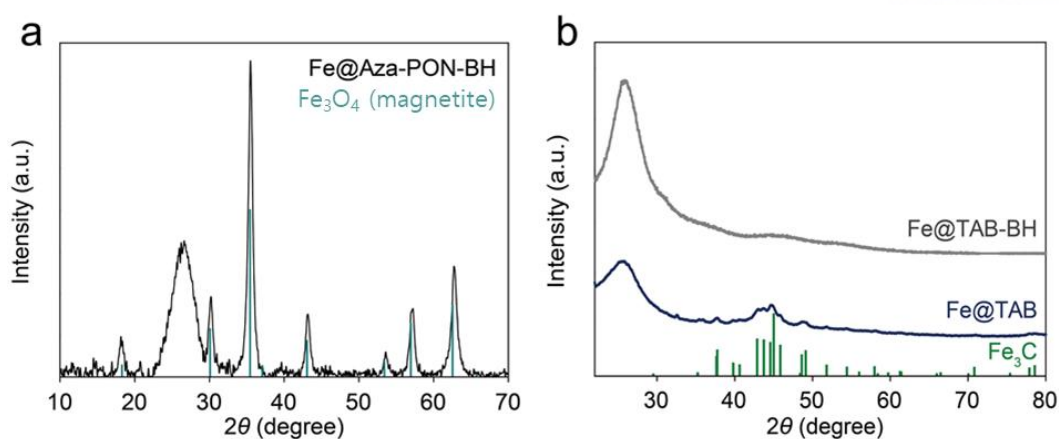
Figure 2.2. High-power X-ray diffraction patterns. (a) Fe@Aza-PON-BH (before heat treatment). (b) Fe@TAB-BH, Fe@TAB. The magnetite (dark cyan bar) and iron carbide (dark green bar) peaks are shown in (a), (b), respectively.
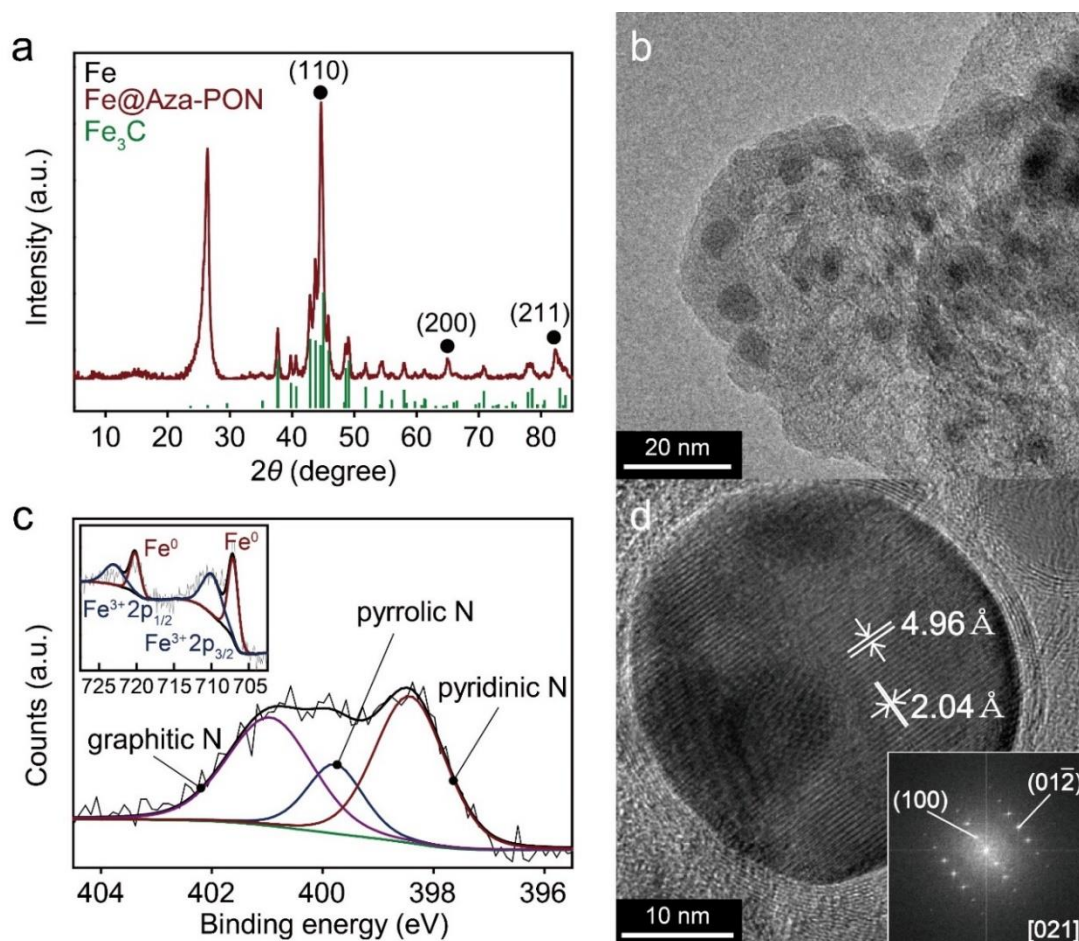
Figure 2.3. Structural analysis. (a) XRD pattern of Fe@Aza-PON; iron carbide (Fe_3C, blue bar) and iron (Fe, red dot) peaks. (b) Transmission electron microscope (TEM) image of Fe@Aza-PON-BH (before heat-treatment). (c) X-ray photoelectron spectroscopy (XPS) of Fe@Aza-PON: N 1s, inset: Fe 2p; (d) TEM image of Fe@Aza-PON after heat-treatment at 750 °C. Inset: the fast Fourier transform (FFT) corresponding iron carbide.

16

Before heat-treatment of the samples, the X-ray diffraction (XRD) pattern shows strong magnetite (Fe_3O_4) peaks, corresponding to Fe^{2+}/Fe^{3+}@Aza-PON (Fe@Aza-PON-BH; BH stands for before heat-treatment, **Figure 2.2a**). After heat-treatment, Aza-PON, in contact with Fe^{2+}/Fe^{3+} moieties, was converted into nitrogenated graphitic shells on the surface of reduced zero-valent Fe (Fe^0) nanoparticles. Encapsulated Fe nanoparticles distributed on the Aza-PON (Fe@Aza-PON) is then produced (**Figure 2.1**). Finally, defectively encapsulated Fe nanoparticles were leached off with 3.0 M aq. hydrochloric acid (HCl) for 24h to produce a durable Fe@Aza-PON catalyst.

The XRD pattern of the Fe@Aza-PON catalyst (**Figure 2.3a**) shows pure Fe^0 and iron carbide (Fe_3C) peaks along with a (002) peak (*d*-spacing of 0.337 nm), which corresponds to a typical van der Waals distance of graphitic layers. The Fe peaks at 44.7°, 65.0° and 82.3° correspond to Fe (110), Fe (200) and Fe (211), respectively.
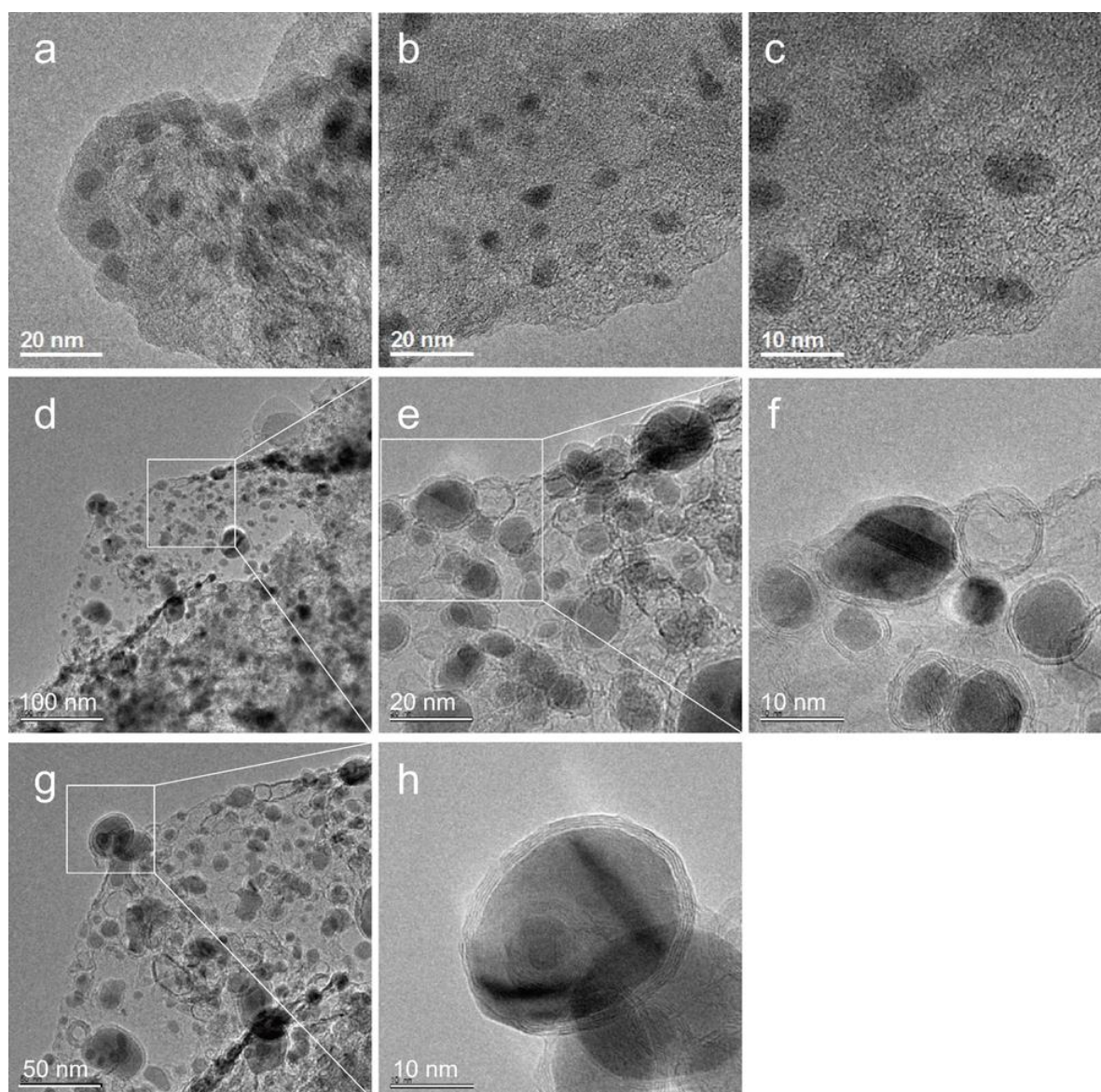
Figure 2.4. TEM images of Fe@Aza-PON. (a-c) Before heat-treatment. (d-h) After heat-treatment.
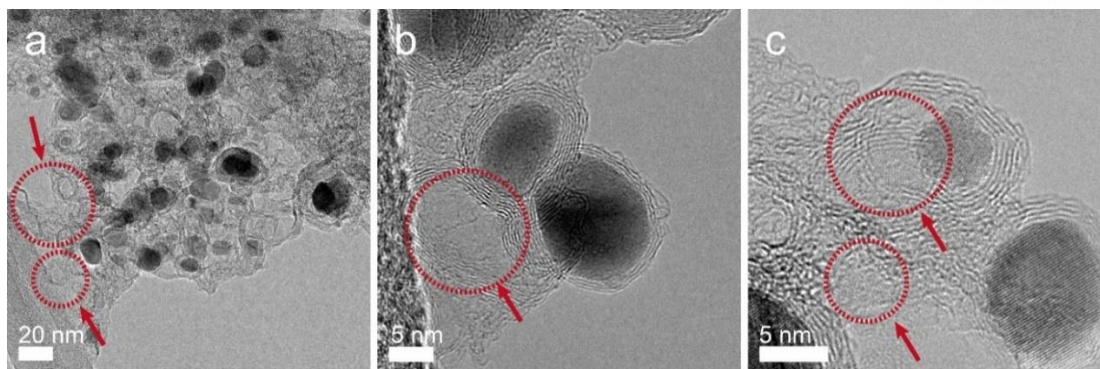
Figure 2.5. HR-TEM images of heat-treated Fe@Aza-PON. (a-c) Dark red arrows indicate the structure of holes after leaching off of the Fe nanoparticles.

The transmission electron microscopy (TEM) image of the Fe@Aza-PON-BH (before heat-treatment) shows well distributed nanoparticles in the range of 5-10 nm on 2D Aza-PON (**Figure 2.3b** and **Figure 2.4a-c**). After the heat-treatment and acid leaching procedures, the Fe@Aza-PON shows Fe^0 nanoparticles encapsulated in approximately 3-7 graphitic shells which corresponds to layers thickness of 1.01-2.36 nm. (**Figure 2.3d, Figure 2.4d-h**). This result suggests that the Aza-PON matrix was converted into graphitic layers on the surface of the Fe^0 nanoparticles.

In some cases, empty shells were observed (dark red arrows, **Figure 2.5**), because defectively encapsulated Fe nanoparticles were leached by the strong acid treatment. Accordingly, Fe nanoparticles that remained intact within the Fe@Aza-PON were expected to be stably encased in graphitic.

Energy-dispersive X-ray spectroscopy (EDX) indicated that the catalyst consisted of C, N and Fe elements (**Figure 2.6**). The loading amount of Fe in the Fe@Aza-PON catalyst was approximately 20 wt% as determined by thermogravimetric analysis (TGA) in air atmosphere (**Figure 2.7**).
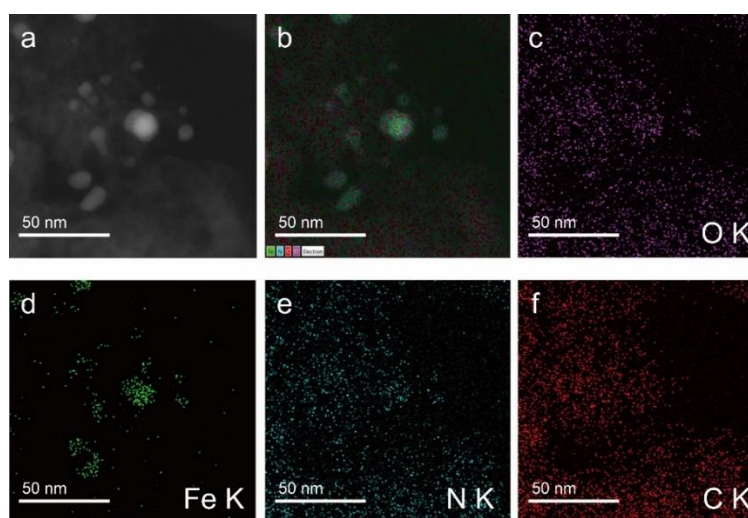
Figure 2.6. The energy dispersive spectroscopy (EDS) elemental mapping images of Fe@Aza-PON. (a) High-angle annular dark-field (HAADF) image. (b) Total element mapping image. (c) Oxygen. (d) Iron. (e) Nitrogen. (f) Carbon.

The chemical bonding nature of the Fe@Aza-PON was investigated by X-ray photoelectron spectroscopy (XPS). As expected, the survey spectrum showed only C, N, O and Fe peaks without other peaks (**Figure 2.3c, Figure 2.8**). Deconvoluted N 1s peaks corresponding to graphitic N (401.0 eV), pyrrolic N (400.0 eV) and pyridinic N (398.4 eV), indicated the presence of nitrogenated graphitic shells from the pyrolysis of the Aza-PON moiety during heat-treatment. The Fe (Fe 2p) survey spectrum showed Fe^0 (720.2, 707.1 eV), Fe^{3+} $2p_{1/2}$ (723.0 eV), and $2p_{3/2}$ (709.9 eV), suggesting the co-existence of pure Fe^0 core particles and Fe_3C interfaces.
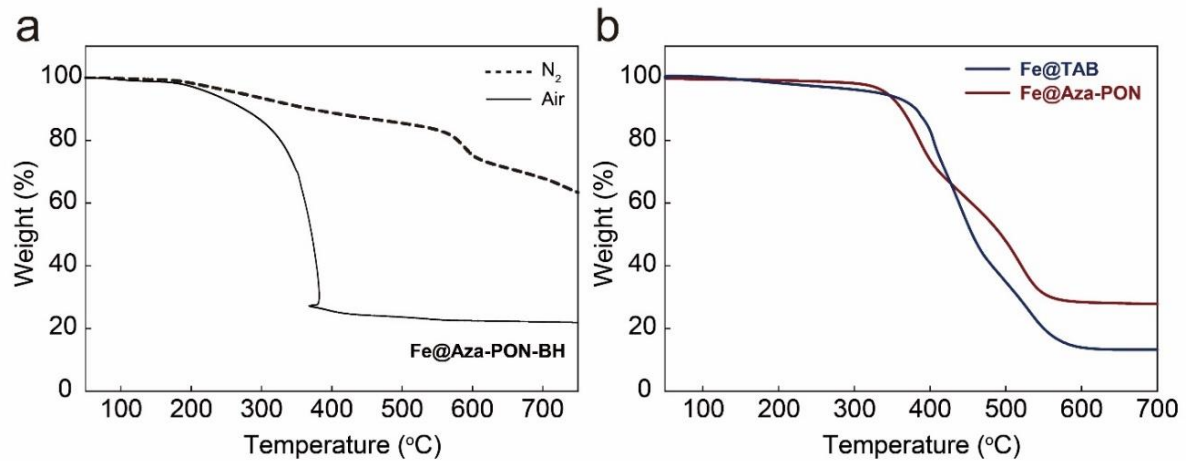
Figure 2.7. TGA thermograms were measured at a ramping rate of 10 °C min^{-1}. (a) Fe@Aza-PON-BH: in air (solid line), in nitrogen (dot line). (b) in air, Fe@Aza-PON (dark red): The residual char yield of 27.70 wt% at 600 °C, which was associated with iron oxide (Fe_2O_3) and the corresponding amount of Fe is 19.39 wt%; Fe@TAB (dark blue): The residual char yield of 13.72 wt% and pure Fe is 9.06 wt%.

Figure 2.8. XPS spectra of Fe@Aza-PON. (a) Survey spectrum, inset is deconvoluted O 1s spectra. (b) C 1s spectra.

19
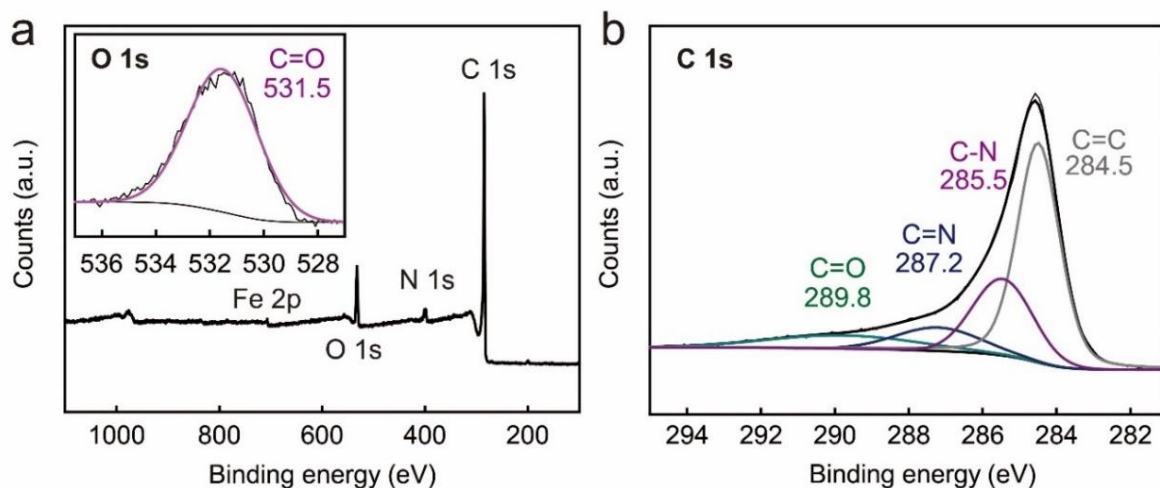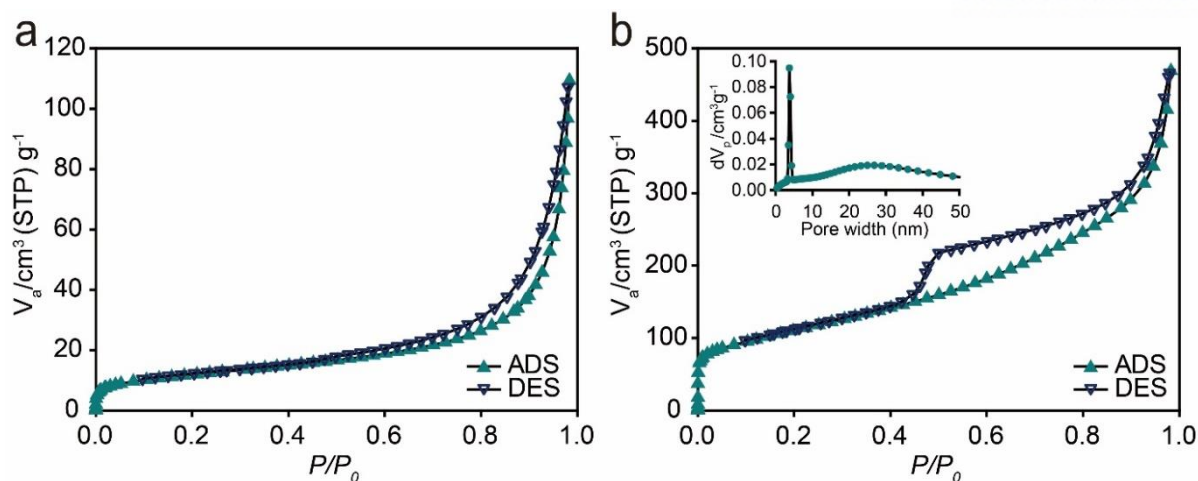
Figure 2.9. N_2 adsorption-desorption isotherms at 77 K. (a) Fe@Aza-PON-BH before heat-treatment. (b) Fe@Aza-PON after heat-treatment. Inset: pore size distribution was calculated by NLDFT.

The Fe@Aza-PON sample exhibited a high Brunauer-Emmett-Teller (BET) specific surface area of 393.98 m^2 g^{-1} (**Figure 2.9**). The type IV hysteresis adsorption plot in the mesoporous region indicated bottle-like empty graphitic shells after leaching of the defectively encapsulated Fe nanoparticles (arrows, **Figure 2.5**). In addition, scanning electron microscopy (SEM) images (**Figure 2.10**) also reflect the presence of empty shells of the Fe@Aza-PON catalyst.

For comparison with Aza-PON (macromolecular network), Fe on carbonized TAB (Fe@TAB) was synthesized by simply mixing $FeCl_3$ and TAB (a monomeric building block) without the presence of HKH (a counterpart monomeric building block). Mixing the Fe precursor and a small amount of organic substance, and then subsequently carbonizing the mixture, is a typical approach for the formation of the Fe-N-C catalyst (experimental details described in Supplementary Information, **Figure 2.11**).[6,10,12,28,29] In this approach, TAB acts as a small molar mass feedstock for the C and N elements during graphitization.
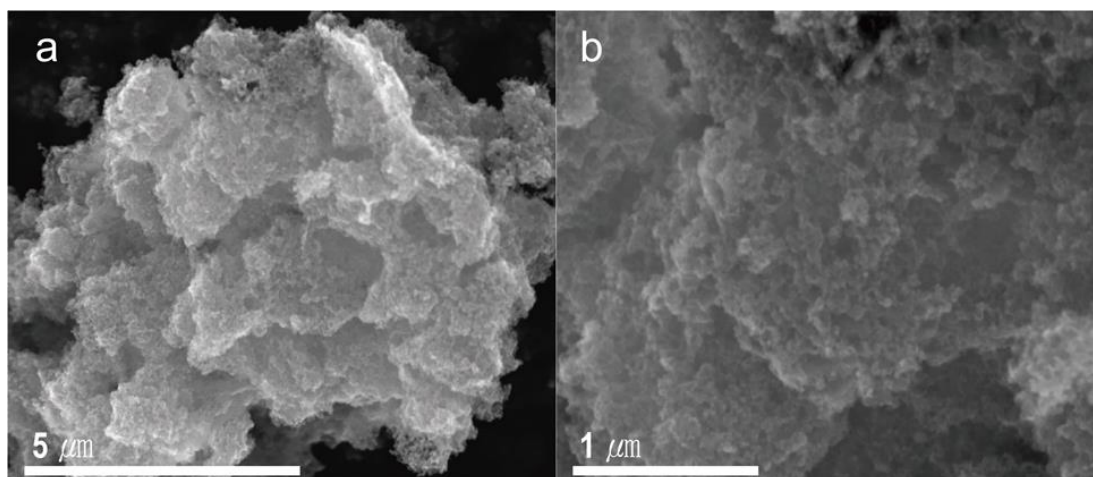
Figure 2.10. (a, b) SEM images of Fe@Aza-PON at different magnification.

For comparison with Aza-PON, Fe@TAB was synthesized by mixing FeCl$_3$ and TAB without presence of HKH (Supporting information). The carbonization is a typical approach for the formation of Fe-N-C catalyst.[6, 9-10, 12, 29] In this approach, TAB plays as a small molar mass feedstock for C and N elements during graphitization. After acid leaching, the Fe@TAB exhibits a similar XRD pattern with Fe@Aza-PON, but its iron peak intensity is relatively much lower (**Figure 2.2b**). The TEM images are well agreed with XRD result, showing much more empty shells after acid leaching (arrows, **Figure. 2.12**).
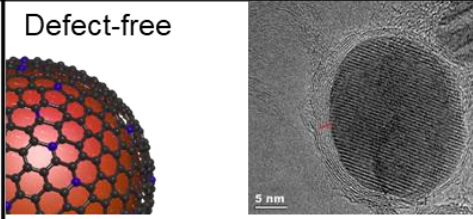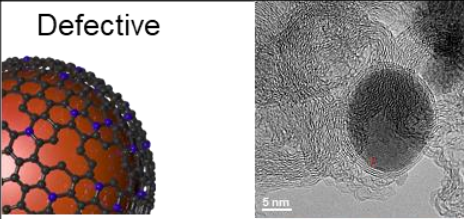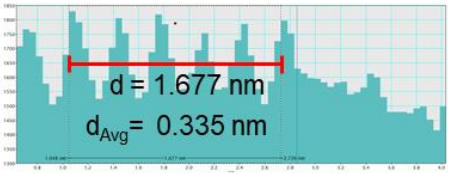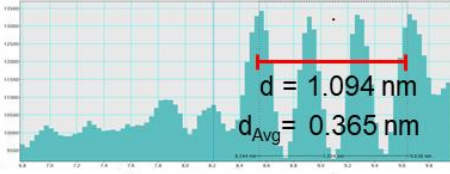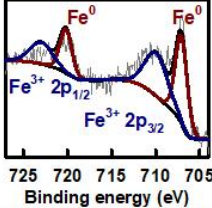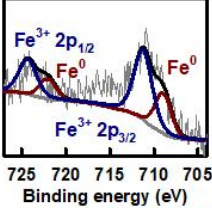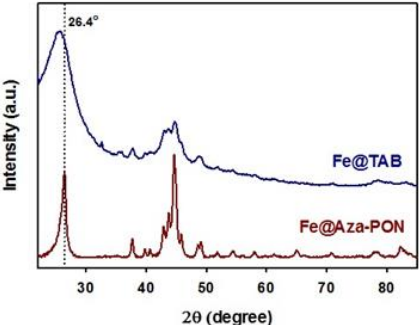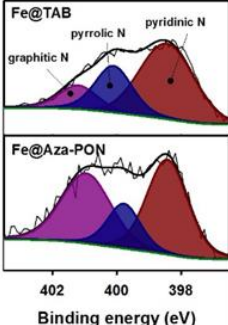
Figure 2.11. Schematic representation of the synthesis of Fe@TAB.

Now, how Aza-PON is converted into void-free nitrogenated graphitic sheets on the surface of Fe nanoparticles? The Fe$_3$O$_4$-catalyzed conversion of carbon feedstock into graphitic structure for encapsulation is well-known mechanism,[30-32] in which Fe$_3$O$_4$ is prone to reduce into the forms of FeO, Fe and Fe$_3$C. During the heat-treatment, the Fe$_3$O$_4$ nanoparticles in contact with Aza-PON frameworks are reduced to form Fe$_3$C at the boundary, while their core part is reduced to Fe^0 only. Hence, as schematically represented in **Figure 2.1**, the structure of Fe@Aza-PON can be described as follow; encapsulated Fe nanoparticles in near the surface of nitrogenated graphitic shells protected further reduction of Fe^0 then, forming the Fe/Fe$_3$C composite simultaneously. In case of Fe@TAB, TAB is not able to form crystalline void-free graphitic shells then, reduction from Fe^0 to Fe$_3$C can be easily proceeded. As a result, the ratio of Fe/Fe$_3$C in Fe@TAB is lower than that in Fe@Aza-PON.

After acid leaching, the Fe@TAB exhibited an XRD pattern similar to that of Fe@Aza-PON. However, its iron peak intensity was relatively much lower (**Figure 2.2b**). The XRD result agreed well with TEM images, which showed many more empty shells after acid leaching (arrows, **Figure 2.12**). The result implies that the 2D layered PON can accommodate much more Fe precursor, resulting in a lower rate of defective encapsulation of Fe nanoparticles (**Table 2.1**). For the Fe@TAB case, because the TAB forms defective graphitic shells, further heat treatment converts the Fe^0 into Fe$_3$C. As a result, the ratio of Fe/Fe$_3$C in Fe@TAB is lower than that in Fe@Aza-PON (**Table 2.1**). The defective free encapsulation is related to the flexible nature and strong affinity of the Aza-PON for the Fe metal due to presence of nitrogen atoms around the holes as an anchoring points.[27,30]

Table 2.1. Comparison of structural differences, Fe (wt%) content in the catalyst, catalytic performance and stability between Fe@Aza-PON and Fe@TAB

	Fe@Aza-PON		Fe@TAB	
Structure	Defect-free d = 1.677 nm d_{Avg} = 0.335 nm		Defective d = 1.094 nm d_{Avg} = 0.365 nm	
Reagent	TAB + HKH (Aza-PON) + $FeCl_3$ (1.1 g + 0.8 g + 1.0 g)		TAB + $FeCl_3$ (1.1 g + 1.0 g)	
Fe (wt%)	19.39%		9.06%	
Catalytic performance (half-wave potential, Tafel slope)	0.1 M KOH	0.1 M $HClO_4$	0.1 M KOH	0.1 M $HClO_4$
	0.839 V (RHE) 60 mV dec^{-1}	0.541 V (RHE) 116 mV dec^{-1}	0.657 V (RHE) 112 mV dec^{-1}	0.371 V (RHE) 250 mV dec^{-1}
Stability (after 10 000 cycles)	Alkaline condition: ~100% Acidic condition : ~100% (Maintained original activity even after 100 000 cycles)		Alkaline condition: 86.88% Acidic condition: 71.85%	
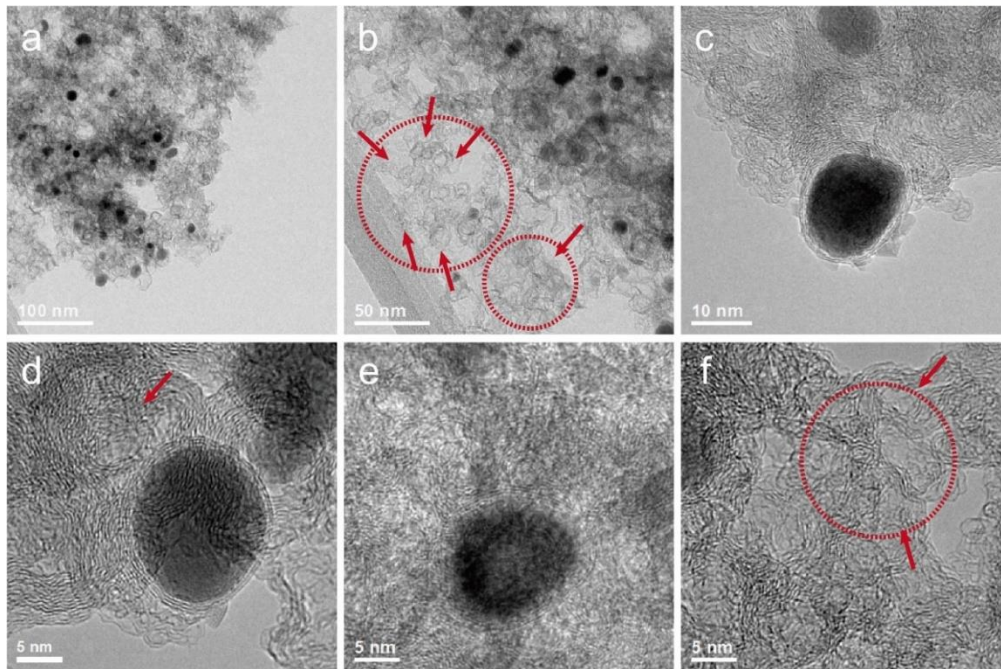
At % table (within Structure):

At %	Fe@Aza-PON	Fe@TAB
C	85.95	79.16
N	4.67	9.49
O	8.90	10.20
Fe	0.48	1.15

Figure 2.12. HR-TEM images of Fe@TAB. (a-f) Most of Fe particles are leached off by acid treatment (dark red arrows).
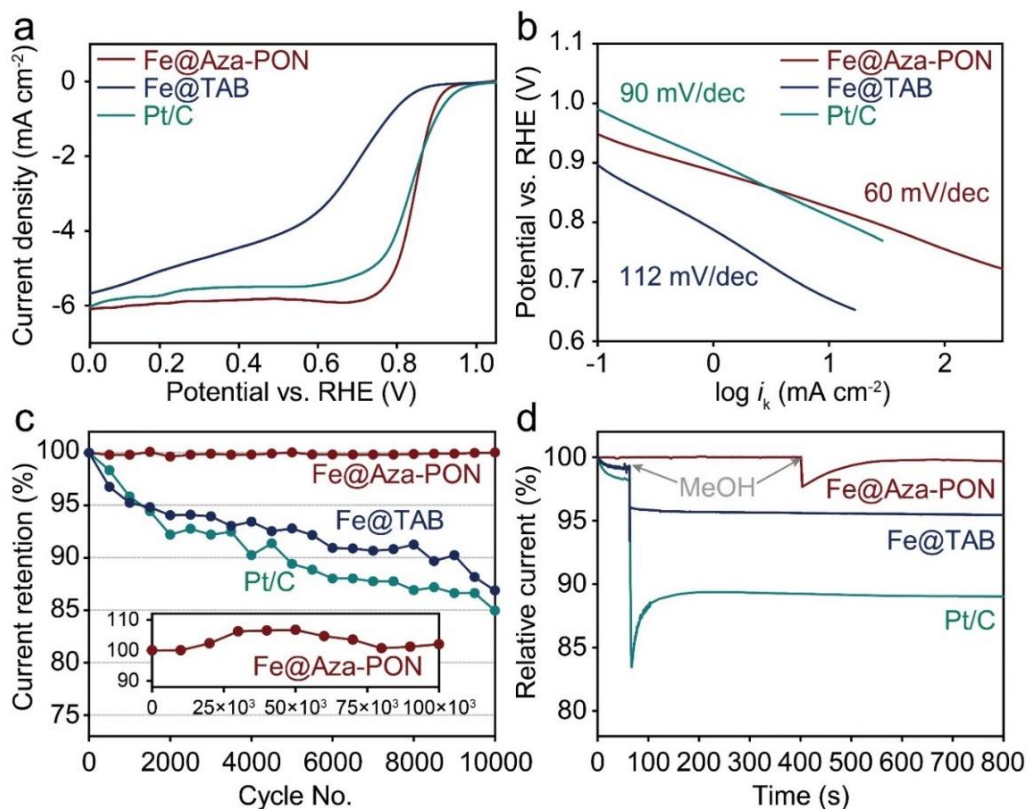
Figure 2.13. Electrochemical ORR performance in 0.1 M aq. KOH. (a) Rotating ring-disk electrode (RRDE) polarized curves recorded with Fe@Aza-PON, Pt/C and Fe@TAB (red: Fe@Aza-PON, black: Fe@TAB , blue: Pt/C) (b) Tafel plot, (c) the test for catalytic stability and (d) result for methanol poisoning.

Next, the mechanism for converting Aza-PON into nitrogenated graphitic shells on the surface of Fe nanoparticles was investigated. The Fe_3O_4-catalyzed conversion of carbon feedstock into graphitic structures for void-free encapsulation is a well-known mechanism,[31-33] in which the Fe_3O_4 is prone to reduce into the forms of FeO, Fe and Fe_3C. During heat-treatment, the Fe_3O_4 nanoparticles in contact with the Aza-PON frameworks are reduced to form Fe_3C at the boundary, while their core part is reduced to Fe^0.

Figure 2.14. Study of elemental composition changes and dependence of electrocatalytic performance on annealing temperature. (a) Element contents of Fe@Aza-PON with respect to annealing temperatures. Inset is a numerical percentage of each element. (b) XPS spectra of Fe@Aza-PON with respect to annealing temperatures. Inset: numerical percentage of each element. (c) CV curves of samples annealed at different temperatures in 0.1 M aq. KOH Condition (catalyst loading: 20 μg, scan rate: 10 mV s^{-1}). (d) Average onset potential *vs.* annealing temperature plots after three measurements (dark red dot).

Hence, as schematically represented in **Figure 2.1**, the structure of the Fe@Aza-PON can be described as follows. The Fe@Aza-PON is composed of Fe nanoparticle cores encapsulated in nitrogenated graphitic shells, which can protect against further reduction of Fe^0 into Fe_3C at the interface and are distributed on the Aza-PON matrix (**Figure 2.1**).

To optimize catalytic performance, control experiments were carried out. As the temperature increased, carbon content increased while nitrogen content decreased (**Figure 2.14a, b**). At higher temperature, the content of pyridinic nitrogen from pyrazine rings in the Aza-PON decreased, as indicated by the reduction in supercapacitance (**Figure 2.14c**).[24] This result is related to the rate of oxygen diffusion as the ratio of Aza-PON was reduced.

However, electron conductivity was improved due to the removal of edge groups,[34,35] which allows better conductive contact. From this complementary relationship between oxygen diffusion and electron conductivity, the optimum annealing temperature was selected to be 750 °C (**Figure 2.14d**). Thus, the catalyst heat-treated at 750 °C was further studied to investigate detailed ORR catalysis.
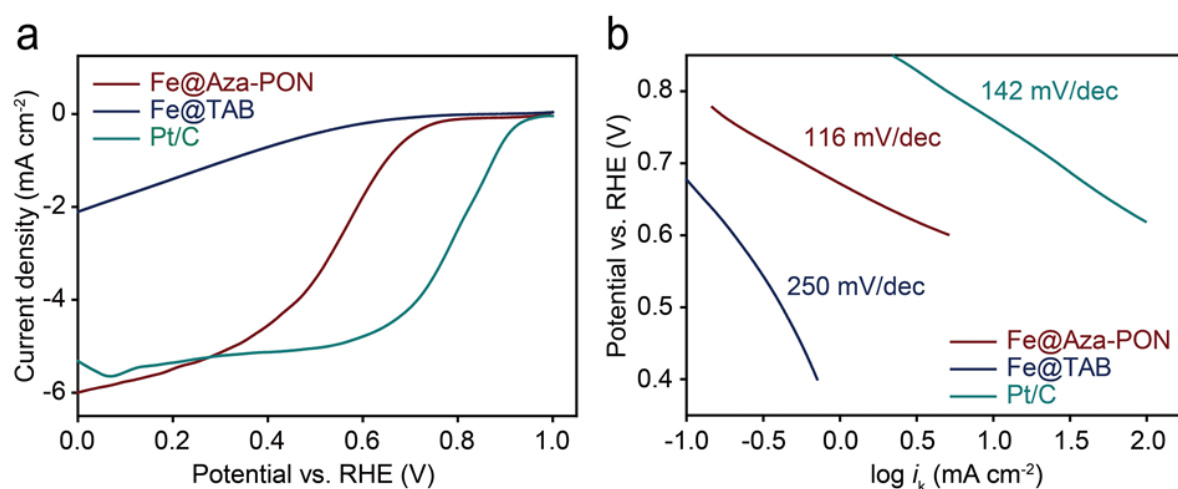
Figure 2.15. Rotating ring-disk electrode (RRDE) voltammograms recorded with Fe@Aza-PON, Pt/C and Fe@TAB in 0.1 M aq. $HClO_4$ solution. (a) LSV curves. (b) Tafel plots (each 30 μg of catalyst amount is loaded, scan rate: 10 mV s^{-1} at 1600 rpm).
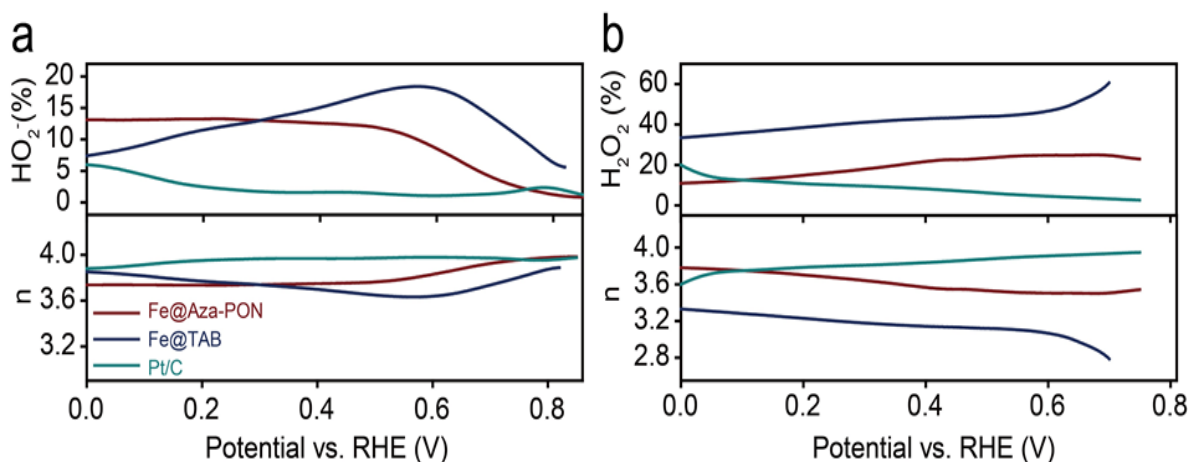
Figure 2.16. The electron transfer number with HO_2^- (or H_2O_2) concentration for Fe@Aza-PON, Fe@TAB, and Pt/C. (a) 0.1 M aq. KOH. (b) 0.1 M aq. $HClO_4$ (scan rate: 10 mV s^{-1}).

Given its structural configuration, Fe@Aza-PON was evaluated as a stable indirect-contact ORR catalyst (with non-contact between the surface of the Fe nanoparticle and oxygen). To begin with, rotating ring disk electrode (RRDE) measurements were conducted with a scan rate of 10 mV s^{-1} at 1600 rpm. For comparison, Fe@TAB and commercial Pt/C (20 wt%) were also tested under the same conditions. As shown in **Figure 2.13a**, the half potential of Fe@Aza-PON is 13 mV higher than that of Pt/C in alkaline condition (0.1 M aq. KOH solution). The Tafel slopes of Fe@Aza-PON, Fe@TAB and Pt/C are 60, 112 and 90 mV decade^{-1} from the Koutecky-Levich (K-L) equation, respectively (**Figure 2.13b**). In acidic condition (0.1 M aq. HClO$_4$) (**Figure 2.15**), the values are 116, 250 and 142 mV decade^{-1}. The lowest Tafel slope for the Fe@Aza-PON in both conditions indicates the fastest kinetics. In addition, the yield of peroxide species (HO$_2^-$ and H$_2$O$_2$) was found to be below 15%, which corresponds to an electron transfer number (n) of ~3.7 in both conditions (**Figure 2.16**). A number close to 4 indicates that the ORR mechanism proceeds kinetically with a favorable 2-step pathway.[36]

The different performances of the Fe@Aza-PON and Fe@TAB can be explained by their structural differences. A high Fe/Fe$_3$C ratio along with high pyridinic N can contribute to high ORR activity (see **Table 2.1**).[3,6,37] In addition, the polar phenazine-based structure in the Aza-PON not only assists oxygen diffusion[26,38] but also promotes oxygen activation.[25]
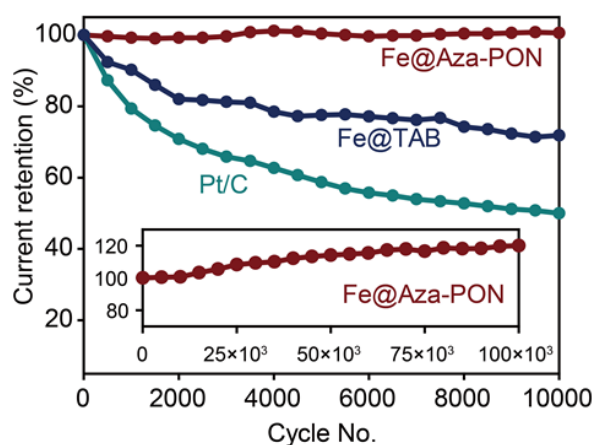
Figure 2.17. Current retention with respect to **chronoamperometric** cycling 0.1 M aq. HClO$_4$ solution. Inset: 100 000 cycles of Fe@Aza-PON (scan rate: 100 mV s^{-1}).

Like other reported Fe-N-C and Fe/Fe$_3$C systems,[6,9,11,13,29] the Fe@Aza-PON catalyst showed ORR activity similar to Pt/C. However, it displayed superior durability, showing high current retention (zero loss) even after 100,000 cycles (**see** insets in **Figure 2.13c, 2.17-2.18**). Compared to other Fe-N-C and Fe/Fe$_3$C systems (**Table 2.2**), the unusual stability of Fe@Aza-PON stems from its indirect-contact ORR catalysis, which can be realized thanks to the void-free encapsulation of the Fe nanoparticle cores in graphitic shells. The electrochemically stable graphitic shells are not only able to protect the Fe nanoparticle cores from oxidation (rusting), but also allow efficient electron tunneling for efficient ORR catalysis.

These structural advantages contribute to durable catalytic activity and protection from impurities such as methanol crossover (**Figure 2.13d**) and CO poisoning (**Figure 2.18**).[39,40]

Table 2.2. ORR stability of Fe-N-C, Fe/Fe$_3$C and other literature reported nonprecious metal composites compared to Fe@Aza-PON

Catalyst	Condition	After 10,000 cycles	Reference
Fe@Aza-PON	0.1 M KOH	Fig. 3c, Fig. S14: Below 1 mV negative shift in both condition, scan rate 100 mV s^{-1} (maintained 100% original current density even after 100 000 cycles) Fig. S15 (10,000 cycles) : ~0.9 mV in 0.1 M KOH ~11 mV in 0.1 M HClO$_4$	Fig. 3c, Fig. S14 Fig. S15
	0.1 M HClO$_4$		
Fe@TAB	0.1 M KOH	Fig. 3c, Fig. S14: 86.88% (KOH) 11 mV negative shift Fig. 15: ~18 mV	Fig. 3c, Fig. S14-15
	0.1 M HClO$_4$	Fig. 3c, Fig. S14: 71.84% (HClO$_4$) 16.8 mV negative shift Fig. S15: ~32 mV	
Fe@C-FeNC-2	0.1 M KOH	16 mV negative shift (5,000 cycles)	*J. Am. Chem. Soc.* **2016**, 138, 3570
Fe-N-C	0.1 M KOH	4 mV negative shift (5,000 cycles)	*Nanoscale*, **2015**, 7, 7644
HQDC-1000	0.1 M KOH	93%	*Sci. Rep.* **2015**, 5, 17064
(Fe,Co)@NGC	0.1 M KOH	~95%	*Chem. Commun.* **2015**, 51, 10479
FeCo-OMPC	0.1 HClO$_4$	24 mV negative shift	*Sci. Rep.* **2013**, 3, 2715
Meso-Fe-N-C/N-G	0.1 M KOH	~8.1 mV negative shifts in KOH (5,000 cycles) 95.3% (KOH) after 10,000 s	*J. Mater. Chem. A*, **2017**, 5, 4868
	0.1 M HClO$_4$	92.3% (HClO$_4$) after 10,000 s	
Fe-Phen-N-800	0.1 M KOH	13 mV negative shift (KOH)	*J. Mater. Chem. A*, **2016**, 4, 19037
	0.1 M HClO$_4$	19 mV negative shift (HClO$_4$)	
Fe$_3$C/NG-800	0.1 M KOH	5 mV negative shift (KOH)	*Adv. Mater.* **2015**, 27, 2521
	0.1 M HClO$_4$	11 mV negative shift (HClO$_4$)	
Fe-8CBDZ	0.1 M H$_2$SO$_4$	94%	*Adv. Energy Mater.* **2014**, 4, 1301735
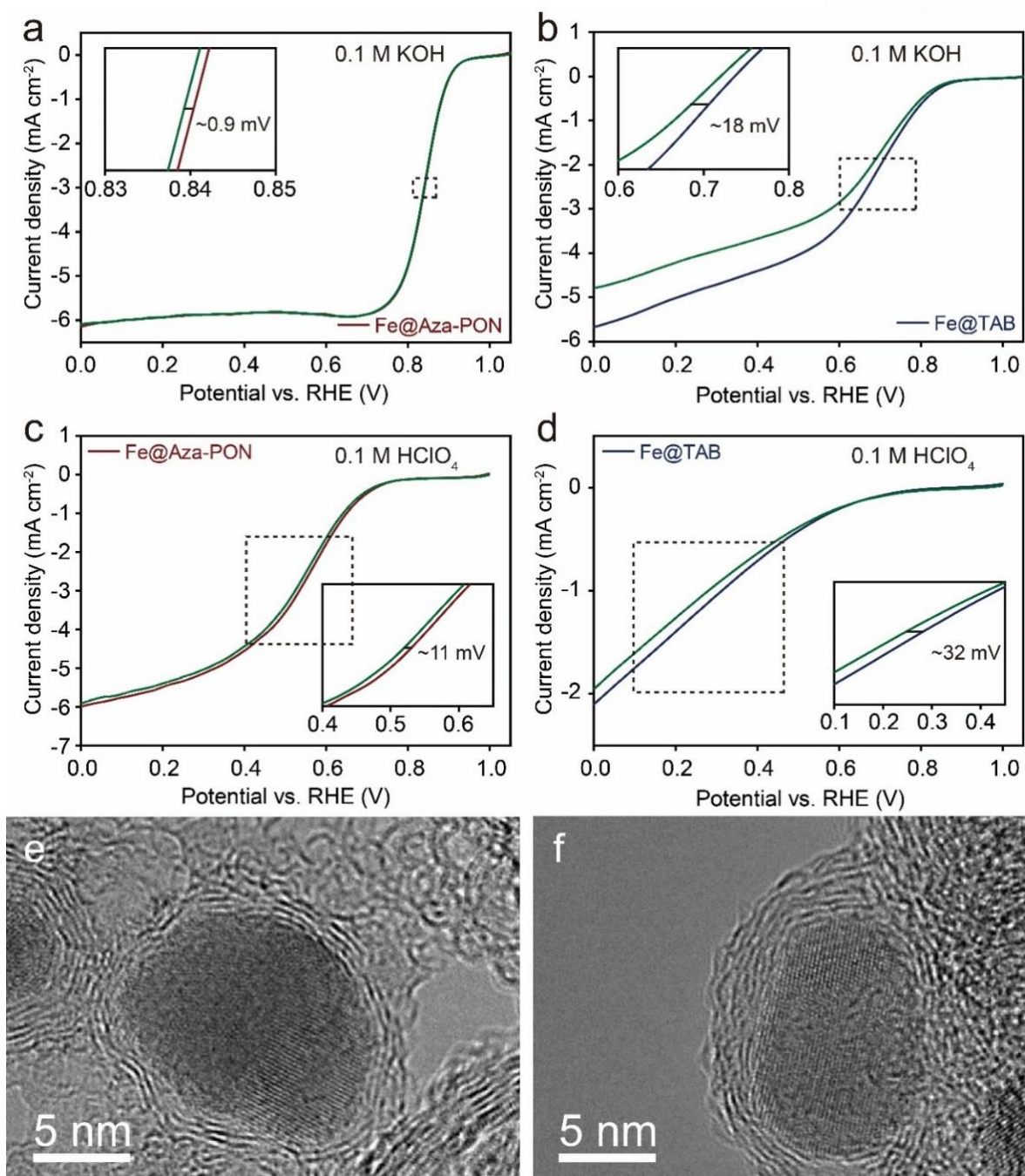
Figure 2.18. Rotating ring-disk electrode (RRDE) voltammograms after 10,000 cycles in both aq. KOH (0.1 M) and aq. $HClO_4$ (0.1 M) solutions. (a, c) LSV curves of Fe@Aza-PON. (b, d) LSV curves of Fe@TAB. Dark green curve: after 10,000 cycles. Insets in (a-d): resulting negative shifts after 10,000 cycles (30 μg of catalyst amount was loaded, scan rate: 10 mV s^{-1} at 1600 rpm). TEM images of Fe@Aza-PON: (e) 0.1 M aq. KOH and (f) 0.1 M aq. $HClO_4$ after 10,000 cycles.
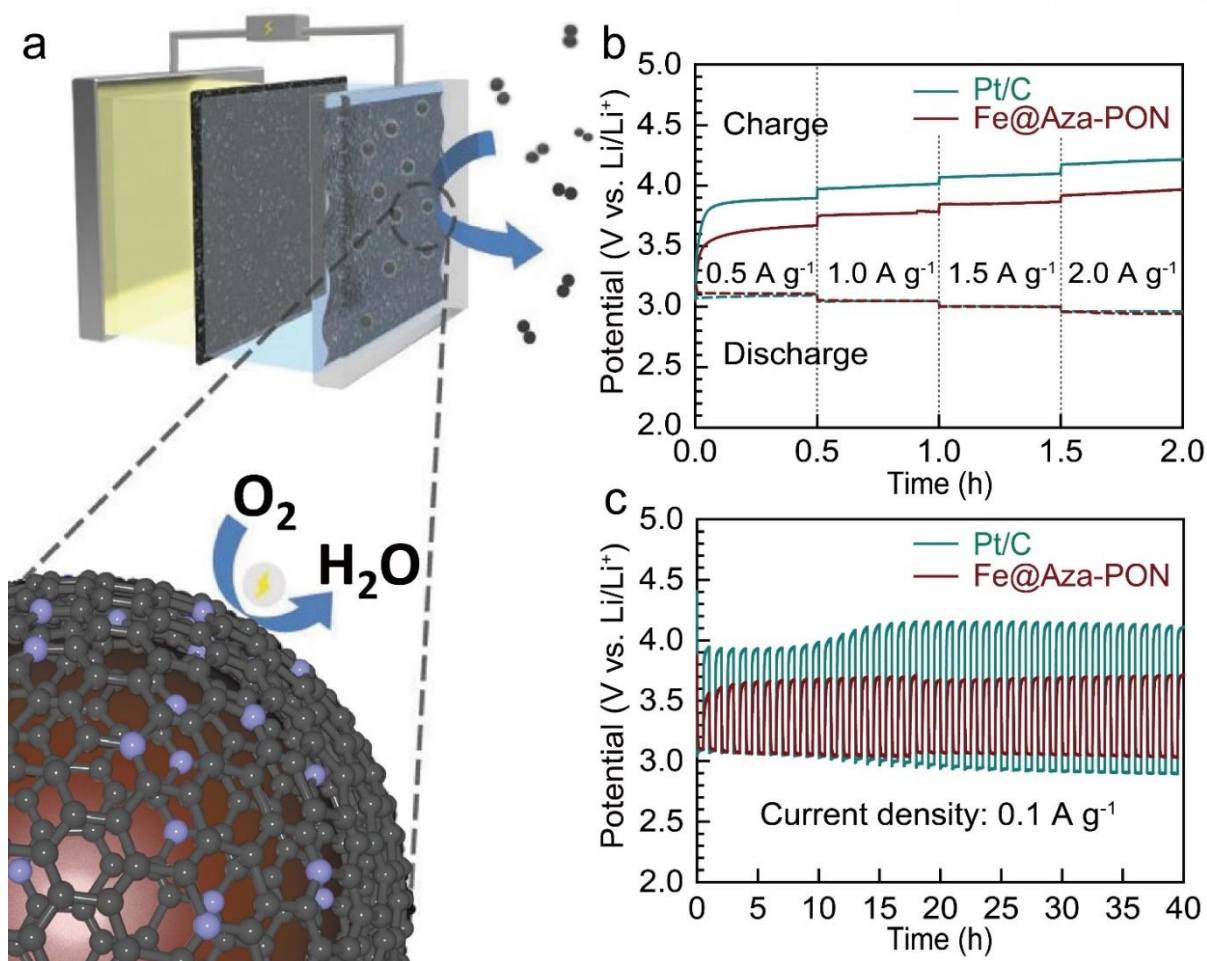
Figure 2.19. (a) Illustration of Li-Air cell system with Fe@Aza-PON. (b) Discharge-charge curves of Pt/C and Fe@Aza-PON, respectively, in 0.5 M LiOH with 1.0 M LiNO$_3$ at each current density. (c) cycling performance at 0.1 A g^{-1}.

As a potentially practical application, Fe@Aza-PON was tested in a hybrid Li-air cell (**Figure 2.19a**).[41,42] **Figure 2.19b** shows the first discharge-charge curves of Fe@Aza-PON and Pt/C in 0.5 M aq. LiOH/1.0 M aq. LiNO$_3$ electrolytes at different current densities, in the range of 0.5 to 2.0 A g^{-1}. The discharge voltage plateau was observed at around 3.1 V for both the Fe@Aza-PON and Pt/C at a current density of 0.5 A g^{-1}.

At the same time, the Fe@Aza-PON exhibited superior performance with respect to its oxygen evolution reaction (OER) activity during the charging process. The charge plateaus were observed at 3.67 and 3.90 V, respectively, for Fe@Aza-PON and Pt/C at the current density of 0.5 A g^{-1}. These outstanding electrocatalytic properties can be attributed to the robust void-free encapsulation of Fe nanoparticles in the Fe@Aza-PON, while the Pt/C is vulnerable to OER process.[41,42]
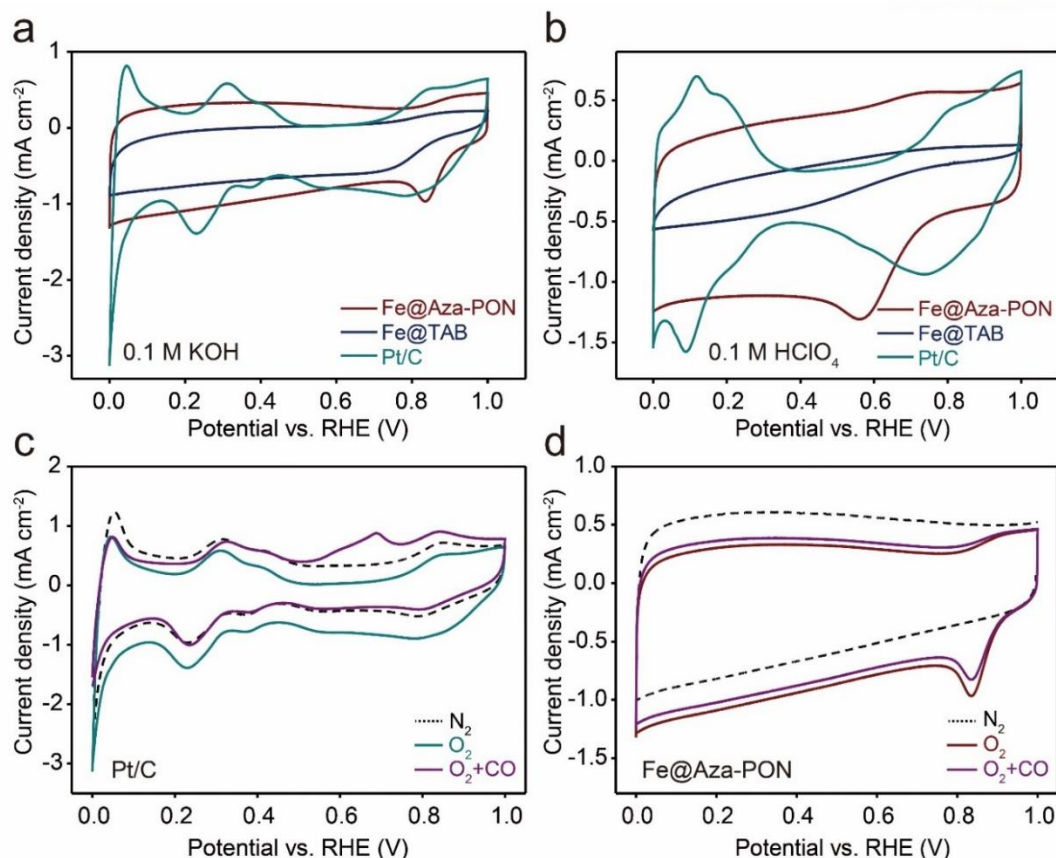
Figure 2.20. CV curves of samples in oxygen-saturated condition. (a) in alkaline medium (0.1 M KOH), (b) in acidic medium (0.1 M HClO$_4$). CO poisoning tests (0.1 M KOH): (c) Pt/C, (d) Fe@Aza-PON. The amount of sample loading in each case was 20 μg (scan rate: 10 mV s^{-1}).

As shown in **Figure 2.19c**, the cycling performance of Pt/C at a constant current density of 0.1 A g^{-1} was substantially degraded with an increase in the discharge-charge voltage gap from 0.85 V to 1.21 V. However, the Fe@Aza-PON exhibited constant cycling performance for 40 h (the voltage gap remained less than 0.7 V). Based on these results, the Fe@Aza-PON catalyst was determined to be an efficient bifunctional catalyst with performance comparable to the benchmark Pt/C in a hybrid Li-air cell.

2.4 Conclusions

We introduced a high-quality iron (Fe)-based oxygen reduction reaction (ORR) catalyst, consisting of Fe nanoparticle cores stably encapsulated in nitrogenated graphitic shells, which were uniformly distributed in a phenazine-based porous organic network (Aza-PON). To realize a stable catalytic structure, the two-dimensional (2D) fused aromatic Aza-PON was key, providing feedstock for the formation of defect-free graphitic shells to protect unstable Fe nanoparticle cores. The well-defined graphitic shells also efficiently facilitated electron tunneling and provided abundant pyridinic N sites for enhanced oxygen diffusion. Due to its structural benefits, the Fe@Aza-PON catalyst displayed

comparable ORR activity, and superior durability, to commercial Pt/C.

Moreover, the bifunctional Fe@Aza-PON catalyst exhibited promising practical performance in a full hybrid Li-air battery cell. Based on this study, the synthesis strategy suggests two important features: (1) the 2D fused aromatic PON forms better void-free encapsulation of vulnerable metallic nanoparticles for improved stability; and (2) considering the availability of various building blocks for the PON syntheses, and non-precious metals, the new design and synthesis of indirect-contact catalysts is very promising for various additional applications.

2.5 Experimental Methods

2.5.1 Synthesis of the Fe@Aza-PON catalyst

Into a 3-necked round flask, 1,2,4,5-benzenetetramine tetrahydrochloride (1.1 g, 3.87 mmol), hexaketocyclohexane octahydrate (0.8 g, 2.56 mmol), iron (III) chloride (1.0 g, 6.17 mmol) and anhydrous N-methyl-2-pyrrolidinone (NMP, 80 mL) were placed. The mixture was stirred at 150 °C under nitrogen atmosphere for 8 h. After cooling to room temperature, sodium borohydride (NaBH$_4$, 10 wt%, 40 mL NMP) was slowly added then heated again at 150 °C for 5 h. The crude was poured into distilled water (1.5 L). The black precipitates were collected by filtration through polytetrafluoroethylene (PTFE, 0.45 μm) and Soxhlet extracted with water and methanol for 3 days. Then, freeze-dried (at −120 °C under 10^{-5} mmHg) for 48 h. The black powders were heat-treated at different temperature under argon atmosphere for 2 h. After heat-treatment, the samples were leached with 3.0 M aq. HCl for 24 h. Finally, the samples were repeatedly washed with distilled water and freeze-dried for 48 h.

2.5.2 Synthesis of Fe@TAB

The procedure is similar to Fe@Aza-PON. For the preparation of Fe@TAB (**Figure 2.11**), hexaketocyclohexane octahydrate was not used. Into a 3-necked round bottom flask, 1,2,4,5-benzenetetramine tetrahydrochloride (1.1 g, 3.87 mmol), iron (III) chloride (1.0 g, 6.17 mmol) and anhydrous N-methyl-2-pyrrolidinone (NMP, 80 mL) were placed. The mixture was stirred at 150 °C under nitrogen atmosphere for 8 h. After cooling to room temperature, sodium borohydride (NaBH$_4$, 10 wt%, 40 mL NMP) was slowly added then heated again at 150 °C for 5 h. The crude was poured into distilled water (1.5 L). The black precipitates were collected by filtration through polytetrafluoroethylene (PTFE, 0.45 μm) membrane and Soxhlet extracted with water and methanol for 3 days each. Then, freeze-dried (at −120 °C under 10^{-5} mmHg) for 48 h. The black powders were heat-treated at different temperature under argon atmosphere for 2 h. After heat-treatment, the samples were leached with 3.0 M aq. HCl for 24 h. Finally, the samples were repeatedly washed with distilled water and freeze-dried for 48 h.

2.5.3 Preparation of hybrid Li-air cell

A lithium metal foil (0.2 mm thickness) was purchased from Honjo Metal and the disk with a diameter of 1.0 cm were prepared for use as the anode. 1.0 M lithium hexafluorophosphate (LiPF$_6$, Sigma-Aldrich Co.) in tetraethylene glycol dimethyl ether (TEGDME, Sigma-Aldrich Co.) was used as an organic anolyte, and 0.5 M lithium hydroxide (LiOH, Sigma-Aldrich Co.) + 1.0 M lithium nitrate (LiNO$_3$, Sigma-Aldrich Co.) in distilled water was used as an aqueous catholyte. Li$_{1+x+y}$Ti$_{2-x}$Al$_x$P$_{3-y}$Si$_y$O$_{12}$ (0.15 mm thickness) solid Li-ion conducting ceramic glass (OHARA Inc.) used as a separator between anolyte and catholyte. The catalyst ink (10 mg mL^{-1}) was prepared by dispersing in the binder stock solution. The binder stock solution is mixture with a volumetric ratio of 45:45:10 for ethanol, isopropyl alcohol, and Nafion (5 wt.%, Sigma-Aldrich Co.), respectively. An air electrode was prepared by drop-coating the catalyst ink onto a gas-diffusion layer (Toray TGP-H-090) with loading density of 1.0 mg cm^{-2}. The applied current densities are normalized by the loading weight of catalyst. Titanium metal mesh was used as a current collector onto the gas diffusion layer and electrochemical measurements were conducted on a Biologic VMP3 at ambient air conditions.

2.6 Materials

All reagents and solvents were purchased from Sigma-Aldrich Chemical Inc., unless otherwise stated. Solvents were degassed with nitrogen purging prior to use. All reactions were performed under nitrogen atmosphere using oven dried glassware.

2.7 Instrumentations

Powder X-ray diffraction (PXRD) studies were taken on a High-Power X-Ray Diffractometer D/MAX 2500V/PC (Cu–Kα radiation, 40 kV, 200 mA, λ = 1.54056 Å) (Rigaku Inc., Japan). High-resolution transmission electron microscopy (HR-TEM) was performed by using a JEM-2100F microscope (JEOL Inc., Japan) under an operating voltage of 200 keV. The samples for TEM images were prepared by dropping dispersed NMP solution on holey carbon TEM grid and dried in oven at 80 °C under reduced pressure. X-ray photoelectron spectroscopy (XPS) was performed on an X-ray Photoelectron Spectrometer Thermo Fisher K-alpha (UK). Thermogravimetric analysis (TGA) was conducted in air and in nitrogen atmosphere at a ramping rate of 10 °C min^{-1} using a Thermogravimetric Analyzer Q200 (TA Instrument Inc., USA). Scanning electron microscope (SEM) images were taken with a Field Emission Scanning Electron Microscope Nanonova 230 (FEI Inc., USA). The surface area was calculated by nitrogen adsorption-desorption isotherms using the Brunauer-Emmett-Teller (BET) method on BELSORP-max (BEL Japan Inc., Japan). Elemental analysis was conducted with a Flash 2000 Analyzer (Thermo Scientific Inc., USA).

2.8 Electrochemical analysis

For all samples in this work, a typical ink preparation procedure was used. Briefly, 5 mg sample and 40 μL Nafion solution were dispersed in 1 ml isopropyl alcohol/water solution with a volume ratio of 1:4, followed by ultrasonication for 30 minutes to form homogeneous catalyst inks. To test electrochemical catalyst performance and stability, three-neck electrode cell and potentiostat (1470E, Solartron, UK) were used. Pt gauze was used as a counter electrode and Ag/AgCl as a reference electrode, which is stored in saturated KCl. The working electrodes were prepared by drop casting catalyst inks onto the glassy carbon (GC) disk electrodes. The 20 μg of catalyst ink was loaded on working electrodes and further dried thoroughly at room temperature prior to measurements. The prepared sample electrodes were tested at ambient condition in each medium (0.1M aq. KOH and 0.1M aq. $HClO_4$) under oxygen (O_2) saturated condition. The 100,000 cycles stability of Fe@Aza-PON, Fe@TAB and Pt/C (Figure 2.13c, Figure 2.17) were conducted in acid and alkaline media at a scan rate of 100 mV s^{-1}. The CO poisoning tests (Figure 2.20c-d) were performed by the same method (scan rate of 10 mV s^{-1}).

Rotating ring-disk electrode (RRDE) measurement were carried out using CompactStat.h as a potentionstat (Ivium Inc., NED) and RRDE-3A (ALS Co., Japan). The 30 μg of catalyst was loaded onto a RRDE (4 mm in diameter, 0.1256 cm^2 surface area) and dried at ambient condition prior to electrochemical tests. Linear sweep voltammetry was measured in O_2 saturated 0.1 M aq. KOH and $HClO_4$ at a scan rate of 10 mV s^{-1} with a rotation speed of 1600 rpm (Figure 2.13a, 2.15). The ring potential was constant at 0.4 and 0.9 V vs. Ag/AgCl in each solution respectively. For checking the stability, the scanning was maintained up to 10,000 cycles (Figure 2.18a-d). The % hydrogen peroxide concentration was calculated by concentration (%) $= 200 \times \frac{I_r}{N} \div (I_d + \frac{I_r}{N})$ relation and electron transfer number (n) was determined by $n = 4 \times \frac{I_d}{I_d + I_r/N}$ equation (I_d is disk current, I_r is ring current and N is current collection efficiency of Pt ring. N was determined to be 0.424 from the reduction of $K_3Fe[CN]_6$) (Figure 2.16). The Tafel plot was derived from $\frac{1}{i_m} = \frac{1}{i_l} + \frac{1}{i_k}$ relation (i_m means measured current, i_l is limiting current, i_k is kinetic current).[1,2] Methanol crossover experiments were performed using rotating disk electrode (RDE) by loading 20 μg of catalyst on glassy carbon RDE (3 mm diameter, 0.0706 cm^2 surface area). The current–time (j–t) chronoamperometric response (Figure 2.13d) at 0.5 V (vs. RHE) at a rotation rate of 2,500 rpm in 0.1 M aq. KOH with the addition of 3 M methanol (2 mL).

2.9 REFERENCES

(1)   Elmer, T.; Worall, M.; Wu, S. Y.; Riffat, S. B. *Renew. Sustainable Energy Rev.* **2015**, *42*, 913.

(2)   Zhou, X. J.; Qiao, J. L.; Yang, L.; Zhang, J. J. *Adv. Energy Mater.* **2014**, *4*, 1301523.

(3)   Hu, Y.; Jensen, J. O.; Zhang, W.; Cleemann, L. N.; Xing, W.; Bjerrum, N. J.; Li, Q. F. *Angew. Chem. Int. Ed.* **2014**, *53*, 3675.

(4)   Jaouen, F.; Goellner, V.; Lefevre, M.; Herranz, J.; Proietti, E.; Dodelet, J. P. *Electrochim. Acta.* **2013**, *87*, 619.

(5)   Li, J. S.; Li, S. L.; Tang, Y. J.; Han, M.; Dai, Z. H.; Bao, J. C.; Lan, Y. Q. *Chem. Commun.* **2015**, *51*, 2710.

(6)   Xiao, M. L.; Zhu, J. B.; Feng, L. G.; Liu, C. P.; Xing, W. *Adv. Mater.* **2015**, *27*, 2521.

(7)   Liu, J.; Song, P.; Ning, Z. G.; Xu, W. L. *Electrocatalysis* **2015**, *6*, 132.

(8)   Shao, M. H.; Chang, Q. W.; Dodelet, J. P.; Chenitz, R. *Chem. Rev.* **2016**, *116*, 3594.

(9)   Huo, L. L.; Liu, B. C.; Zhang, G.; Si, R.; Liu, J.; Zhang, J. *J. Mater. Chem. A* **2017**, *5*, 4868.

(10)   Sanetuntikul, J.; Shanmugam, S. *Nanoscale* **2015**, *7*, 7644.

(11)   Kim, J. H.; Sa, Y. J.; Jeong, H. Y.; Joo, S. H. *ACS Appl. Mater. Interfaces* **2017**, *9*, 9567.

(12)   Jiang, W. J.; Gu, L.; Li, L.; Zhang, Y.; Zhang, X.; Zhang, L. J.; Wang, J. Q.; Hu, J. S.; Wei, Z. D.; Wan, L. J. *J. Am. Chem. Soc.* **2016**, *138*, 3570.

(13)   Serov, A.; Artyushkova, K.; Atanassov, P. *Adv. Energy Mater.* **2014**, *4*, 1301735.

(14)   Cooper, A. I. *Adv. Mater.* **2009**, *21*, 1291.

(15)   Jiang, J. X.; Su, F.; Trewin, A.; Wood, C. D.; Niu, H.; Jones, J. T. A.; Khimyak, Y. Z.; Cooper, A. I. *J. Am. Chem. Soc.* **2008**, *130*, 7710.

(16)   Xu, Y. H.; Jin, S. B.; Xu, H.; Nagai, A.; Jiang, D. L. *Chem. Soc. Rev.* **2013**, *42*, 8012.

(17)   Chen, L.; Honsho, Y.; Seki, S.; Jiang, D. L. *J. Am. Chem. Soc.* **2010**, *132*, 6742.

(18)   Xu, Y. H.; Chen, L.; Guo, Z. Q.; Nagai, A.; Jiang, D. L. *J. Am. Chem. Soc.* **2011**, *133*, 17622.

(19)   Chen, L.; Yang, Y.; Guo, Z. Q.; Jiang, D. L. *Adv. Mater.* **2011**, *23*, 3149.

(20)   Chen, L.; Yang, Y.; Jiang, D. L. *J. Am. Chem. Soc.* **2010**, *132*, 9138.

(21)   Jiang, J. X.; Su, F.; Niu, H.; Wood, C. D.; Campbell, N. L.; Khimyak, Y. Z.; Cooper, A. I. *Chem. Commun.* **2008**, 486.

(22)   Ren, S.; Dawson, R.; Laybourn, A.; Jiang, J. X.; Khimyak, Y.; Adams, D. J.; Cooper, A. I. *Polym. Chem.* **2012**, *3*, 928.

(23)   Xie, Y.; Wang, T. T.; Liu, X. H.; Zou, K.; Deng, W. Q. *Nat. Commun.* **2013**, *4*, 1960.

(24)   Kou, Y.; Xu, Y. H.; Guo, Z. Q.; Jiang, D. L. *Angew. Chem. Int. Ed.* **2011**, *50*, 8753.

(25)   Briega-Martos, V.; Ferre-Vilaplana, A.; de la Pena, A.; Segura, J. L.; Zamora, F.; Feliu, J. M.; Herrero, E. *ACS Cat.* **2017**, *7*, 1015.

(26)   Guo, D. H.; Shibuya, R.; Akiba, C.; Saji, S.; Kondo, T.; Nakamura, J. *Science* **2016**, *351*, 361.

(27)   Merzoug, M.; Zouchoune, B. *J. Organomet. Chem.* **2014**, *770*, 69.

(28)   Cheon, J. Y.; Kim, T.; Choi, Y.; Jeong, H. Y.; Kim, M. G.; Sa, Y. J.; Kim, J.; Lee, Z.; Yang, T. H.; Kwon, K.; Terasaki, O.; Park, G. G.; Adzic, R. R.; Joo, S. H. *Sci. Rep.* **2013**, *3*, 2715.

(29)   Yang, Z. K.; Zhao, Z. W.; Liang, K.; Zhou, X.; Shen, C. C.; Liu, Y. N.; Wang, X.; Xu, A. W. *J. Mater. Chem. A* **2016**, *4*, 19037.

(30)   Zitolo, A.; Goellner, V.; Armel, V.; Sougrati, M. T.; Mineva, T.; Stievano, L.; Fonda, E.; Jaouen, F. *Nat. Mater.* **2015**, *14*, 937.

(31)   Bonnet, F.; Ropital, F.; Lecour, P.; Espinat, D.; Huiban, Y.; Gengembre, L.; Berthier, Y.; Marcus, P. *Surf. Interface Anal.* **2002**, *34*, 418.

(32)   Herrmann, I. K.; Grass, R. N.; Mazunin, D.; Stark, W. J. *Chem. Mater.* **2009**, *21*, 3275.

(33)   Giordano, C.; Kraupner, A.; Wimbush, S. C.; Antonietti, M. *Small* **2010**, *6*, 1859.

(34)   Kumar, P. V.; Bardhan, N. M.; Tongay, S.; Wu, J.; Belcher, A. M.; Grossman, J. C. *Nat. Chem.* **2014**, *6*, 151.

(35)   Wang, Z.; Yang, X.; Xu, M.; Wei, J.; Liu, X. *J. Mater. Sci. Mater. Electron.* **2013**, *24*, 2610.

(36)   Dai, L. M.; Xue, Y. H.; Qu, L. T.; Choi, H. J.; Baek, J. B. *Chem. Rev.* **2015**, *115*, 4823.

(37)   Lee, J.-S.; Park, G. S.; Kim, S. T.; Liu, M.; Cho, J. *Angew. Chem. Int. Ed.* **2013**, *52*, 1026.

(38)   Rao, C. V.; Cabrera, C. R.; Ishikawa, Y. *J. Phys. Chem. Lett.* **2010**, *1*, 2622.

(39)   Heinzel, A.; Barragan, V. M. *J. Power Sources* **1999**, *84*, 70.

(40)   Mehmood, A.; Scibioh, M. A.; Prabhuram, J.; An, M. G.; Ha, H. Y. *J. Power Sources* **2015**, *297*, 224.

(41)   Kim, C.; Gwon, O.; Jeon, I. Y.; Kim, Y.; Shin, J.; Ju, Y. W.; Baek, J. B.; Kim, G. *J. Mater. Chem. A* **2016**, *4*, 2122.

(42)   Li, L. J.; Manthiram, A. *Adv. Energy Mater.* **2014**, *4*, 1301795.

III. A Robust 3D Cage-like Ultramicroporous Network Structure with High Gas-Uptake Capacity

3.1 Abstract

Uncertainties in energy supply and resource depletion, climate change and the rising costs of conventional energy sources present significant challenges to current research. To tackle these issues, the storage of hydrogen (H_2), methane (CH_4) and carbon dioxide (CO_2) by adsorption in porous materials at relatively low pressure and ambient temperature has been proposed as a solution. Here, we report a three-dimensional (3D) cage-like organic network (3D-CON) structure synthesized *via* the straightforward condensation of building blocks designed with gas adsorption properties. The 3D-CON can be prepared using an easy but powerful route, which is essential for commercial scale-up. The resulting fused aromatic 3D-CON exhibited a high Brunauer-Emmett-Teller (BET) specific surface area of up to 2247 $m^2 g^{-1}$. More importantly, the 3D-CON displayed outstanding low pressure hydrogen (H_2, 2.64 wt%, 1.0 bar and 77 K), methane (CH_4, 2.4 wt%, 1.0 bar and 273 K) and carbon dioxide (CO_2, 26.7 wt%, 1.0 bar and 273 K) uptake with a high isosteric heat of adsorption (H_2, 8.10 kJ mol^{-1}; CH_4, 18.72 kJ mol^{-1}; CO_2, 31.87 kJ mol^{-1}). These values are among the best reported for organic networks with high thermal stability (~600 °C).

3.2 Introduction

With the growing consumption of fossil fuels and demand for clean energy, worldwide environmental problems and gas storage needs have become increasingly important.[1-4] Organic porous materials (OPMs) are considered fundamentally valuable for capturing carbon dioxide (CO_2)[5] and the safe storage of clean energy resources[2] as well as explosive industrial gases (*e.g.*, methane, CH_4).[6-7] Among clean energy sources, hydrogen (H_2) has long been regarded as one of the best alternatives to replace fossil fuels. It outperforms the others, because it possesses the highest heat of combustion, and water is the only by-product after combustion.[8]

Recent efforts have been undertaken to improve the design of porous materials and develop processes which result in intrinsic porosities, with the goal of enhancing H_2 and CH_4 storage, and CO_2 capture.[9-11] A notable area of progress in porous materials research has been the evolution of porous high crystallinity metal-organic frameworks (MOFs), which are constructed from metal ions and organic linkers using reticular chemistry.[12-13] Many of these interesting materials have been reported to have the highest surface area and gas uptake capacity among all porous materials.[13-14] However, despite their huge flexibility in design and diversity of structure, MOFs inevitably contain a considerable amount of metal centers and relatively weak coordination bonds, which can badly hamper their applications.[15] The

poor stability problems might be resolved by substituting susceptible chemical coordination bonds with stronger covalent bonds, as has been demonstrated using covalent organic frameworks (COFs) and porous polymeric materials (PPMs).[9, 16-17]

OPMs (COFs and PPMs) are constructed from lightweight building blocks with strong covalent bonding, and have attracted a great amount of scientific and technological curiosity, while achieving critical importance in many applications such as gas storage, catalysis and gas separation.[9, 16] These OPMs generally possess stable and perpetual porosity, synthetic diversity, low mass densities and physiochemical stability, which makes them immensely competitive in gas storage applications.[18-21] Further vigorous and intensive efforts are underway to produce OPMs with higher surface areas *via* different strategies.[9]

To fabricate stable OPMs, it is typically necessary to apply rigid building blocks (repeating units) that prevent the collapse of the framework and fill the volume space in a more periodic manner. OPM rigidity is usually created by fusing repeating aromatic units. However, while significant progress has been made in developing robust OPMs,[22] a better understanding of methods for fabricating rigid structures with permanent pores using light elements is still highly desired.
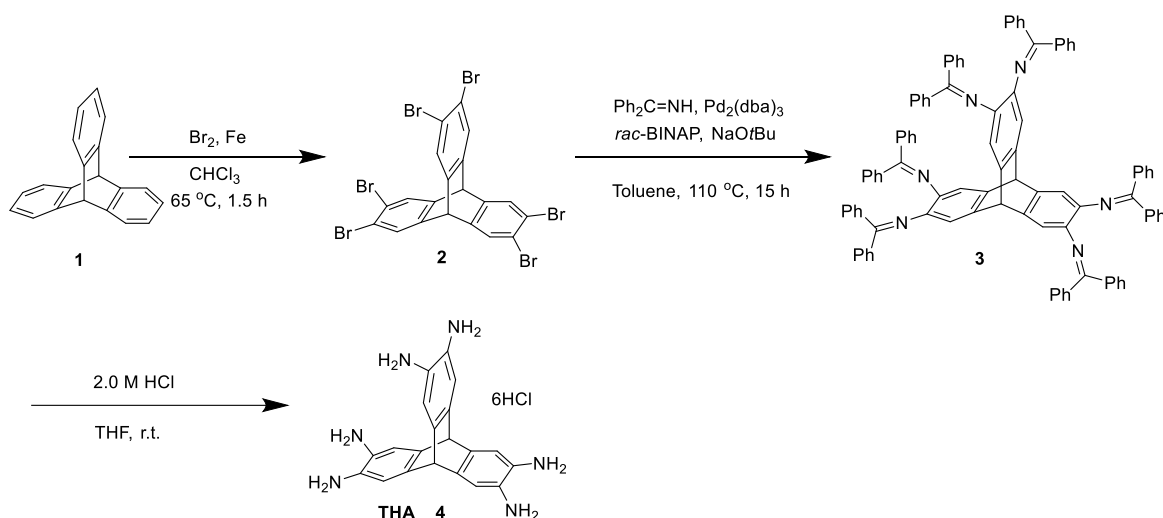
Figure 3.1. Synthetic scheme triptycenehexaamine (THA) hexahydrochloride.[1] Key procedure to afford pure THA is hydrochlorination, since *ortho*-amino groups in THA are unstable against oxidation.

In the pursuit of high performance OPMs, we employed a strategy based on insights about the C_2N structure,[23] to realize a uniformly microporous robust 3D cage-like organic network (CON) structure by the condensation of triptycene-based hexamine (THA)[24] and hexaketocyclohexane (HKH) octahydrate (**Figure 3.1; Figure 3.2**). The resulting 3D-CON has a high Brunauer-Emmett-Teller (BET) specific surface area as well as good thermal and physiochemical stability. In addition to its exceptional surface area, the as-produced 3D-CON outperformed highly porous MOFs in thermal and hydrothermal stability and demonstrated great potential for H_2 and CH_4 storage as well as CO_2 capture.
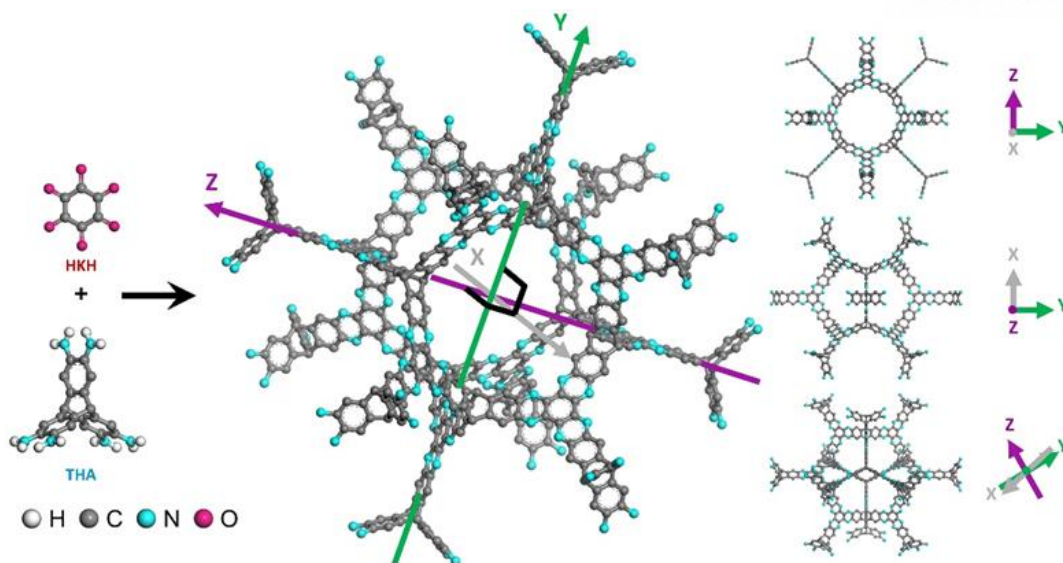
Figure 3.2. Schematic illustration of robust 3D-CON structure. Triptycene-based hexamine (THA) and hexaketocyclohexane (HKH) in ethylene glycol and acetic acid (3 M) mixture used to form the 3D-CON. The three structures on the right side are from the different view angle.

3.3 Results and discussion

The condensation reaction between THA and HKH spontaneously results in the irreversible formation of fused aromatic pyrazine rings without the use of an expensive catalyst. The structure of resulting material is highly stable in a practical range of thermal and physiochemical conditions.

Since 3D network structures result in a higher surface area compared to two-dimensional (2D) framework structures, a potential multifunctional candidate (monomer) with 3D topology was deliberately selected to synthesize the 3D-CON in this study. This [3+3] condensation with THA used to form the pyrazine rings has never been previously exploited. Triptycene is considered a promising unit for the synthesis of 3D-CONs with good gas storage performance, because it has a special 'internal free volume' feature.[25-27] Moreover, the presence of periodic nitrogen atoms, aromatic phenyl and pyrazine rings in the 3D-CON are very useful for the adsorption and desorption of gases and other metals in the structure.

After completing the condensation reaction between the THA and HKH, a monolithic solid gel-like material was formed, and the reaction solvent (ethylene glycol) around the material was almost clean (**Figure 3.3a, b**), suggesting the complete digestion of the starting monomers. The subsequent Soxhlet extraction with water and methanol also confirmed the clean reaction (no monomer residues), with no color removal during the Soxhlet extraction process (**Figure 3.3c**). In the ethylene glycol and acetic acid mixture, the material looked black (**Figure 3.3a, b**). After the removal of ethylene glycol and acetic acid by washing with water, the material turned bright brown (**Figure 3.3c**) and the color remained after freeze drying, with an almost quantitative yield (**Figure 3.3d**).
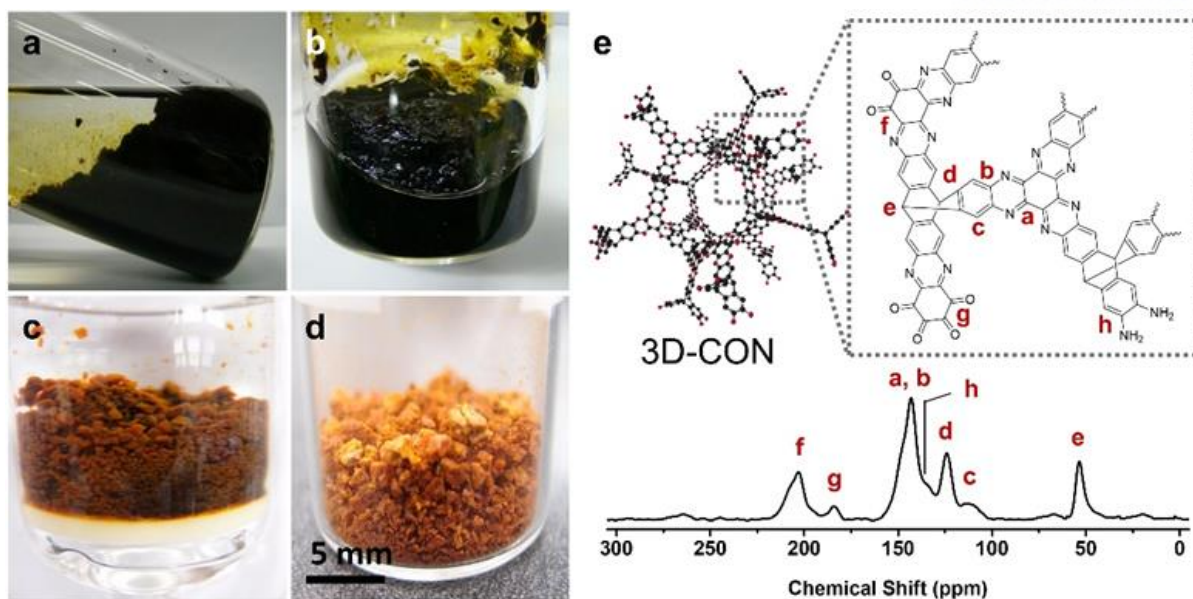
Figure 3.3. Digital images and NMR spectrum of 3D-CON. (**a**) Tilted Pyrex glass ampule showing the clean reaction solvent after completion of the reaction. (**b**) After draining the reaction solvent from the Pyrex glass ampule. (**c**) During Soxhlet extraction with water and methanol. (**d**) After freeze drying at −120 °C for four days under dynamic vacuum. (**e**) Solid-state ^{13}C CP-MAS NMR spectrum.

The bright brown color is due to the breaking of aromaticity by a barrelene-like moiety. It is this barrelene-like core in the THA that is responsible for the formation of the stable and high surface area material. Once the condensation between ortho-diamines in the THA and diketones in HKH occurs, a fused aromatic pyrazine ring forms a stable and rigid linker between the THA and HKH units. The resulting structure is highly rigid and retains a diamond-like structural stability, and also creates sufficient periodic micropores with greatly increased internal surface areas.

In addition, solid-state ^{13}C cross-polarization magic angle spinning (CP-MAS) nuclear magnetic resonance (NMR) spectroscopy also revealed that condensation of the starting monomers resulted in the complete transformation to pyrazine-linked fused aromatic rings (**Figure 3.2**). The solid-state ^{13}C CP-MAS NMR spectrum revealed seven carbon peaks with chemical shifts of 53.5, 113, 124.1, 133.63, 143, 184 and 203 ppm, which can be assigned to the sp^3 bridge carbon (e), aromatic (sp^2) carbons (a, b, c, d, h) and the edge carbonyl (C=O) groups (f, g), respectively (**Figure 3.3e**).

In order to investigate the long-range structure of the 3D-CON, powder X-ray diffraction (PXRD) and transmission electron microscopy (TEM) were performed. Although the peaks are broad due to the massive molecular size (∼∞), the PXRD pattern still revealed some order in the structure (**Figure 3.4a**). The 3D-CON material does not exhibit long range crystallographic ordering, but the locally ordered structure is expected to support a high surface area (*vide infra*).

Thermogravimetric analysis (TGA) revealed that the 3D-CON was thermally stable. When the

temperature was raised from 50 to 600 °C, less than 4% weight loss occurred (**Figure 3.4b**). The 3D-CON is insoluble in common organic solvents such as DMF, alcohols, acetone and organic acids, even after stirring at ambient condition for a long time (~ month), indicating that the 3D-CON framework possesses high chemical stability.

Transmission electron microscopy (TEM) images obtained from the dispersed sample revealed that the texture is sheet-like (**Figure 3.6a**), but at high resolution it exhibited uniform micropores (**Figure 3.6b, c**).

The bulk morphologies of the 3D-CON were visualized with field-emission scanning electron microscopy (FE-SEM). The 3D-CON showed uniform micropores and a clean morphology. Its grain size varied from tens to hundreds of micrometers, suggesting a fine microporous structure (**Figure 3.4c, d**). SEM coupled energy-dispersive spectroscopy (SEM-EDS) (**Figure 3.4e**) and SEM elemental mapping were used to corroborate the elemental composition of the 3D-CON. The presence of carbon (C), nitrogen (N) and oxygen (O) was confirmed in the SEM-EDS analysis by elemental mapping (**Figure 3.5**).
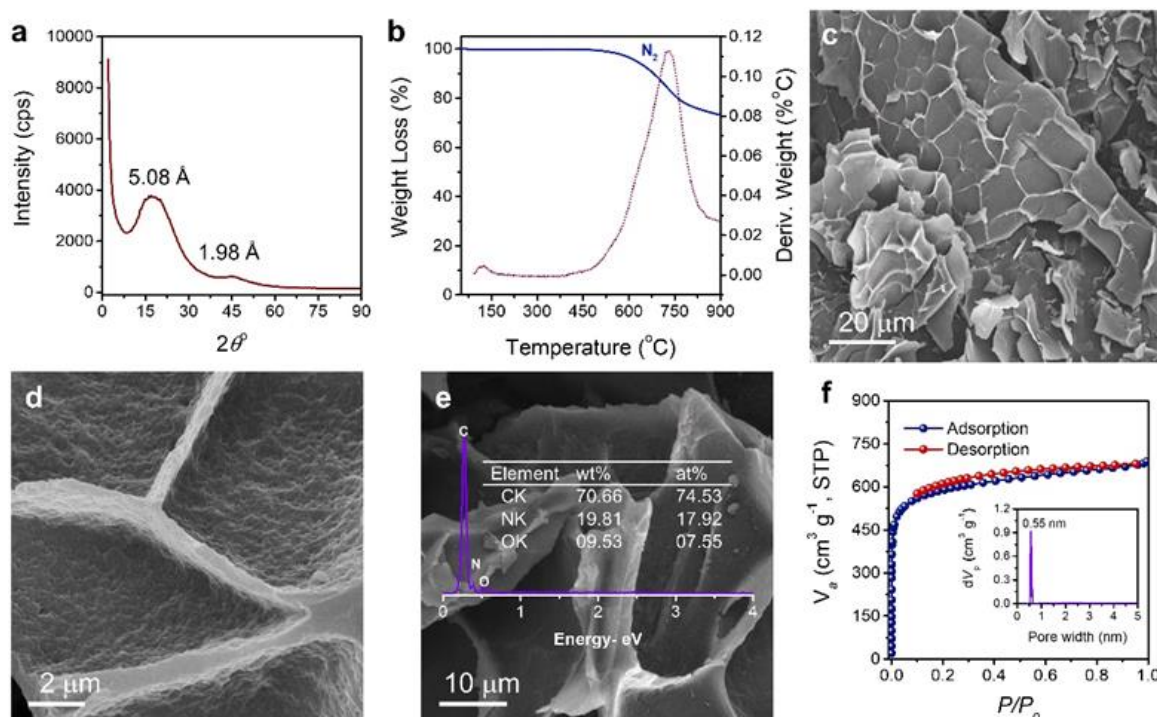
Figure 3.4. Structural characterization of the robust 3D-CON structure. (**a**) Powder X-ray diffraction (PXRD) pattern. (**b**) TGA curve of the as-prepared sample under nitrogen atmosphere after in situ activation at 150 °C in a TGA instrument, to remove any adsorbed guest molecules, at a ramping rate of 10 °C min^{-1}. (**c, d**) SEM images at different magnifications. (**e**) Energy dispersive X-ray spectroscopy (EDS) spectrum with corresponding SEM image, showing elemental contents. (**f**) Nitrogen adsorption and desorption isotherm at 77 K. The inset is the corresponding pore size distribution from the NLDFT approximation.

Using different elemental analyses techniques, the chemical composition of the 3D-CON was determined, and the results are summarized in **Table 3.1**. The X-ray photoelectron spectroscopy (XPS) technique was used to probe the bonding nature of the 3D-CON. The survey scan spectrum from the 3D-CON indicated the presence of C 1s, N 1s and O 1s without any other elements in the structure (**Figure 3.7a**). The peak, which appeared at 398.7 eV, was attributed to the characteristic sp^2-hybridized nitrogen atoms in the 3D-CON structure. In the high resolution XPS spectrum, C 1s can be deconvoluted into 284.3, 285.2 and 288.7 eV, which are assignable to sp^2 *C*-C and sp^2 *C*-N in the aromatic ring, and the minor peak at 288.7 eV is attributed to the *C*-heteroatoms, *e.g.*, sp^2 *C*=O and sp^2 *C*-NH$_2$ at the edges (**Figure 3.7b**). The N 1s peak shows one major peak at 398.7 eV for the pyrazine-like nitrogen in the structure (**Figure 3.7c**). The presence of the O 1s peak in the 3D-CON can be assigned to trapped moisture and/or oxygen in the pores and residual carbonyl (C=*O*) groups at the edges (**Figure 3.7d**).
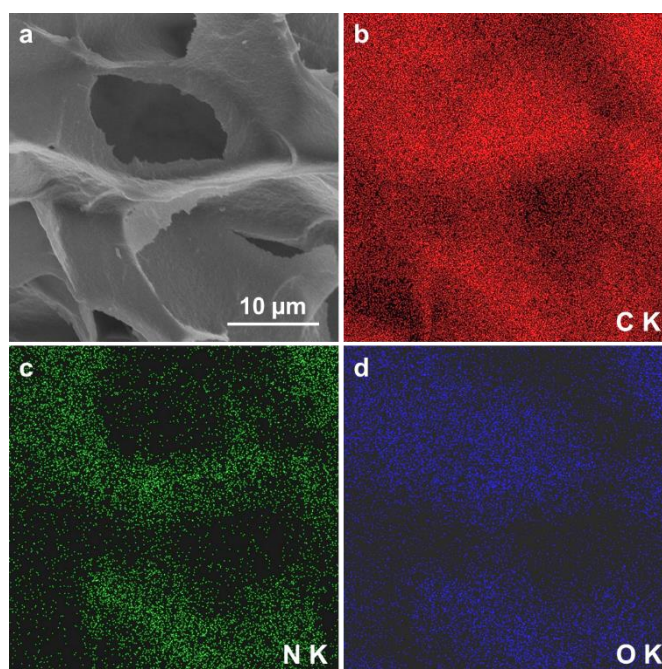
Figure 3.5. SEM elemental mappings of 3D-CON. (**a**) SEM image, (**b**) carbon, (**c**) nitrogen, (**d**) oxygen.

Table 3.1. Elemental composition of the 3D-CON from different characterization techniques

Technique	C	H	N	O	Total
Theoretical (wt%)	65.54	3.39	17.64	13.43	100
EA (wt%)[a]	66.27	2.95	16.24	13.90	99.36
XPS (at%)	84.11	NA[b]	10.35	5.54	100
SEM EDS (wt%)	70.66	NA[b]	19.81[c]	09.53[d]	100
SEM EDS (at%)	74.53	NA[b]	17.92	7.55	100

[a] Elemental analysis (EA) is most reliable element counts for bulk sample. [b] NA = Not available.
[c, d] The increased nitrogen content and decreased oxygen content in EDS is due to removal of adsorbed moisture and oxygen under high vacuum condition in SEM.

The porous properties and surface area of the 3D-CON was investigated by subjecting the framework to nitrogen adsorption-desorption experiments at 77 K. Before the sorption isotherm measurements, the sample was preheated at 150 °C for 12 h under dynamic vacuum.

As the sorption isotherm displayed in **Figure 3.4f**, the 3D-CON isotherm was fully reversible with an extremely steep nitrogen uptake in the low-pressure range (0-0.01). This result reflects the permanent microporous nature of the material according to the IUPAC classification[28]. The small hysteresis observed over the whole range of relative pressure suggests that the pore surface has relatively strong gas binding force.

The sharp uptake at very low p/p_o is due to enhanced adsorbent-adsorptive interactions in the ultramicropores, resulting in micropore filling at very low p/p_o. The Brunauer-Emmett-Teller (BET) model was used on the isotherms at a relative p/p_o range (0.005-0.05) to generate the BET surface area. The specific surface area found to be 2247 $m^2\ g^{-1}$ with a total pore volume of 1.06 $cm^3\ g^{-1}$ and an average pore diameter of 1.8 nm.
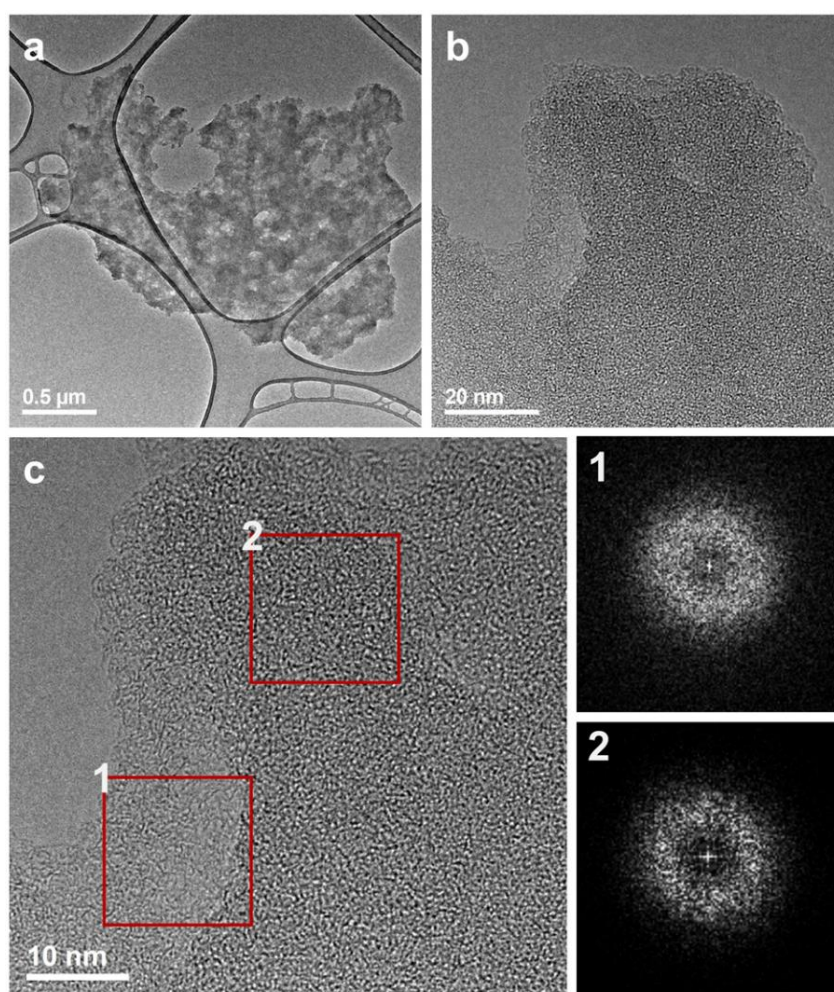
Figure 3.6. TEM images of 3D-CON. (a) Low magnification. (b) High resolution. (c) TEM image with corresponding fast Fourier transform (FFT) pattern from the highlighted region, showing low crystallinity as expected from the high molecular weight 3D organic network.
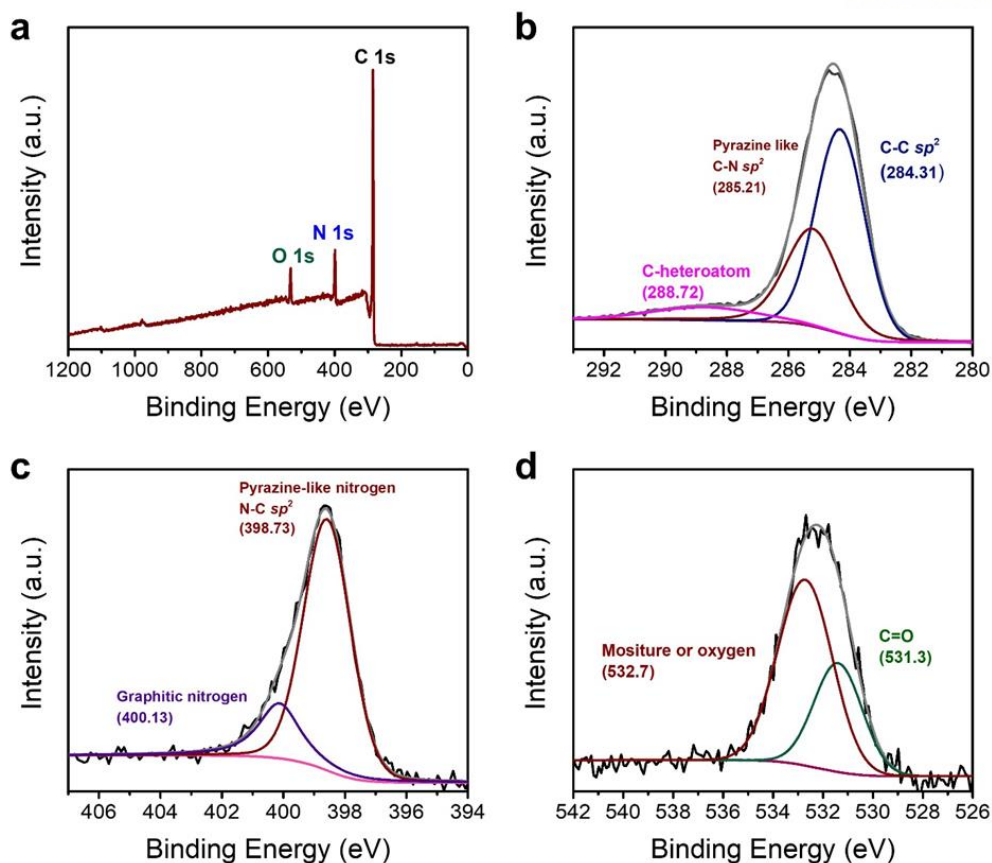
Figure 3.7. (a) Full XPS survey spectrum of 3D-CON. Deconvoluted XPS spectra: (b) C 1s; (c) N 1s; and (d) O 1s.

Pore size distribution obtained using the nonlocal density functional theory (NLDFT), which gives a more closely matching adsorption isotherm, was centered at around 0.55 nm (inset, **Figure 3.4f**). The BET measurements suggest that the 3D-CON possesses a uniform pore size (narrow pore size distribution), which is well related to the dimensions of the structure. Thus, it is clear that this material has an ordered structure.

Given the high specific surface area, microporous nature and narrow pore size distribution of 3D-CON material, the potential gas uptake capacities of small target molecules (H_2, CH_4 and CO_2) were investigated. It has been reported that nitrogen containing microporous frameworks generally perform well as a material for storing small gas molecules[26]. The H_2 uptake capacity of the 3D-CON was then explored.

The physiosorption storage of H_2 for energy applications is a promising approach to replace conventional fossil energy sources. The standard for on-board H_2 storage systems set by the US Department of Energy (DOE) by the year 2020 is 5.5 wt% and 40 g of H_2 L^{-1}. The H_2 adsorption-desorption isotherm of the 3D-CON was collected at 77 K with pressures up to 1.0 bar (**Figure 3.8a; Figure 3.9a**). The highest H_2 uptake was 2.64 wt% (296.30 cm^3 g^{-1}). This value was higher than most OPMs reported recently (**Figure 3.9f; Table 3.2**).

43
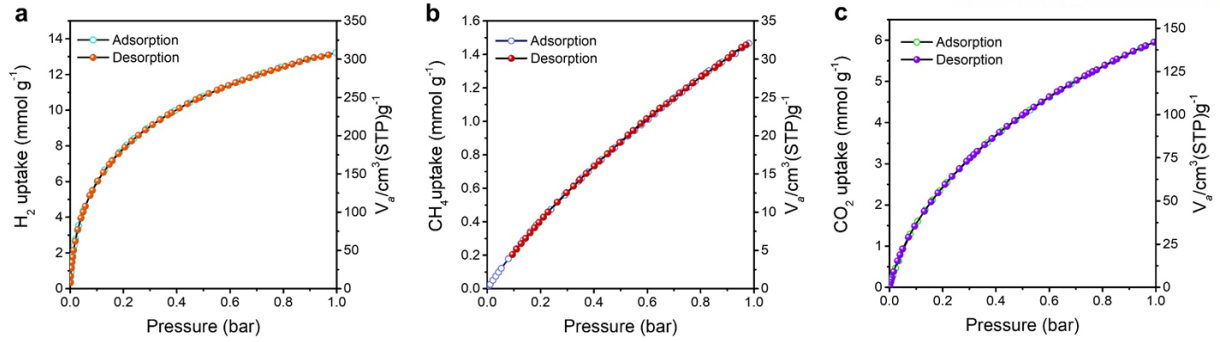
Figure 3.8. (**a**) H_2 adsorption isotherms of 3D-CON measured at 77 K. (**b**) CH_4 adsorption isotherm at 273 K. (**c**) CO_2 adsorption isotherms at 273 K in millimoles per gram and centimeter cube per gram scale.
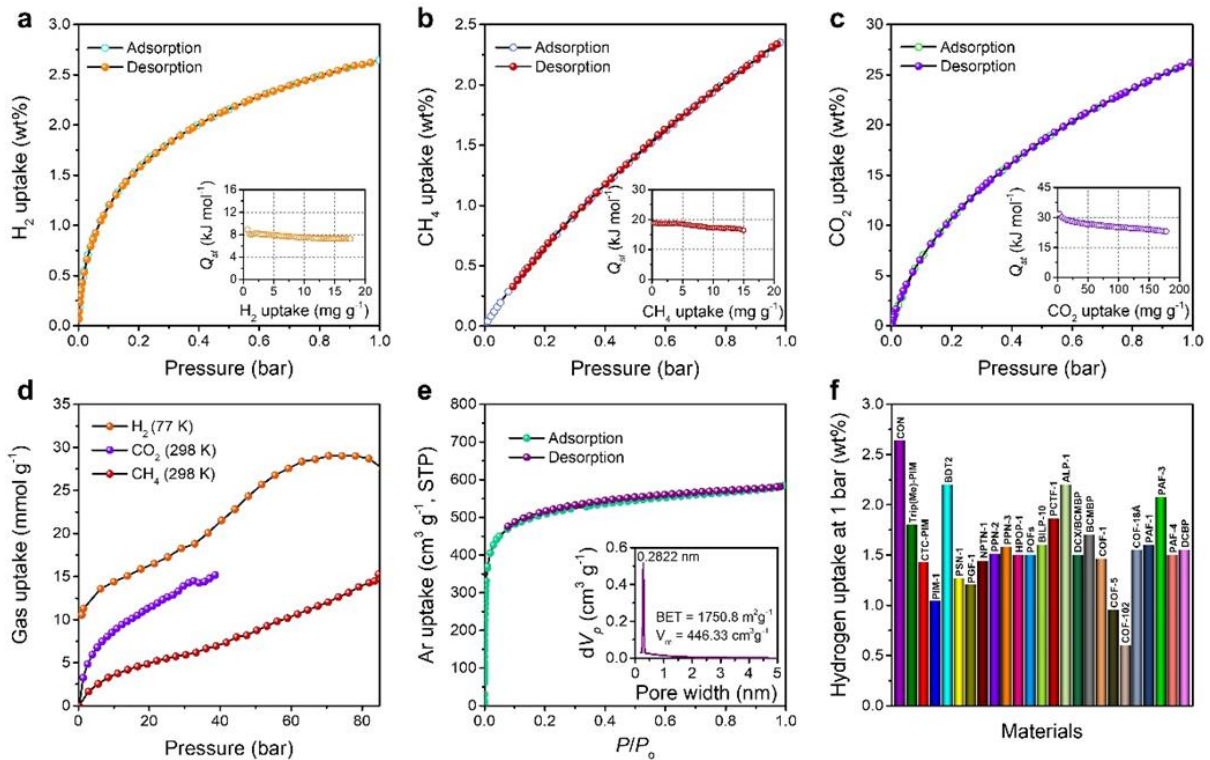
Figure 3.9. Gas storage properties of 3D-CON and literature comparison. (**a**) Hydrogen adsorption-desorption isotherm at 77 K. Inset: isosteric heat of adsorption (Q_{st}) as a function of gas loading calculated from low pressure isotherms at 77 and 87 K. (**b**) Methane adsorption-desorption isotherm at 273 K. Inset: Q_{st} as a function of gas storage obtained from low pressure isotherms at 77 and 87 K. (**c**) Carbon dioxide adsorption-desorption isotherms at 273 K. Inset: Q_{st} for the CO_2 as a function of gas uptake estimated from low pressure isotherms at 273 and 298 K. (**d**) High pressure gas (H_2, CH_4 and CO_2) uptakes. (**e**) Argon adsorption-desorption isotherm measured at 87 K. Inset: pore size distribution calculated from NLDFT. (**f**) Comparison of hydrogen uptakes for organic porous materials (OPMs) at 1 bar and 77 K.

This high H_2 uptake capacity can be attributed to the large surface area, which results from the combined effect of the 'internal free volume' of the triptycene-based 3D framework. The absence of hysteresis confirms the reversible physiosorption of H_2. In addition to exhibiting high surface area and stability, the 3D-CON met the DOE 2020 storage target at 77 K and 59 bar (**Figure 3.9d**).

As the basic constituent of natural gas, methane (CH_4) is an alternative fuel that is cleaner than petroleum oils due to its lower carbon emissions. CH_4 furnishes more energy because of its higher hydrogen to carbon ratio. Although CH_4 is more abundant and economical than gasoline, for use in automobiles an efficient and secured storage is required. The storage capacity should allow the vehicle to drive more than several hundred kilometers before refueling.

To further explore the different aspects that affect the CH_4 uptake in the 3D-CON, CH_4 adsorption assessments were performed at 273 K and 298 K in the low pressure range (**Figure 3.9b; Figure 3.8b**). As shown in **Figure 3.9b**, the CH_4 uptake at 1 bar is 2.4 wt% (33.5 $cm^3 g^{-1}$) at 273 K and 1.55 wt% (21.6 $cm^3 g^{-1}$) at 298 K (**Figure 3.10a**). This CH_4 uptake of 3D-CON is among the best reported values in the literature (**Table 3.2**).
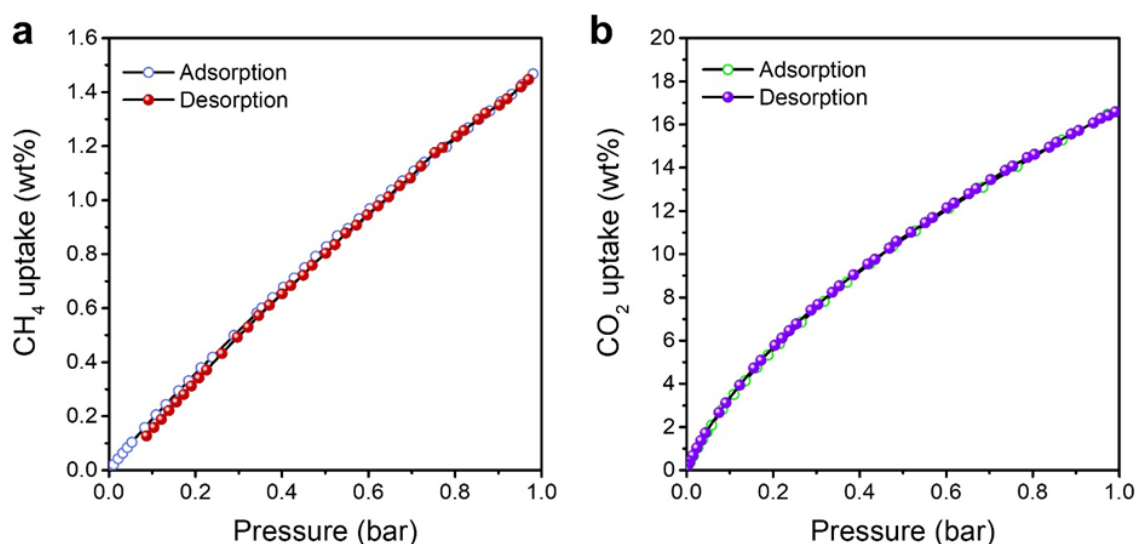
Figure 3.10. Adsorption isotherms of 3D-CON measured at 298 K: (**a**) CH_4, (**b**) CO_2.

The discharge of CO_2 due to the combustion of fossil fuels is now considered responsible for abnormal climate change, rising sea levels and an irreversible increase in the acidity of the oceans, resulting in adverse impacts on the sea ecology and environment. These issues have inspired the pursuit of state-of-the-art CO_2 capture technology and materials. The 3D-CON material, with its well-defined microporous structure, holds great potential for CO_2 capture.

Testing of the low pressure CO_2 uptake of the 3D-CON was performed, and it exhibited excellent CO_2 uptake at 1.0 bar, with a value of 26.7 wt% (137 $cm^3 g^{-1}$) at 273 K (**Figure 3.9c; Figure 3.8c**) and 17.15 wt% (88 $cm^3 g^{-1}$) at 298 K for CO_2 (**Figure 3.10b**). Adsorption and desorption isotherms showed no hysteresis, indicating the CO_2 uptake in 3D-CON was a reversible process; the interactions between

the 3D-CON and CO_2 are weak, and the framework can be regenerated without the application of heat[29].

Again, the adsorption capacity values for 3D-CON were found to be among the highest compared to most of the OPMs previously reported, and were even competitive with the best reported MOFs under the same conditions (**Table 3.2**).[30]

To further understand the interactions and adsorption properties of gases with the 3D-CON, the isosteric heat of adsorption (Q_{st}) for H_2, CH_4 and CO_2 was calculated from the gas adsorption isotherms at two different temperatures by fitting the values into the Clausius-Clapeyron equation[31]. The Q_{st} for hydrogen was examined by using the H_2 adsorption experiments at 77 and 87 K (**inset in Figure 3.9a)**.

One of the reasons for a lower uptake of H_2 is the weak interaction of H_2 with the adsorbent, due to a lack of binding sites. The 3D-CON displayed a Q_{st} value of 8.10 kJ mol^{-1} for H_2 adsorption at low H_2 uptake. Then, the Q_{st} value decreased slowly as the hydrogen uptake increased, and reached a value of 7.25 kJ mol^{-1} (**inset, Figure 3.9a**). This value is at the higher end compared to the reported literature[9]. At the same time, the higher Q_{st} value in the low pressure region is indicative of the higher affinity toward 3D-CON, due to the narrow ultramicroporous pore size distribution and robust fused-aromatic framework.

The Q_{st} values of the 3D-CON toward CH_4 and CO_2 were estimated from the adsorption data collected at 273 and 298 K (**inset, Figure 3.9b, c**). In the low CH_4 uptake zone, the Q_{st} value (18.72 kJ mol^{-1}) implied a highly reversible (absence of hysteresis) CH_4 attraction toward 3D-CON. A strong binding energy is preferred for storing a large amount of CH_4 at low pressure (**inset, Figure 3.9b**). The magnitude of Q_{st} was among the optimum heat of adsorption values reported for CH_4 adsorption, allowing both adsorption and desorption to occur at a fast rate, which is desirable for a fuel storage system.[32]

In the low CO_2 uptake zone, the 3D-CON exhibited a large Q_{st} value (31.87 kJ mol^{-1}) implying high CO_2 affinity toward the 3D-CON. The reason for the high Q_{st} value observed in the low-pressure region may be the strong interactions between CO_2 and the 3D-CON, as well as the narrow ultramicroporosity (**inset, Figure 3.9c**). Furthermore, the 3D-CON showed a gradual decrease in Q_{st} as a function of the quantity adsorbed. All of the Q_{st} values (H_2, CH_4, CO_2) were among the highest reported values for OPMs, and comparable to MOFs as well.[6, 33-34]

The low pressure gas sorption studies showed that the 3D-CON was far from saturation at 1 bar pressure. Thus, to evaluate the high pressure gas uptake capacity, high pressure gas sorption analyses for H_2, CH_4 and CO_2 were also performed (**Figure 3.9d**).

The H_2 uptake by the 3D-CON at 77 K revealed a gradual increase with pressure, and the H_2 storage at 59 bar reached 5.5 wt% (27.24 mmol g^{-1}) (**Figure 3.9d**) with saturation being reached at 70 bar (5.8 wt%). This exceeds the hydrogen uptake capacities of most OPMs having a similar surface area (**Table 3.2**).

The high pressure CH_4 uptake capacity of the 3D-CON at 298 K and 84 bar was found to be 24.5 wt% (15.27 mmol g^{-1}) (**Figure 3.9d**), which is fairly comparable to the best reported values (**Table 3.2**). The CO_2 storage was quite significant, reaching 70 wt% (15.90 mmol g^{-1}) at 298 K and 35 bar (**Figure 3.9d**). This value exceeds those of most reported OPMs (**Table 3.2**).

The microporosity of the 3D-CON was further confirmed by measuring the argon (Ar) gas adsorption isotherm. Moreover, measuring Ar adsorption at 87 K has some advantages for micropore analysis, because Ar does not have a quadrupole interaction. **Figure 3.9e** shows the Ar isotherm measured for 3D-CON, which exhibits a rapid Ar uptake at a very low relative pressure, indicating the typical behavior of permanent microporosity, followed by a very small gradual increase in Ar uptake (P/P_o = 0.05− 0.9).

The steep uptake at very low pressure is due to enhanced interactions in the narrow micropores, a typical type I isotherm, resulting in micropore filling at very low pressure. The pore size distributions were estimated by using NLDFT from the adsorption of the Ar isotherm (**inset, Figure 3.9e**), showing that the 3D-CON has only one major peak centered at 2.82 Å. This ultrahigh microporosity could be the reason of its exceptional H_2 uptake at low pressure, which should be associated with the robust fused-aromatic ring-based 3D-CON structure, suggesting a promising potential for clean energy and environmental applications.

3.4 Conclusions

In summary, we have presented the design and synthesis of shape persistent cage-like organic network structure using a rigid shape persistent building block derived from triptycene hexamine. This robust structure is thermally stable, ultramicroporous and display outstanding gas adsorption property. The cage-like organic network structure exhibits a BET surface area up to 2247 m^2 g^{-1} and high gas adsorption capacity. Owing to the small pore size distribution and aromatic fused ring system, the cage-like network structure exhibits excellent H_2 uptake of up to 2.64 wt % at 77K and 1.0 bar. Uptake for CO_2 is 26.7 wt % and CH_4 is 2.4 wt % at 273 K and 1.0 bar. This strategy of exploiting the effective condensation reaction to synthesize organic frameworks with high uptake capacity and high physiochemical stabilities hold huge promise for practical applications. CON demonstrates huge advance in the preparation of cage-like porous aromatic frameworks for high gas storage capacity.

3.5 Experimental Methods

3.5.1 Synthesis of triptycenehexaamine (THA) hexahydrochloride.

In a one-necked round bottom flask containing compound **3** (0.5 g, 0.38 mmol, Figure 3.2) in tetrahydrofuran (THF) solution (22 mL), aqueous HCl solution (2.0 M, 1.7 mL, 3.4 mmol) was slowly added. The mixture was stirred at room temperature for 0.5 h. The precipitate (triptycenehexaamine

hexahydrochloride, **4**) was collected by filtration, repeatedly washed with THF and hexane. An off-white powdery solid was dried under reduced pressure (0.01 mmHg) to yield quantitative (96%). The crude product was recrystallized from diluted aqueous HCl solution to give white needle-type crystals (**Figure 3.11**). ^{1}H NMR (400 MHz, D_2O) δ (ppm) 7.16 (s, triptycene aromatic C-H), 5.43 (s, 2H, triptycene aliphatic C-H) (**Figure 3.12a**). ^{13}C NMR (400 MHz, D_2O) δ (ppm) 141.61, 125.28, 117.08, 50.46 (**Figure 3.12b**). DIP-MS m/z for $C_{20}N_{20}N_6$: $[M^+]$ found 344.136 (**Figure 3.12c**). EA calculated for $C_{20}N_{26}N_6Cl_6$: (wt%) C, 42.56; H, 4.65; Cl, 37.77; N, 14.92. Found: C, 42.50; H, 4.66; N, 14.90.
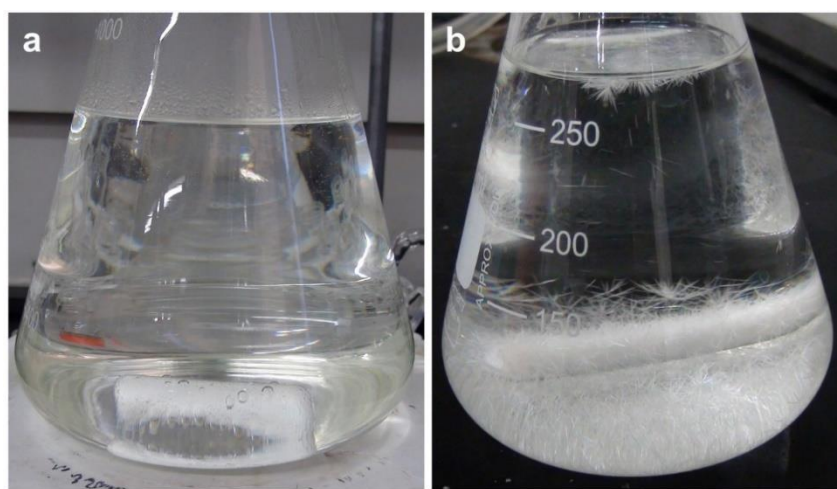
Figure 3.11. Recrystallization of triptycenehexaamine (THA, 4) hexahydrochloride in dilute aqueous HCl solution. (a) Before crystallization. (b) After crystallization overnight standing at room temperature. White needle-type crystals were formed.
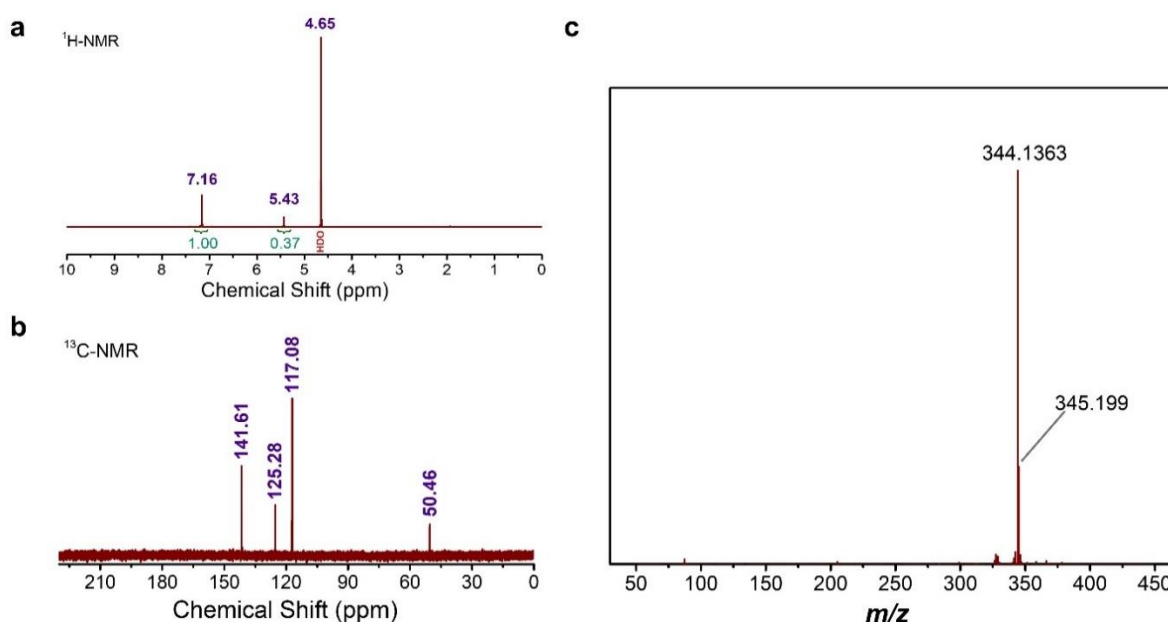
Figure 3.12. Characterizations of the triptycenehexaamine (THA, **4**) hexahydrochloride. (a) ^{1}H-NMR spectrum (D_2O). (b) ^{13}C-NMR spectrum (D_2O). (c) DIP-MS spectrum.

3.5.2 Synthesis of robust three-dimensional (3D) cage-like organic network (CON).

Into 120 mL Pyrex ampoule, hexaketocyclohexane (HKH) octahydrate (0.277 g, 0.887 mmol) and triptycene hexamine (THA) hexahydrochloride (500 mg, 0.887 mmol) were charged. Ethylene glycol (25 mL) and acetic acid (3 M, 25 mL) were added and the ampule was violently agitated for complete mixing at room temperature. Then, the mixture was degassed by charging/discharging nitrogen using three freeze-thaw pump cycles. The ampoule was then sealed under reduced pressure in the liquid nitrogen. The ampule was placed and slowly heated to 130 °C for 80 h. The brown precipitates were collected by filtration and Soxhlet extracted with water and methanol for 3 days each. The sample was dried under reduced pressure (0.01 mmHg) overnight to afford bright brown powder in quantitative yield (99.3%).

3.5.3 Low pressure gas adsorption analysis (up to 1 bar).

Low pressure gas adsorption measurements were performed on samples, which were heated previously under dynamic vacuum at 150 °C for 12 h to remove residual solvents and other adsorbates. Basic volumetric N_2 sorption studies were carried out at 77 K using the Brunauer-Emmett-Teller (BET) method on BELSORP-max (BEL Japan, Inc., Japan). Liquid nitrogen, liquid argon and ice-water baths were used for adsorption measurement at 77, 87 and 273 K, respectively. Ultra-high purity (UHP) grade N_2, Ar, H_2, CO_2 and CH_4 gases (99.999% purity) were used during the adsorption measurements. A sample and nitrogen (99.999 %) gas supply was used in the nitrogen sorption analysis at 77 K (liquid nitrogen) throughout the whole measurement. Oil-free environments (vacuum pump and pressure regulators) were used for all measurements to avoid contamination of the samples during the degassing process and isotherm calculation. In order to test sample stability, the hydrogen isotherm measurements were repeated four times in succession over a period of eight months, during which other gas isotherms such as CH_4, CO_2 were also carried out on the same sample. There was no obvious change between the cycles or fluctuations were recorded due to change in the temperature and pressure.

3.5.4 High pressure gas sorption measurements.

High pressure adsorption of H_2, CO_2, CH_4 were recorded using Gas Adsorption-Desorption Measurement System (PCTPro-E&E, SETARAM France) at 77 K (liquid nitrogen bath) or 298 K (room temperature). The samples were degassed at 150 °C for 15 h under dynamic vacuum prior to measurements until a constant mass was attained. The sample was charged into the sample holder under inert atmosphere.

3.6 Materials.

All the solvents, chemicals and reagents were purchased from Aldrich Chemical Inc., unless

otherwise stated. Solvents were degassed with nitrogen purging before use. All reactions were performed under nitrogen atmosphere using oven dried glassware. Triptycene hexamine (THA) hexahydrochloride was synthesized according to a procedure described in the literature.[24]

3.7 Instrumentations.

Scanning electron microscope (SEM) images were taken with a Field Emission Scanning Electron Microscope Nanonova 230 FEI, USA. X-ray photoelectron spectroscopy (XPS) was performed on an X-ray Photoelectron Spectrometer Thermo Fisher K-alpha (UK). X-ray diffraction (XRD) studies were taken on a High-Power X-Ray Diffractometer D/MAZX 2500V/PC (Cu–Kα radiation, 35 kV, 20 mA, λ = 1.5418 Å) Rigaku, Japan. Magic-angle spinning (MAS) nuclear magnetic resonance (NMR) spectra were measured at 298 K on an Agilent VNMRS 600 spectrometer. The spectra were recorded under conditions of cross polarization ($^{13}C \leftarrow {}^{1}H$), magic angle sample spinning high power ^{1}H decoupling. The thermogravimetric analysis (TGA) was carried using a SDT Model Q600 thermal analyzer at a heating rate of 10 °C min^{-1} in nitrogen and dry air atmosphere. Elemental analysis (EA) was conducted with a Thermo Scientific Flash 2000 Analyzer. High resolution transmission electron microscopy (HR-TEM) was performed by using a JEM-2100F microscope (JEOL, Japan) under an operating voltage of 200 keV. The samples for TEM were prepared by drop casting an ethanol dispersion on Quantifoil holey carbon TEM grid and dried.

Table 3.2. Hydrogen, CO_2 and CH_4 uptake of various literature reported organic porous materials (OPMs)

Materials	BET area m^2 g^{-1}	H$_2$ uptake 77 K (wt%)	CO$_2$ uptake (273 K) mg g^{-1}	CH$_4$ uptake (273 K) mg g^{-1}	References
3D-CON	2247	2.64 (1.0 bar) 5.8 (70 bar)	267 (1.0 bar) 750 (35 bar, 298 K)	24 (1.0 bar) 237 (85 bar, 298 K)	*This work*
Trip(Me)-PIM	1760	1.80 (1.0 bar), 3.4 (18 bar)	---	---	Macromolecules, 2010, 43, 5287
CTC-PIM	770	1.43 (1.0 bar) 1.7 (10 bar)	---	---	Angew. Chem. Int. Ed. 2006, 45, 1804
PIM-1	760	1.04 (1.0 bar) 1.44 (10 bar)	---	---	Angew. Chem. Int. Ed. 2006, 45, 1804
BDT2	571	1.5 (1.0 bar)	105 (1.0 bar)	8 (1.0 bar)	ACS Appl. Mater. Interfaces 2016, 8, 27669
BDT3	1010	2.2 (1.0 bar)	165 (1.0 bar)	29 (1.0 bar)	ACS Appl. Mater. Interfaces 2016, 8, 27669
PSN-1	1045	1.26 (1.0 bar)	150 (1.0 bar)	---	Chem. Commun. 2014, 50, 1897
PGF-1	825	1.20 (1.0 bar)	72 (1.0 bar)	---	Chem. Commun. 2014, 50, 2015

NPTN-1	1558	1.44 (1.0 bar)	140 (1.0 bar)	---	Macromolecules 2014, 47, 2875
Th-1	726	1.11 (1.0 bar)	127 (1.0 bar)	---	Adv. Mater. 2012, 24, 5703
Cz-POF-1	2065	2.2 (1.0 bar)	202 (1.0 bar)	22 (1.0 bar)	Chem. Mater. 2014, 26, 4023
FCTF-1-600	1535	---	243 (1.0 bar)	---	Energy Environ. Sci., 2013, 6, 3684
Network-1	1980	1.76 (1.0 bar)	160 (1.0 bar)	---	J. Mater. Chem. A, 2014, 2, 8054
Network-A	4077	---	117 (1.0 bar)	---	Energy Environ. Sci., 2011, 4, 4239
Network-C	1237	---	170 (1.0 bar)	---	Energy Environ. Sci., 2011, 4, 4239
Network-E	1470	---	130 (1.0 bar)	---	Energy Environ. Sci., 2011, 4, 4239
TPI-1@IC	1053	---	141 (1.0 bar)	---	J. Mater. Chem. A, 2015, 3, 878
PPN-1	827	1.37 (1.0 bar), 3.30 (45 bar)	---	---	Chem. Mater. 2010, 22, 5964
PPN-2	2790	1.51 (1.0 bar), 3.76 (40 bar)	---	---	Chem. Mater. 2010, 22, 5964
PPN-3	5323	1.58 (1.0 bar), 4.28 (42 bar)	---	---	Chem. Mater. 2010, 22, 5964
POP-1	1031	2.78 (60 bar)	---	---	Chem. Commun. 2010, 46, 4547
POP-2	1013	2.71 (60 bar)	---	---	Chem. Commun. 2010, 46, 4547
POP-3	1246	3.07 (60 bar)	---	---	Chem. Commun. 2010, 46, 4547
POP-4	1033	2.35 (60 bar)	---	---	Chem. Commun. 2010, 46, 4547
HPOP-1	1148	1.50 (1.13 bar)	---	---	Macromolecules, 2011, 44, 5573
HPOP-2	742	1.08 (1.13 bar)	---	---	Macromolecules, 2011, 44, 5573
POFs	1063	1.5 (1.0 bar), 4.3 (70 bar)	---	---	Chem. Mater., 2010, 22, 4974
BILP-3	1306	2.1 (1.0 bar)	225 (1.0 bar)	24 (1.0 bar)	Chem. Commun. 2012, 48, 1141
BILP-10	787	1.6 (1.0 bar)	177 (1 bar)	16.7 (1.0 bar)	J. Mater. Chem., 2012, 22, 25409
TPOP-5	810	1.07 (1.13 bar)	---	---	J. Mater. Chem., 2011, 21, 13554
PCTF-1	2235	1.86 (1.0 bar)	142 (1.0 bar)	16.9 (1.0 bar)	Chem. Commun. 2013, 49, 3961
APOP-3	1402	1.80 (1.0 bar)	199 (1.0 bar)	21 (1.0 bar)	Polym. Chem., 2013, 4, 4690
PCTF-2	784	0.9 (1.0 bar)	80.7 (1.0 bar)	10.8 (1.0 bar)	Chem. Commun. 2013, 49, 3961
ALP-1	1235	2.2 (1.0 bar)	236 (1.0 bar)	26 (1.0 bar)	Chem. Mater. 2014, 26, 1385

P-PCz	1647	---	245 (1.0 bar)	---	Chem. Commun. 2016, **52**, 4454
TSP-2	913	---	180 (1.0 bar)	---	Chem. Commun. 2014, 50, 7933
TAPOP-1	930	---	154 (1.0 bar)	---	RSC Adv., 2015, 5, 90135
PPN-6-CH$_2$DETA	555	---	158 (1.0 bar)	---	Angew. Chem. Int. Ed. 2012, 51, 7480
Azo-COP-2	729	---	112 (1.0 bar)	---	Nat. Commun. 2013, 4, 1357
STPI-2	541	---	146 (1.0 bar)	---	Polymer 2014, 55, 3642
PECONF-3	851	---	153 (1.0 bar)	16 (1.0 bar)	Nat. Commun. 2011, 2, 401
Polystyrene	1930	1.4 (1.0 bar), 5.2 (80 bar)	---	---	Chem. Mater. 2006, 18, 4430
DCX/BCMBP	1904	1.50 (1.0 bar), 3.7 (15 bar),	---	70 (36 bar)	Adv. Mater. 2008, 20, 1916
BCMBP	1366	1.70 (1.0 bar), 2.8 (15 bar),	---	88 (36 bar)	Adv. Mater. 2008, 20, 1916
Polyaniline	632	0.96 (1.0 bar)	---	---	J. Mater. Chem., 2007, 17, 4989
Polypyrrole	732	1.60 (1.0 bar)	---	---	Chem. Commun. 2009, 1526
COF-1	750	1.46 (35 bar)	230 (35 bar)	40 (44 bar)	J. Am. Chem. Soc. 2009, 131, 8875
COF-5	1990	0.95 (1.0 bar), 3.54 (35 bar)	870 (55 bar)	89 (35 bar)	J. Am. Chem. Soc. 2009, 131, 8875
COF-103	4630	0.6 (1.0 bar) 3.5 (35 bar)	1190 (55 bar)	175 (35 bar)	J. Am. Chem. Soc. 2009, 131, 8875
COF-102	3620	0.6 (1.0 bar), 3.6 (35 bar)	1200 (55 bar)	187 (35 bar)	J. Am. Chem. Soc. 2009, 131, 8875
COF-18Å	1263	1.55 (1.0 bar)	---	---	Adv. Mater. 2008, 20, 2741
PAF-1	5600	1.6 (1.0 bar)	91 (1.0 bar)	13 (1.0 bar)	Energy Environ. Sci., 2011, 4, 3991
PAF-3	2932	2.07 (1.0 bar)	153 (1.0 bar)	19 (1.0 bar)	Energy Environ. Sci., 2011, 4, 3991
PAF-4	2246	1.50 (1.0 bar)	107 (1.0 bar)	13 (1.0 bar)	Energy Environ. Sci., 2011, 4, 3991
DCBP	2475	1.55 (1.0 bar)			Angew. Chem. Int. Ed. 2008, 47, 3450

3.8 References

(1) Ferey, G.; Serre, C.; Devic, T.; Maurin, G.; Jobic, H.; Llewellyn, P. L.; De Weireld, G.; Vimont, A.; Daturi, M.; Chang, J.-S., *Chem. Soc. Rev.* **2011,** *40*, 550-562.

(2) Germain, J.; Fréchet, J. M. J.; Svec, F., *Small* **2009,** *5*, 1098-1111.

(3) Owusu, P. A.; Asumadu-Sarkodie, S.; Dubey, S., *Cogent Eng.* **2016,** *3*, 1167990.

(4) McGlade, C. E., *Energy* **2012,** *47*, 262-270.

(5) D'Alessandro, D. M.; Smit, B.; Long, J. R., *Angew. Chem. Int. Ed.* **2010,** *49*, 6058-6082.

(6) Lu, W.; Yuan, D.; Zhao, D.; Schilling, C. I.; Plietzsch, O.; Muller, T.; Bräse, S.; Guenther, J.; Blümel, J.; Krishna, R.; Li, Z.; Zhou, H.-C., *Chem. Mater.* **2010,** *22*, 5964-5972.

(7) Kumar, K. V.; Preuss, K.; Titirici, M.-M.; Rodríguez-Reinoso, F., *Chem. Rev.* **2017,** *117*, 1796-1825.

(8) Dell, R.; Rand, D., Clean Energy **2004**.

(9) Dawson, R.; Cooper, A. I.; Adams, D. J., *Prog. Polym. Sci.* **2012,** *37*, 530-563.

(10) Ben, T.; Pei, C.; Zhang, D.; Xu, J.; Deng, F.; Jing, X.; Qiu, S., *Energy Environ. Sci.* **2011,** *4*, 3991-3999.

(11) Liu, Q.; Tang, Z.; Wu, M.; Zhou, Z., *Polym. Int.* **2014,** *63*, 381-392.

(12) Li, B.; Wen, H.-M.; Cui, Y.; Zhou, W.; Qian, G.; Chen, B., *Adv. Mater.* **2016,** *28*, 8819-8860.

(13) Furukawa, H.; Cordova, K. E.; O'Keeffe, M.; Yaghi, O. M., *Science* **2013,** *341*, 1230444.

(14) Cooper, A. I.; Rosseinsky, M. J., *Nat. Chem.* **2009,** *1*, 26-27.

(15) Czaja, A. U.; Trukhan, N.; Muller, U., *Chem. Soc. Rev.* **2009,** *38*, 1284-1293.

(16) Davis, M. E., *Nature* **2002,** *417*, 813-821.

(17) Ben, T.; Qiu, S., *CrystEngComm* **2013,** *15*, 17-26.

(18) Chen, Q.; Luo, M.; Hammershøj, P.; Zhou, D.; Han, Y.; Laursen, B. W.; Yan, C.-G.; Han, B.-H., *J. Am. Chem. Soc.* **2012,** *134*, 6084-6087.

(19) Yuan, D.; Lu, W.; Zhao, D.; Zhou, H.-C., *Adv. Mater.* **2011,** *23*, 3723-3725.

(20) Rabbani, M. G.; El-Kaderi, H. M., *Chem. Mater.* **2012,** *24*, 1511-1517.

(21) Lu, W.; Yuan, D.; Sculley, J.; Zhao, D.; Krishna, R.; Zhou, H.-C., *J. Am. Chem. Soc.* **2011,** *133*, 18126-18129.

(22) Zhang, Y.; Riduan, S. N., *Chem. Soc. Rev.* **2012,** *41*, 2083-2094.

(23) Mahmood, J.; Lee, E. K.; Jung, M.; Shin, D.; Jeon, I.-Y.; Jung, S.-M.; Choi, H.-J.; Seo, J.-M.; Bae, S.-Y.; Sohn, S.-D.; Park, N.; Oh, J. H.; Shin, H.-J.; Baek, J.-B., *Nat. Commun.* **2015,** *6,* 6486.

(24) Rabbani, M. G.; Reich, T. E.; Kassab, R. M.; Jackson, K. T.; El-Kaderi, H. M., *Chem. Commun.* **2012,** *48*, 1141-1143.

(25)   Zhang, C.; Zhu, P.-C.; Tan, L.; Liu, J.-M.; Tan, B.; Yang, X.-L.; Xu, H.-B., *Macromolecules* **2015,** *48*, 8509-8514.

(26)   Mondal, S.; Das, N., *J. Mater. Chem. A* **2015,** *3*, 23577-23586.

(27)   Chong, J. H.; MacLachlan, M. J., *Chem. Soc. Rev.* **2009,** *38*, 3301-3315.

(28)   Rouquerol, J.; Avnir, D.; Fairbridge, C. W.; Everett, D. H.; Haynes, J. M.; Pernicone, N.; Ramsay, J. D. F.; Sing, K. S. W.; Unger, K. K., *Pure Appl. Chem.* **1994**, 66, 1739-1758.

(29)   Arab, P.; Rabbani, M. G.; Sekizkardes, A. K.; İslamoğlu, T.; El-Kaderi, H. M., *Chem. Mater.* **2014,** *26*, 1385-1392.

(30)   Sumida, K.; Rogow, D. L.; Mason, J. A.; McDonald, T. M.; Bloch, E. D.; Herm, Z. R.; Bae, T.-H.; Long, J. R., *Chem. Rev.* **2012,** *112*, 724-781.

(31)   Xie, L.-H.; Suh, M. P., *Chem. Eur. J.* **2013,** *19*, 11590-11597.

(32)   Bhatia, S. K.; Myers, A. L., *Langmuir* **2006,** *22*, 1688-1700.

(33)   Wang, Z.; Zhang, B.; Yu, H.; Sun, L.; Jiao, C.; Liu, W., *Chem. Commun.* **2010,** *46*, 7730-7732.

(34)   Gallo, M.; Glossman-Mitnik, D., *J. Phys. Chem. C* **2009,** *113*, 6634-6642.

IV. Two-dimensional standing-like fully-fused aromatic network for efficient gas separation N_2/CH_4

4.1 Abstract

Fully-fused aromatic networks (FANs) have been widely applied as the energy materials. Gas storage and separation are important technologies in the energy market such as shale gas, and material development is the key. The organic network structure depends on the structural dimensions. The 2-dimensional structures have been applied to separation with high selectivity, and 3-dimensional structures have been applied to gas storage with high gas adsorption amount. Gas separation through pressure swing adsorption (PSA) is considered both in terms of selectivity and capacity, but there are many difficulties in material development due to the trade-off relationship between the two. In this study, we introduce a new standing-like 2-dimensional structure, which and provide a strategy to complement the selectivity and storage capacity. The results provide insights into the design of polymer structures for gas separation.

4.2 Introduction

Rationally designed porous organic frameworks (POFs) are classified into various categories like ordered covalent organic frameworks (COFs), porous organic networks (PONs), hyper-cross-linked polymers (HCPs), conjugated microporous polymers (CMPs), fused aromatic networks (FANs), etc.[1,2] The dimension of the structure, chemical properties of the pore and their size can be controlled by choosing suitable monomer symmetry along with its functional groups to envision applications in the field of energy storage, catalysis, drug delivery, gas absorption, separation membrane and other significant applications.[1,3-7]

FANs structures doped with heterogeneous elements (especially nitrogen) such as C_2N-h2D,[8] C_3N,[9] Aza-CMP,[10] aza-COF-1,[11] and CS-COF,[12] etc., have been reported to overcome the limitation of the two-dimensional (2D) inorganic/metallic structure (eg. graphene, MoS_2, etc.), and fully-fused structures have exhibited excellent electronic properties with semiconductor characteristics as an energy material. In addition, by stably holding the metal with the electron delocalized of the bonding between nitrogen and carbon, they showed a high catalytic activity and strong durability.[13-15]

In the gas separation field, metal organic frameworks (MOFs) have been studied a lot to overcome the commercial zeolite properties that are currently being used in connection with pressure swing adsorption (PSA), which is a technique called molecular sieve that separates the desired gas from the mixture by using difference in adsorption of the individual gas.[16,17] Although a wide range of POFs structures be can design with mass production,[18] but their application to PSA process is hampered by

the low thermal stability and the flexibility which creates variation in pore size due to rotation or folding of structure.

Among the possible candidate of POFs structures for the separation, fused aromatic networks (FANs) can be perceived as an alternative. The FANs, which have a rigid fused ring do not rotate and renders higher thermal stability to the framework. However, studies on gas storage and separation related to fully-fused 2D structure are not actively studied. This is because the entire structure is aromatic, and the interlayer interaction force becomes large, so that it has a lower surface area than the three-dimensional (3D) structure or the general POFs.

For the successful gas separation application, not only gas selectivity which related to purity but also gas adsorption property is significant factor to reduce cycles of PSA process. Generally, 2D structure is advantageous for separation by showing high selectivity, but 3D structure is known to be for gas storage rather than separation because variety gas molecules easily access to open pores. Due to the trade-off relationship between selectivity and capacity, it may be difficult to design precise structures. Moreover, the conventional 2D structures have the disadvantages of blocking the pore channels depending on the stacking pattern such as AA, AB, or ABC.[19] Although there are studies to prevent interlayer interaction by attaching bulky and rigid substituents to prevent layers stacking, this method has the disadvantage of losing original structural characteristics.[20]

To cope with design and performance issues, here, we report new type of standing-like 2D fully fused aromatic network (2D-Standing) structure to highlight new strategies in design of gas separation material through reducing layered π-π interactions. To compare the structural properties of standing-like motif, we prepared 2D (2D-Flat type) and 3D (3D-CON) structures as the conventional FANs.[21]

The separation between CH_4 and N_2 gases is very challenging technology due to the kinetic diameter similarity (CH_4: 3.80 Å and N_2: 3.64 Å).[22,23] Since the PSA process is effective for separating methane for natural gas upgrading, we have investigated the adsorption and selectivity with the structures mentioned above.

This study will provide insight into the design of FANs structures, how these differences affect gas separation and adsorption properties. Furthermore, how standing-like 2D structure differs from the layered 2D structure. To the best of our knowledge, this is the first case of design and performance study of fully fused aromatic 2D-Standing structure and its comparison with the other dimensional structures (2D and 3D) of the same family.

4.3 Results and discussion

All the fully-fused aromatic network structures were synthesized by condensation aromatization between di-amine and di-ketone moieties in acidic condition (***see Methods***).   Phenazine rings formed through aromatization are partially polarized due to the pyridinic N. In addition, all structures have

56

fused rings, so it has the advantage of being strong and thermodynamic stability because it is irreversible reaction. For 2D-Flat, like **Figure 4.1**, the structure will grow in two-dimensional direction, but in case of 2D-Standing, we expect the units of structure to be grown 'standing-like' vertically along the growth 2D plane.
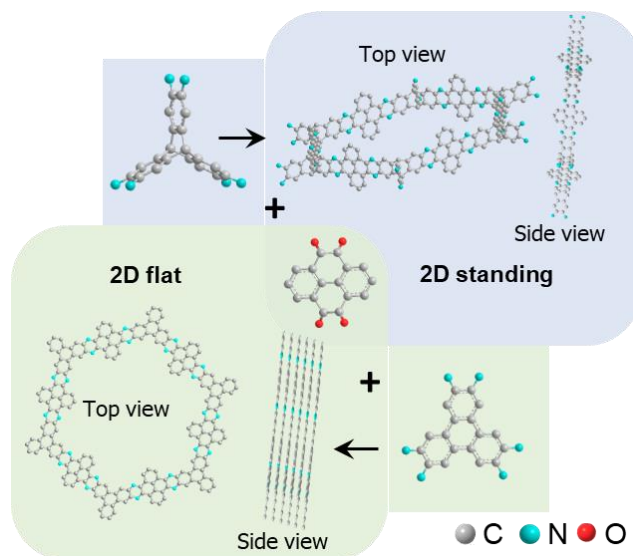
Figure 4.1. Illustrate of 2D-Flat and 2D-Standing network structure. Each element is drawn as different color (gray: carbon, cyan: nitrogen, red: oxygen).
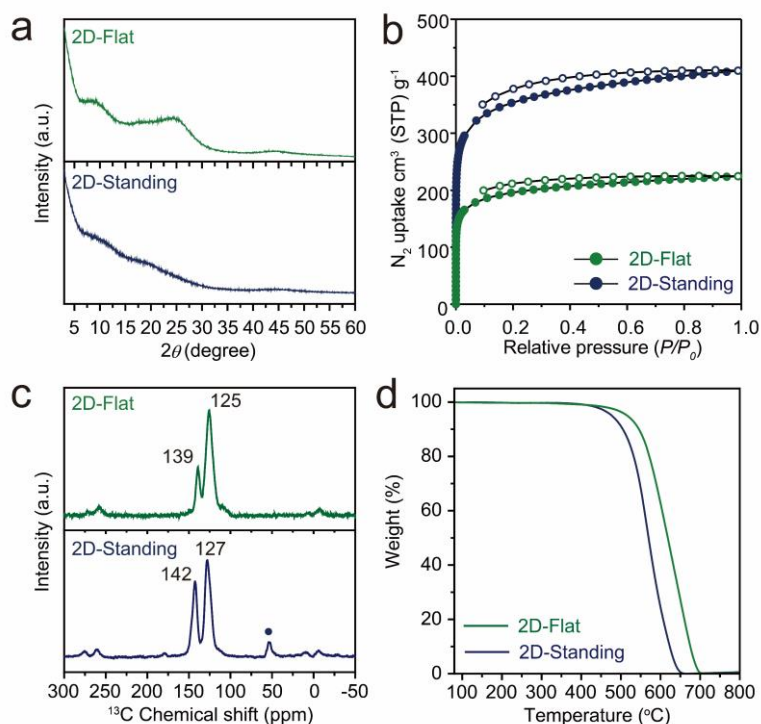
Figure 4.2. Structural characterization of the structures. (a) XRD patterns of the frameworks (b) BET isotherms measured at 77 K. Filled: adsorption; blank: desorption. (c) CP/MAS ^{13}C NMR spectra of 2D-Standing (top) and 2D-Flat (bottom) structure. (d) TGA of each organic network structure in the air atmosphere (ramping rate: 10 ˚C/min). Dark blue: 2D-Standing, dark green: 2D-Flat.

Table 4.1. Atomic compositions of surface of 2D-Standing and 2D-Flat structures as determined by the survey of XPS regarding carbon (C), nitrogen (N), and oxygen (O)

Results		Element (at. %)		
		C	N	O
2D-Standing	Theoretical	84.63	11.52	3.84
	Experimental	81.79	9.62	9.53
2D-Flat	Theoretical	84.00	12.03	3.97
	Experimental	83.90	7.71	8.39

To analyze structure, we performed an X-ray photoelectron spectroscopy (XPS), elemental analysis (EA), X-ray diffraction (XRD), Brunauer-Emmett-Teller (BET) analysis, Cross-polarization/magic angle spinning ^{13}C nuclear magnetic resonance (CP/MAS ^{13}C NMR), scanning electron microscopy (SEM), and high-resolution transmission electron microscopy (HR-TEM) for each structure.

The atomic compositions of surface and presence of carbon (C), nitrogen (N), and oxygen (O) respectively in the deconvoluted XPS peaks were observed. The pyridinic N (398.28 eV), C-N (294.96 eV), and C=O (531.42 eV, could be on the edge) peaks were identified (**Figure 4.3**, **Table 4.1**). The elemental analysis was well matched with the expected values and the experimental results, and other elements were not observed (**Table 4.2**). Regarding XRD patterns, interestingly in a 2D-Flat structure, the peak at 26° corresponds to the interlayer interaction is missing in case of 2D-Standing structure, which indicates the difference between the two structures (**Figure 4.2a**). This means that 2D-Standing structure does not have a π-π interaction between the layers and indirectly shows the availability of open pores or surface area loss by the stacking pattern.
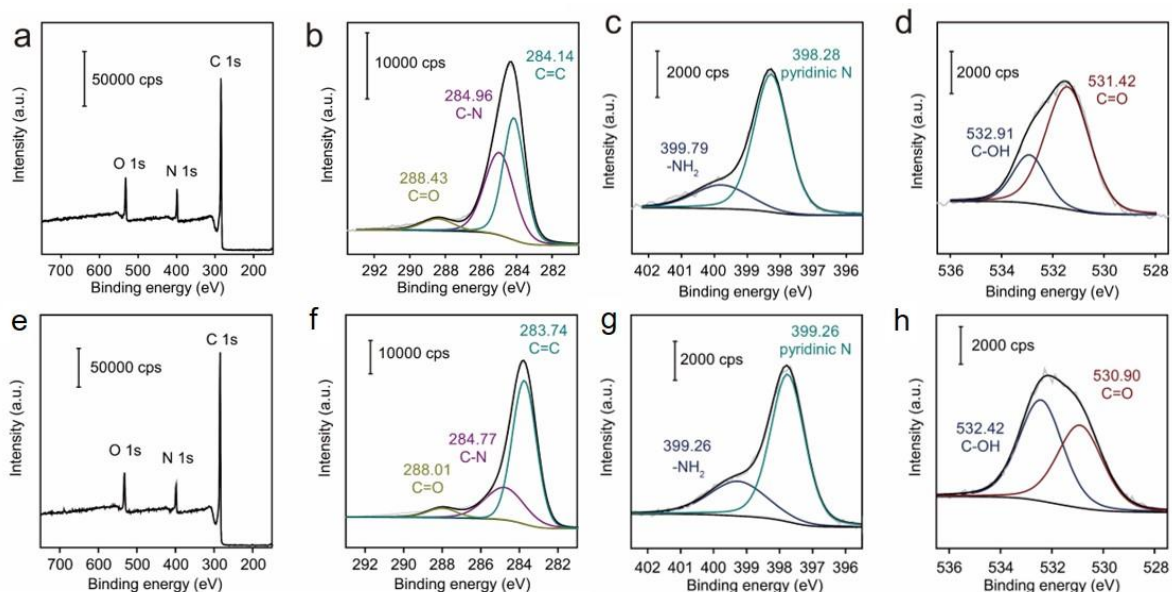
Figure 4.3. High-resolution XPS spectra of 2D-Standing (a-d, top) and 2D-Flat (e-h, bottom). (a, e) Survey spectrum. (b, f) C 1s spectra. (c, g) N 1s spectra. (d, h) O 1s spectra.
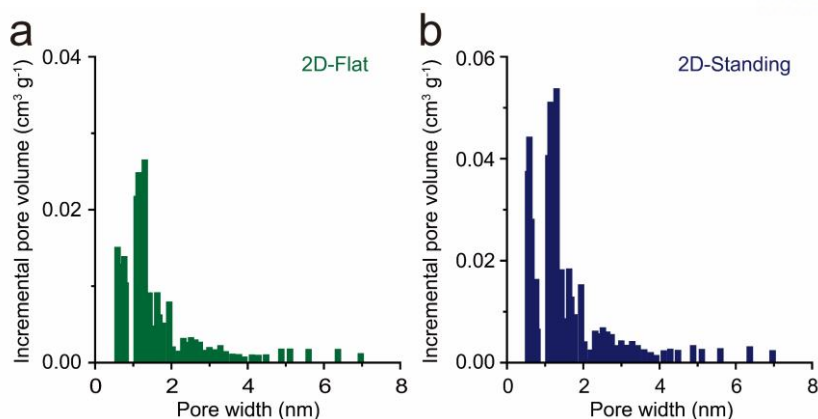
Figure 4.4. NLDFT pore size distribution (PSD) results of (a) 2D-Flat and (b) 2D-Standing.

Table 4.2. Elemental analysis data of 2D-Standing and 2D-Flat structures

Results		Element (wt%)				
		C	N	H	O	Total
2D-Standing	Theoretical	79.39	12.62	3.18	4.81	100
	Experimental	78.05	10.56	2.93	7.53	99.07
2D-Flat	Theoretical	79.99	13.33	2.88	3.81	100
	Experimental	76.81	10.96	2.61	6.06	96.44

The BET surface area calculated by isotherm N_2 sorption curves at 77 K provides information on regarding the surface area of the materials depending on the geometry (**Figure 4.2b, Table 4.3**). As expected, 2D-Standing indicates the higher surface area (1336.22 m^2 g^{-1}) and adsorption amount compared to 2D-Flat structure (743.45 m^2 g^{-1}). It can be described the creation of loose packing with rigid framework makes yield higher permeability and free volume.[24] The pore size distribution (PSD) using non-local density functional theory (NLDFT) showed the major pore widths of 0.59 and 1.3 nm in both structures **(Figure 4.4)**. This means that the structural difference between 2D-Flat and 2D-Standing is the difference between lying and standing but does not affect the pore size. From the BET analysis, a 2D-standing structure can be indirectly understood that by eliminating π-π stacking, the gas molecules feel freedom for adsorption like 3D structure. This suggests that with same functional groups and even in the same chemical environment, the orientation of the structure (standing-like) is advantageous for high gas storage and large surface area.

CP/MAS ^{13}C NMR spectroscopy critically confirmed the difference between 2D-Standing and 2D-Flat structure (**Figure 4.2c**). The resonance peak at δ = 54 (dark blue dot in **Figure 4.2c**) can be assigned to the bridging carbon of the triptycene unit (methylidyne bridge) in 2D-Standing network.[21,25] In case of 2D-flat structure, the peak at δ = 125 shows a strong carbon peak related to aromatic pyrene and triphenylene moieties, and δ = 139 is associated with phenazine carbon (C=N) peak formed by the

reaction of di-amine and di-ketone moieties. The 2D-Standing structure also reveals the respective carbon peaks at $\delta = 127$ and 142 associated to the aromatic fragment and phenazine carbon respectively, similar to 2D-Flat structure. The TEM images, both structures failed to obtain informative results due to the beam damage (**Figure 4.5**).[25]
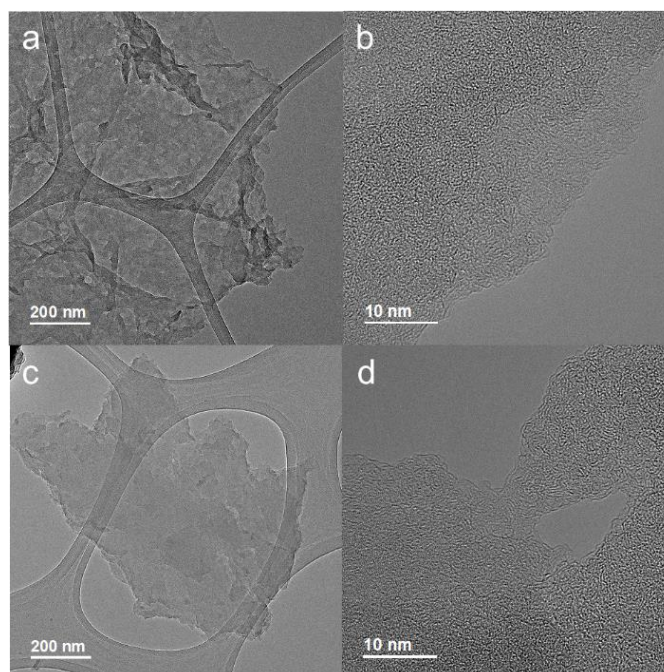
Figure 4.5. High-resolution transmission electron microscopy (HR-TEM) images of 2D-Standing network structure (a, b) and 2D-Flat structure (c, d) at different magnification.

The materials were characterized well with the thermogravimetric analysis (TGA) according to the dimensions of the structure (**Figure 4.2d**). On the contrary, the 2D-Flat structure shows high stability as it prevents external heat energy from penetrating. The flatness of the structure in the PSA process be it can reduce the cooling process and provide an energy advantage when carried out at high temperatures. However, it is seen as a trade-off relationship since the amount of gas adsorption decreases significantly (requires more cycles). Within this relationship, 2D-Standing structure designed in this study has the advantage of improving gas adsorption amount while blocking π-π interactions between layers.

Table 4.3. Table showing methane (CH_4) and nitrogen (N_2) absorption in two temperature, heat of adsorption and selectivity (at 293 K) by gas ratio for each structure

	CH_4 (mmol g^{-1})		N_2 (mmol g^{-1})		CH_4/N_2 Selectivity	
	293 K	298 K	293 K	298 K	50/50	80/20
2D-Flat	0.571	0.501	0.139	0.122	5.729	5.882
2D-Standing	0.837	0.769	0.221	0.205	4.947	5.044
3D-CON	0.989	0.899	0.279	0.252	4.420	4.371

Selectivity is calculated by IAST.
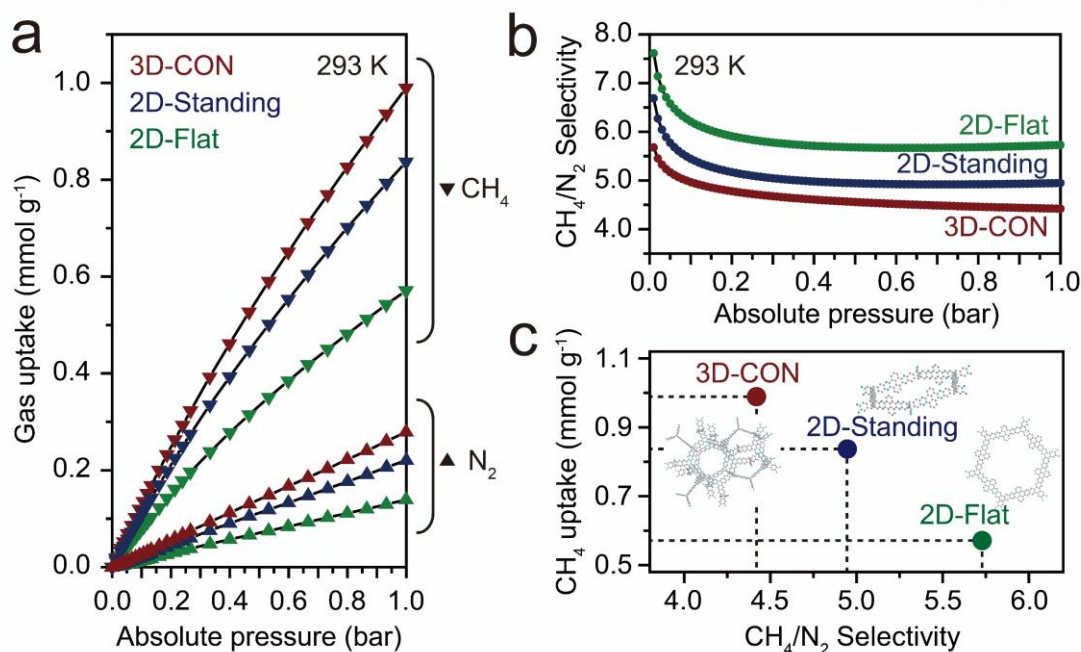
Figure 4.6. Gas adsorption properties of 2D-Standing, 2D-Flat and 3D-CON regarding CH_4 and N_2 at 293 K. (a) adsorption amount (mmol g^{-1}) of CH_4 (downward triangle) and N_2 (upward triangle). (b) the separation selectivity of IAST-predicted CH_4/N_2 mixture. (c) graph of CH_4 uptakes and selectivity trends for each structure. Dark blue stands for 2D-Standing, dark green for 2D-Flat and dark red stands for 3D-CON.
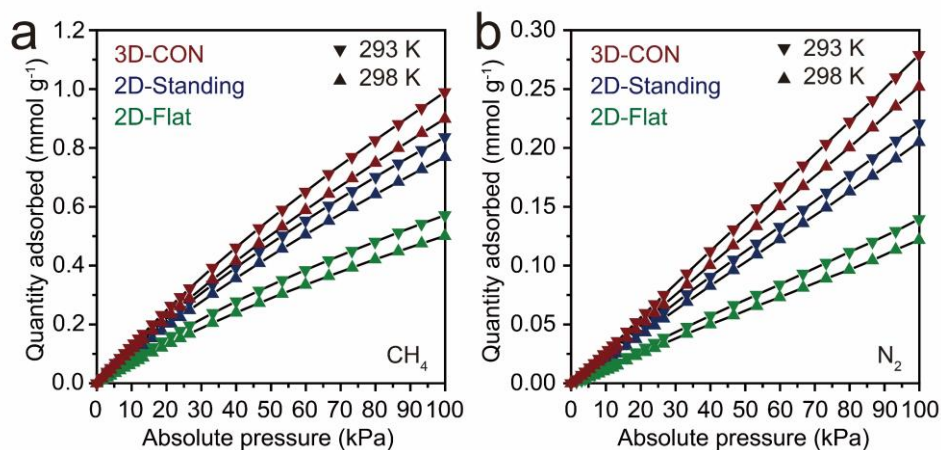
Figure 4.7. Gas adsorption amount regarding (a) CH_4 and (b) N_2. Both graphs show adsorption amount (mmol g^{-1}). Both graphs show the amount of adsorption (mmol g^{-1}), measured at 293 K (downward triangle) and 298 K (upward triangle). Dark red stands for 3D-CON, dark blue for 2D-Standing, and dark green for 2D-Flat.

To compare gas separation properties, adsorption of methane (CH_4) and dinitrogen (N_2) was conducted under two temperature conditions (293 K and 298 K) according to the characteristics of the structural dimension (**Figure 4.6**, **Figure 4.7**). The 3D-CON structure is a structure synthesized from the aromatization reaction of hexaketocyclohexane (HKH) with triptycene hexamine (THA) that

61

reported an excellent performance in hydrogen storage.[21] The reason for comparing 3D-CON is to see the characteristic differences in the direction of the arrangement of the triptycene for 2D-Standing structure. The adsorption of CH_4 under the 1 bar at 293 K condition showed that the 2D-Flat has 0.571 mmol g^{-1} (0.92 wt%), a 2D-Standing has 0.84 mmol g^{-1} (1.34 wt%), and a 3D-CON has 0.99 mmol g^{-1} (1.59 wt%) (**Figure 4.6a**). As to the N_2 uptakes, values 0.139 mmol g^{-1} (0.39 wt%), 0.221 mmol g^{-1} (0.62 wt%), and 0.279 mmol g^{-1} (0.78 wt%) are shown in order. 3D-CON shows the highest gas adsorption amount (**Figure 4.6a**, **Table 4.3**). The trend of gas uptake is increasing from 2D to 3D structure. The 2D-Standing and 3D-CON have structures of triptycene, which is known to be advantageous for gas adsorption, but differences in CH_4 and N_2 adsorption amount are due to the random arrangement (direction) of triptycene in the 3D-CON structure so that gases can easily access the microporous cages.

To calculate selectivity which is the binary gas mixture separation system, the single component curves were fitted by using Langmuir-Freundlich isotherm model. From the results, the separation selectivity of CH_4/N_2 (50:50) mixture were predicted by ideal adsorbed solution theory (IAST) (**Figure 4.6a**).[26] The value of IAST represents the 5.73, 4.95, and 4.42 in turn from 2D-Flat, 2D-Standing and 3D-CON (**Figure 4.6b**, **Table 4.3**). As expected, the structure in which the two-dimensional structure is layered has the best selectivity, and the larger the structural dimension, the greater the adsorption capacity, the less selective. Combining the preceding results, **Figure 4.6c** shows the relationship between CH_4 uptakes (mmol g^{-1}) and selectivity (293 K). The 2D-Standing showed intermediate values in adsorption amount of CH_4 and selectivity between 3D-CON and 2D-Flat. The advantage of the 2D-Standing structure is that it has the internal volume of the triptycene, which is advantageous for the absorption of gases, and that by avoiding the stacked structure, it is not necessary to consider the pore blockages caused by the stacking pattern. In addition, unlike 3D-CON, the structure grows in a 2D plane, so it has a consistent arrangement to separate the gas.

From a structural point of view, the 2D-Flat structure has a layered structure with non-covalent π-π stacking interactions, 2D-Standing structure has no such interactions, thereby maximizing the surface area in two dimensions. Both 2D-Standing and 3D-CON structures are triptycene-based networks. In other words, both have an intrinsic free volume, which is expected exhibit high gas adsorption amount in the stable network structure. The difference between the 2D-Standing and 3D-CON can be described based on the arrangement of triptycene units, in case of 2D-Standing the triptycene units are arranged in a standing 2D plane while in case of 3D-CON the triptycene units are arranged in a 3D space.

4.4 Conclusion

The newly designed standing-like 2D structure shows that it has 3D features while simultaneously having 2D features. There is no need to consider stacking compared to the conventional 2D materials. The trade-off relationship in the gas adsorption and separation, 2D-Standing structure showed the role

of a compromise. While this type of structure maintains symmetry, changing the monomer can create an infinite number of structures. Not only gas storage and separation, but it will also provide new material design strategies such as catalysts and energy materials, which will have a huge impact on polymeric material science.

4.5 Methods

4.5.1 Synthesis of fully-fused aromatic 2D-Standing network structure

In the 250 ml three-neck flask, triptycene hexamine (THA) hexahydrochloride (1.0 g, 1.7 mmol) and dihydropyrene-4,5,9,10-tetraone (0.70 g, 2.67 mmol) were taken in distilled trifluoromethanesulfonic acid (TFMSA, 35 ml) on ice bath. After stirring at 0 ˚C for 1 h, the ice bath was replaced with oil bath and gradually raised the temperature to 175 ˚C. Just after 1 h the later the thin liquid converted into like gel solid. The temperature was maintained for 2 h to ensure complete reaction and then cooled down to room temperature. The gel-like product was precipitated in deionized water and filtered on PTFE membrane (0.45 μm pore size). The collected product was Soxhlet extraction with water and MeOH for 3 days each and freeze dried at -120 ˚C under reduced pressure for 3 days.

4.5.2 Synthesis of fully-fused aromatic 2D-Flat network structure

Triphenylene hexamine (1.5 g, 2.79 mmol) and dihydropyrene-4,5,9,10-tetraone (1.09 g, 4.18 mmol) were mixed in TFMSA (40 ml) at ice bath. Then the mixture could reach room temperature for 12 h. Next, the temperature raised slowly to 175 ˚C at once and stirred for 3 h. The mixture was then cooled to room temperature and precipitated in deionized water. After precipitation, the refining process is identical to 2D-Standing.

4.5.3 Synthesis of 3D cage-like organic network (3D-CON)

Triptycene hexamine hexahydrochloride (0.5 g, 0.88 mmol) and hexaketocyclohexane (HKH) octahydrate (0.277 g, 0.88 mmol) were charged into the 3 neck round bottom flask containing TFMSA at 0 °C under nitrogen condition. The mixture was stirred for 1 h at 0 °C. Then the ice bath was replaced with oil bath and raised the temperature to 175 °C and stirred for 6 hours. The mixture was then cooled to room temperature and precipitated in deionized water. After precipitation, the refining process is identical to 2D-Standing.

4.6 Instrumentations

Powder X-ray diffraction (PXRD) studies were conducted with a High-Power X-Ray Diffractometer D/MAX2500V/PC (Cu-Kα radiation, 40 kV, 200 mA, λ = 1.54056 Å) (Rigaku Inc., Japan). Elemental analysis was studied by a Flash 2000 Analyzer (Thermo Scientific Inc., USA). N_2 adsorption isotherms at 77 K were measured using a Micromeritics 3Flex surface characterization analyzer (Micromeritics

Instruments, Norcross, GA, USA) and surface areas of each samples were calculated using the Brunauer-Emmett-Teller (BET) method within the consistency criteria. The methane and nitrogen adsorption isotherms at 293 and 298 K were also measured with the 3Flex analyzer. Thermogravimetric analysis (TGA) was conducted in air and in nitrogen atmosphere at a ramping rate of 10 °C min^{-1} by using STA 8000 (PerkinElmer Inc., USA). X-ray photoelectron spectroscopy (XPS) was collected by an X-ray Photoelectron Spectrometer K-alpha (Thermo Fisher Inc., USA). High-resolution transmission electron microscopy (HR-TEM) was performed by using a JEM-2100F microscope (JEOL Inc., Japan) under an operating voltage of 200 keV. CP/MAS ^{13}C NMR was measured by using VNMRS 600 (Agilent Technologies Inc., USA) with 20 kHz spinning rate.

4.7 References

(1)   Zhang, S. H.; Yang, Q.; Wang, C.; Luo, X. L.; Kim, J. H.; Wang, Z.; Yamauchi, Y. *Adv. Sci.* **2018**, *5*.

(2)   Mahmood, J.; Anjum, M. A. R.; Baek, J.-B. *Adv. Mater.* **2018**, *0*, 1805062.

(3)   Jiang, L. C.; Tian, Y. Y.; Sun, T.; Zhu, Y. L.; Ren, H.; Zou, X. Q.; Ma, Y. H.; Meihaus, K. R.; Long, J. R.; Zhu, G. S. *J. Am. Chem. Soc.* **2018**, *140*, 15724.

(4)   Yuan, Y.; Zhu, G. S. *ACS Central. Sci* **2019**, *5*, 409.

(5)   Fang, Q. R.; Wang, J. H.; Gu, S.; Kaspar, R. B.; Zhuang, Z. B.; Zheng, J.; Guo, H. X.; Qiu, S. L.; Yan, Y. S. *J. Am. Chem. Soc.* **2015**, *137*, 8352.

(6)   Lei, Z. D.; Yang, Q. S.; Xu, Y.; Guo, S. Y.; Sun, W. W.; Liu, H.; Lv, L. P.; Zhang, Y.; Wang, Y. *Nat. Commun.* **2018**, *9*.

(7)   Jeong, K.; Park, S.; Jung, G. Y.; Kim, S. H.; Lee, Y.-H.; Kwak, S. K.; Lee, S.-Y. *J. Am. Chem. Soc.* **2019**, *141*, 5880.

(8)   Mahmood, J.; Lee, E. K.; Jung, M.; Shin, D.; Jeon, I. Y.; Jung, S. M.; Choi, H. J.; Seo, J. M.; Bae, S. Y.; Sohn, S. D.; Park, N.; Oh, J. H.; Shin, H. J.; Baek, J. B. *Nat. Commun.* **2015**, *6*.

(9)   Mahmood, J.; Lee, E. K.; Jung, M.; Shin, D.; Choi, H. J.; Seo, J. M.; Jung, S. M.; Kim, D.; Li, F.; Lah, M. S.; Park, N.; Shin, H. J.; Oh, J. H.; Baek, J. B. *Proc. Natl. Acad. Sci. U.S.A.* **2016**, *113*, 7414.

(10)   Kou, Y.; Xu, Y. H.; Guo, Z. Q.; Jiang, D. L. *Angew. Chem. Int. Ed.* **2011**, *50*, 8753.

(11)   Meng, Z.; Aykanat, A.; Mirica, K. A. *Chem. Mater.* **2019**, *31*, 819.

(12)   Guo, J.; Xu, Y. H.; Jin, S. B.; Chen, L.; Kaji, T.; Honsho, Y.; Addicoat, M. A.; Kim, J.; Saeki, A.; Ihee, H.; Seki, S.; Irle, S.; Hiramoto, M.; Gao, J.; Jiang, D. L. *Nat. Commun.* **2013**, *4*.

(13)   Mahmood, J.; Li, F.; Jung, S. M.; Okyay, M. S.; Ahmad, I.; Kim, S. J.; Park, N.; Jeong, H. Y.; Baek, J. B. *Nat. Nanotech.* **2017**, *12*, 441.

(14)   Kim, S. J.; Mahmood, J.; Kim, C.; Han, G. F.; Kim, S. W.; Jung, S. M.; Zhu, G. M.; De Yoreo, J. J.; Kim, G.; Baek, J. B. *J. Am. Chem. Soc.* **2018**, *140*, 1737.

(15)   Mahmood, J.; Anjum, M. A. R.; Shin, S. H.; Ahmad, I.; Noh, H. J.; Kim, S. J.; Jeong, H. Y.; Lee,

J. S.; Baek, J. B. *Adv. Mater.* **2018**, *30*.

(16)   Belmabkhout, Y.; Bhatt, P. M.; Adil, K.; Pillai, R. S.; Cadiau, A.; Shkurenkol, A.; Maurin, G.; Liu, G. P.; Koros, W.; Eddaoudi, M. *Nat. Energy* **2018**, *3*, 1059.

(17)   Lin, R. B.; Li, L. B.; Zhou, H. L.; Wu, H.; He, C. H.; Li, S.; Krishna, R.; Li, J. P.; Zhou, W.; Chen, B. L. *Nat. Mater.* **2018**, *17*, 1128.

(18)   Kandambeth, S.; Dey, K.; Banerjee, R. *J. Am. Chem. Soc.* **2019**, *141*, 1807.

(19)   Wu, X. W.; Han, X.; Liu, Y. H.; Liu, Y.; Cui, Y. *J. Am. Chem. Soc.* **2018**, *140*, 16124.

(20)   Marco, A. B.; Cortizo-Lacalle, D.; Perez-Miqueo, I.; Valenti, G.; Boni, A.; Plas, J.; Strutynski, K.; De Feyter, S.; Paolucci, F.; Montes, M.; Khlobystov, A. N.; Melle-Franco, M.; Mateo-Alonso, A. *Angew. Chem. Int. Ed.* **2017**, *56*, 6946.

(21)   Mahmood, J.; Kim, S. J.; Noh, H. J.; Jung, S. M.; Ahmad, I.; Li, F.; Seo, J. M.; Baek, J. B. *Angew. Chem. Int. Ed.* **2018**, *57*, 3415.

(22)   Baker, R. W.; Lokhandwala, K. *Ind. Eng. Chem. Res.* **2008**, *47*, 2109.

(23)   Bhadra, S. J.; Farooq, S. *Ind. Eng. Chem. Res.* **2011**, *50*, 14030.

(24)   Rose, I.; Bezzu, C. G.; Carta, M.; Comesana-Gandara, B.; Lasseuguette, E.; Ferrari, M. C.; Bernardo, P.; Clarizia, G.; Fuoco, A.; Jansen, J. C.; Hart, K. E.; Liyana-Arachchi, T. P.; Colina, C. M.; McKeown, N. B. *Nat. Mater.* **2017**, *16*, 932.

(25)   Bhola, R.; Payamyar, P.; Murray, D. J.; Kumar, B.; Teator, A. J.; Schmidt, M. U.; Hammer, S. M.; Saha, A.; Sakamoto, J.; Schluter, A. D.; King, B. T. *J. Am. Chem. Soc.* **2013**, *135*, 14134.

(26)   Myers, A. L.; Prausnitz, J. M. *Aiche. J.* **1965**, *11*, 121.

V. Mechanochemically Induced Fe-Graphitic Nanoplatelets as Catalysts for the Oxidative Dehydrogenation

5.1 Abstract

Carbon-based catalysts have attracted much attention for the dehydrogenation (DH) of organic molecules, due to their rich active sites, high conversion efficiency and selectivity. However, because of their poor stability at high operation temperature (above 600 °C) and relatively high cost, their practical applications have been limited. Here, we report a simple ball-milling induced mechanochemical reaction which can introduce iron (Fe) and different functional groups (mostly stable aromatic C=O after heat-treatment) along the edges of graphene nanoplatelets. The resulting Fe-graphene nanoplatelets (Fe-XGnPs, X = H, C, N, or V) provide active sites for the oxidative dehydrogenation (ODH) of ethylbenzene into styrene. Among them, Fe-NGnPs (X = N) displayed the highest performance for styrene production at low temperature (~11.13 mmol g^{-1} h^{-1}, 450 °C) with high selectivity and durability.

5.2 Introduction

Dehydrogenation (DH) is an important reaction in the petroleum and polymer industries. For example, polystyrene (PS) is extensively produced by the DH of ethylbenzene (styrene, ST). In chemical industries, ethylbenzene (EB) DH is typically performed using metal-based catalysts such as potassium (K), molybdenum (Mo), and aluminum (Al) promoted iron oxide (Fe_2O_3).[1-2] At the same time, non-metallic catalysts based on nanostructured carbon-based materials such as heteroatom-doped carbon nanotubes (CNT), graphene, and ordered mesoporous carbon materials, have been intensively studied because they exhibit high conversion efficiency compared to metal oxides.[3-5] However, because their operating temperature is relatively high, the stability of carbon-based catalysts remains an important issue. In addition, a cost-effective synthesis method has yet to be developed.

Before they can be successfully employed for commercial uses, carbon-based catalysts need to be scalable at low-cost. One of the promising approaches, a mechanochemical reaction using ball-milling, has recently been shown to produce various types of edge-functionalized graphene nanoplatelets (EFGnPs).[6-12] EFGnPs produced by the mechanochemical ball-milling of graphite in the presence of different reactants have exhibited outstanding performance in energy conversion and storage applications.[13-19] The mechanochemical reaction has many advantages, including being an eco-friendly (less chemical waste), scalable, low-cost EFGnPs production method, which also allows selectivity of the functional groups at their edges.[8]

In contrast, the direct-DH process using excess steam requires high temperature (600-700 °C) and the consumption of a large quantity of energy to reduce coking on the surface of the catalysts. Compared

to direct-DH, oxidative dehydrogenation (ODH) is an energy saving process. From a thermodynamic viewpoint, the ODH process can produce much higher yields than the direct-DH process for the DH of ethylbenzene into styrene.[2]

The ODH reaction can be performed using several oxidizing agents, including oxygen, carbon dioxide, halogens, dinitrogen monoxide, and elemental sulfur. Among them, carbon dioxide (CO_2) is the most promising agent, because it can be a soft oxidant as well as a diluent. The others have undesirable side reactions, including burning carbon-based catalysts (their use at industrial scale can cause a serious explosion).[20] In addition, the reverse water-gas shift (RWGS) between CO_2 and H_2 is known to improve catalytic conversion via synergistic coupling reaction, as shown in Eq. (1).[21] In this study, therefore, ODH was selected as an energy saving process, with CO_2 as the oxidizing agent.[2, 20]

$$CO_2 + H_2 \rightleftarrows CO + H_2O \quad (1)$$

To investigate the catalytically active sites for ODH, the surface functionality of the EFGnPs was controlled by changing the milling conditions. GnP samples were produced by ball-milling graphite in the presence of hydrogen (H_2), carbon dioxide (CO_2), nitrogen (N_2), or vacuum (V), to produce XGnPs (X = H, C, N, or V). Depending on the specific combination in the ball-mill reactor, the reaction between the Fe atoms and active carbon species formed Fe-graphene nanoplatelet (Fe-XGnPs) structures. The Fe-XGnPs demonstrated efficient catalytic activity for ODH at low temperature (below 450 °C) with high selectivity and durability.

5.3 Results and Discussion

For the oxidative dehydrogenation (ODH) of ethylbenzene into styrene, a series of iron (Fe)-doped graphene nanoplatelets (Fe-XGnPs, X = H, C, N, or V) were prepared using the mechanochemical reaction by ball-milling under hydrogen (H_2), dry ice (solid state CO_2), nitrogen (N_2), or vacuum (V) (**Figure 5.1**). The stainless steel balls have two important roles: to induce the reaction between the active carbon species and chemical substances (H_2, CO_2, N_2, or vacuum) to form XGnPs, and for the *in-situ* doping of XGnPs with Fe to produce Fe-XGnPs. In a ball-mill container the high speed traveling stainless steel balls collide with graphite. During this process, they deliver enough kinetic energy to the graphitic framework to cause dissociation of the graphitic C-C and Fe-Fe bonds, and generate active carbon and Fe species.[7] This allows the formation of C-Fe bonds along the unzipped edges of the graphene nanoplatelets (GnPs) to produce Fe-GnPs. In addition, when the mechanochemical reaction is carried out in the presence of other chemical substance (*e.g.,* H_2, CO_2, N_2, or vacuum), the formation of C-*X'* bonds (*X'* = H, COOH, N, or V) can also occur at the graphitic edges, to yield Fe-XGnPs (X = H, C, N, or V).

All of the catalysts were produced using stainless steel balls with 5 mm diameters. Low Fe-doped NGnPs (LFe-NGnPs) were also produced using smaller balls (diameter: 3 mm) (*vide infra*). Because the smaller balls had much lower kinetic energy, a smaller amount of Fe could be doped.

To maximize catalytic activity and to ensure stability, the samples were annealed above the catalytic reaction temperature. After heat-treatment, only stable functional groups (aromatic N and C=O) were expected to remain on the Fe-XGnP catalysts. It is known that stable aromatic N- and carbonyl (C=O) groups on carbon-based catalysts contribute to the ODH of organic substances.
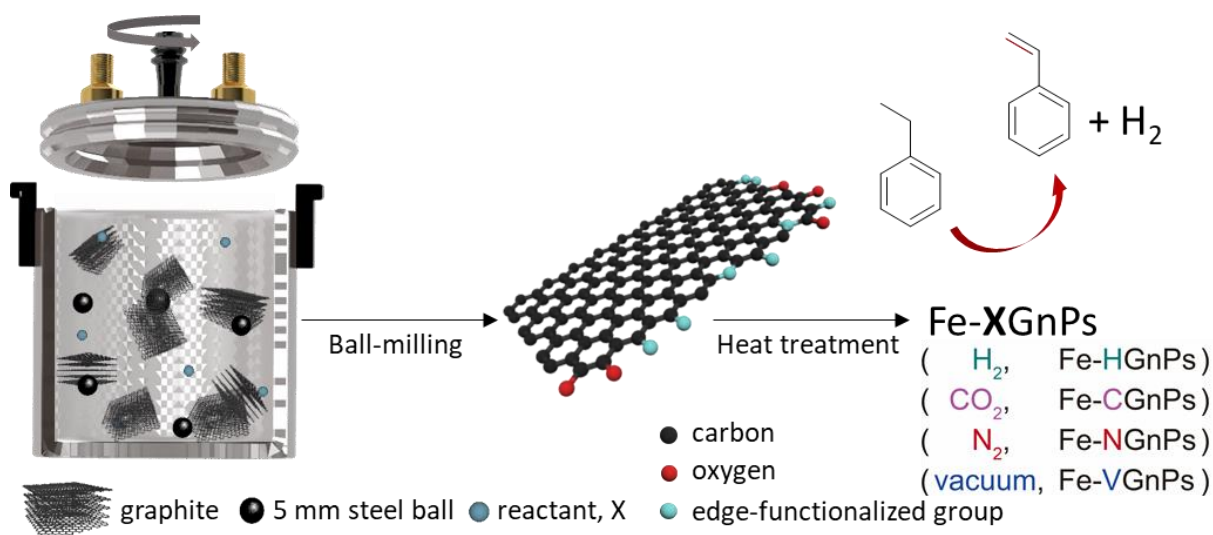
Figure 5.1. A schematic of the preparation of Fe-XGnP catalysts (X = H, C, N, or V) with *in-situ* Fe-doping, and functionalization with different elements at the edges of the graphene nanoplatelets (GnPs). After heat-treatment, the higher Fe content (5 mm balls) are designated Fe-XGnPs and the lower Fe-containing NGnPs (3 mm balls) are named LFe-NGnPs.
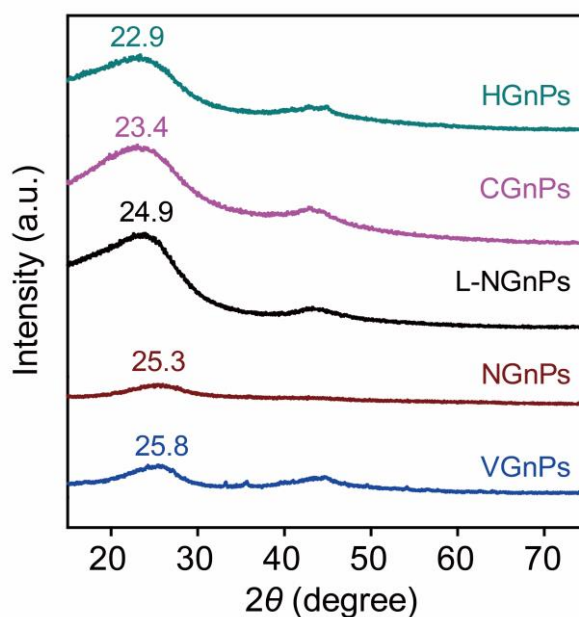
Figure 5.2. Powder X-ray diffraction patterns of XGnPs (X = H, C, N or V). L is lower Fe containing XGnPs (milled with 3 mm of steel balls).
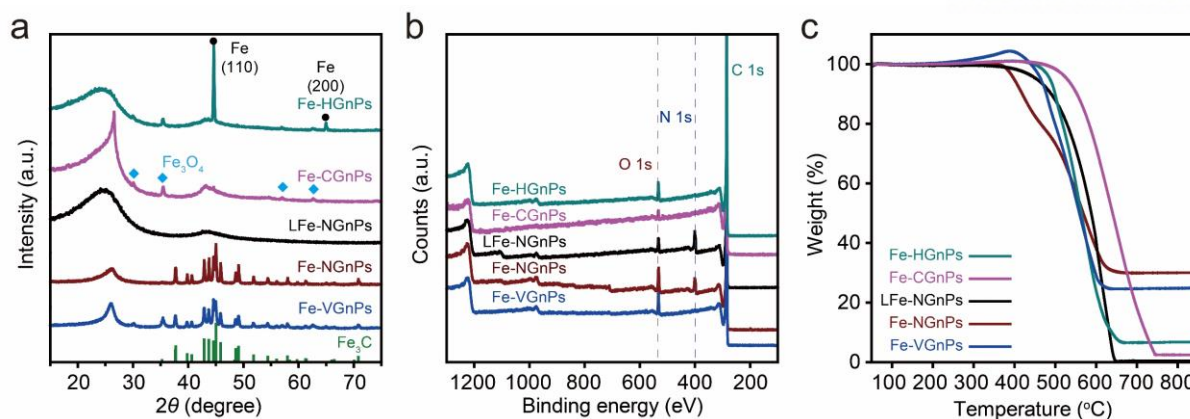
Figure 5.3. Structure analysis of heat-treated (L)Fe-XGnPs. **a**) Powder X-ray diffraction patterns; iron carbide (Fe$_3$C, dark green bars), iron oxide (main peaks of Fe$_3$O$_4$, sky blue square diamond dots) and Fe (black dots). **b**) Full XPS survey spectra. High-resolution survey spectra are shown in **Figure 5.4**. **c**) TGA thermograms obtained with a ramping rate of 10 °C min^{-1} in air, providing quantitative Fe contents in the samples based on char yields at 800 °C.

X-ray diffraction (XRD) patterns of the samples before and after annealing display a clear difference. While samples before heat-treatment show only broad (002) peaks associated with the *d*-spacing of graphitic layers (**Figure 5.2**), samples after heat-treatment at 700 °C in argon atmosphere display different diffraction patterns (**Figure 5.3a**) depending on the milling environment. For example, Fe-NGnPs and Fe-VGnPs mainly present sharp Fe$_3$C peaks, whereas Fe-HGnPs and Fe-CGnPs display bcc Fe and magnetite peaks (**Figure 5.3a**, ICDD no. 01-077-0255 (Fe$_3$C), 00-006-0696 (Fe), 98-000-0294 (Fe$_3$O$_4$)). The NGnPs (in nitrogen) and VGnPs (in vacuum) have plenty of binding sites to form Fe-N (NGnPs only) and Fe-C bonds. Atomically deposited Fe species along the broken edges of the NGnPs and VGnPs formed into Fe$_3$C and Fe particles upon heat-treatment.

In the Fe-NGnPs, the active carbon formed by the removal of nitrogen at high temperature can combine with oxygen to reduce Fe, and does not show oxidized Fe. However, since the VGnPs have no functional groups capable of reducing Fe, the Fe-VGnPs contain an oxide form (Fe$_3$O$_4$, magnetite).

Unlike the Fe-NGnPs and Fe-VGnPs, the Fe-HGnPs (in hydrogen) and Fe-CGnPs (in carbon dioxide) have no specific chemical binding sites for active Fe species, but Fe species physically trapped in the graphitic structure were thermally transformed into Fe particles. Fe-HGnPs have strong Fe peaks because the HGnPs have abundant hydrogen that can reduce Fe, whereas the Fe-CGnPs shows strong magnetite peaks, because the CGnPs do not have enough reducing elements.[8]

The heat-treated Fe-XGnPs (X = H, C, N, or V) catalysts were expected to have an enhanced graphitic structure and improved interaction between the C and Fe. The LFe-NGnPs, which were prepared from NGnPs using smaller steel balls (3 mm), had a broad XRD peak between 40-50 degrees because of the lower Fe content.
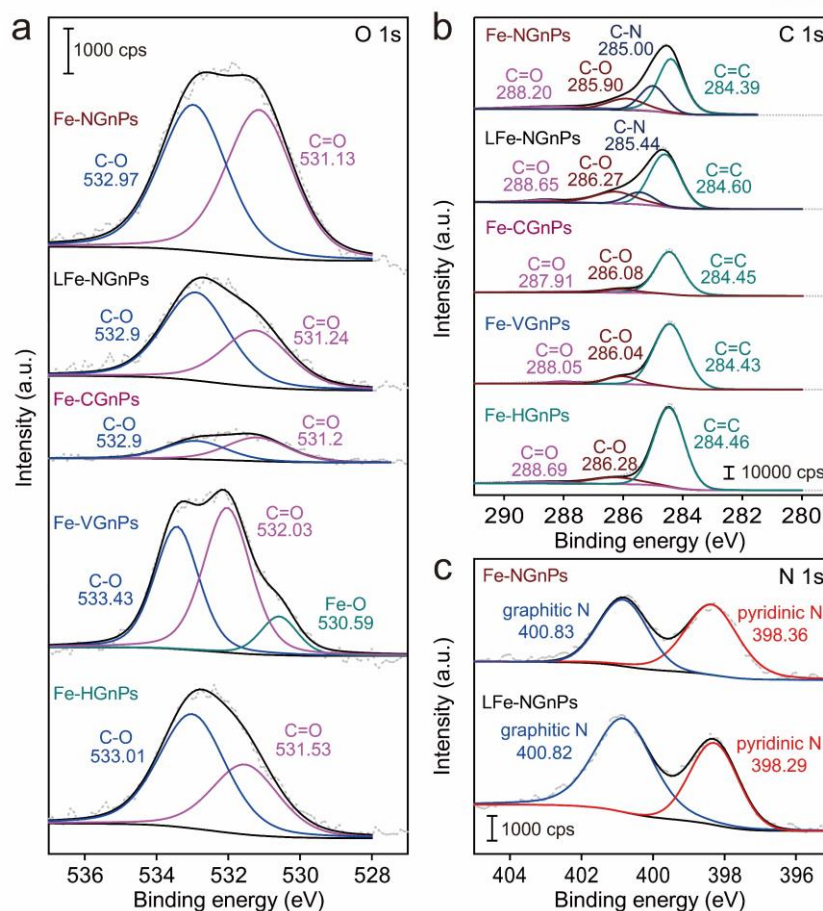
Figure 5.4. High-resolution XPS spectra of Fe-XGnPs: a) O 1s; b) C 1s and c) N 1s. Each intensity scale is shown in the graph.

X-ray photoelectron spectroscopy (XPS) spectra show the introduced elements and their bonding natures in (L)Fe-XGnPs (**Figure 5.3b**). As expected, the O 1s peak in each sample can be attributed to aromatic carbonyl (C=O) groups, which are the only stable oxygenated groups at the edges of the GnPs after heat-treatment at 700 °C in argon atmosphere (**Figure 5.4**).[22] Quantitative analysis of the elemental contents using XPS is not reliable, because XPS is more sensitive to the surface chemical composition (**Table 5.1**).[23] Elemental analysis (EA) and thermogravimetric analysis (TGA) are more straightforward methods to determine element contents. Fe contents in particular can be determined by analyzing the char yield of TGA in air.

The elemental analysis (EA) results show the difference between samples before and after heat-treatment (**Table 5.2**). Unexpectedly, the Fe-CGnPs displayed the lowest ratio of oxygen (O) to carbon (C), although their precursors were prepared with the most oxygen-rich substance, CO_2. This result supports the conclusion that CGnPs have abundant dangling oxygenated groups (*e.g.,* -COOH and -OH), which can be thermally stripped off during heat-treatment. Unlike the Fe-CGnPs, the Fe-NGnPs and Fe-VGnPs had higher O/C ratios, suggesting that they have the more stable aromatic C=O groups in their structures.

70

Thermogravimetric analysis (TGA) indicated that the Fe contents of Fe-NGnPs, Fe-VGnPs, Fe-HGnPs, Fe-CGnPs and LFe-NGnPs were 20.88, 16.82, 4.37, 1.65 and 0.30 wt%, respectively, based on char yields at 800 °C (as calculated from the residual weights of Fe_2O_3) (**Figure 5.3c**). Among the (L)Fe-XGnPs samples, the Fe-NGnPs and Fe-VGnPs contained high Fe contents, implying that the active carbon species were generated from broken graphitic C-C bonds, which have enough energy to form metal-C bonds with semimetals or post-transition metals.[10, 24]

In this work, active carbon species react with active Fe species in without (vacuum) or inactive reactant (nitrogen gas) to form C-Fe bonds. In contrast, the Fe-HGnPs and Fe-CGnPs have lower Fe contents, because active carbon species have a much greater chance of reacting with hydrogen (C-H) or carbon dioxide (C-COOH) than the active Fe species.

Table 5.1. Atomic compositions of (L)Fe-XGnPs before (top) and after (bottom) heat-treatment determined by X-ray photoelectron spectroscopy

Before heat-treatment	Element (at%)			
	C	N	O	Fe[a)]
Fe-HGnPs	89.21	-	10.49	0.30
Fe-CGnPs	83.40	-	16.38	0.21
LFe-NGnPs	83.03	9.34	7.16	0.46
Fe-NGnPs	69.17	15.18	14.08	1.57
Fe-VGnPs	89.36	-	10.64	-
After heat-treatment	Element (at%)			
	C	N	O	Fe
Fe-HGnPs	97.05	-	2.95	-
Fe-CGnPs	97.36	-	2.64	-
LFe-NGnPs	92.21	5.29	2.49	-
Fe-NGnPs	92.31	3.59	3.92	0.18
Fe-VGnPs	95.42	-	4.58	-

a) XPS has limitation to detect metallic elements with valence electrons in *d*- and *f*-orbitals.

The specific surface areas of samples before and after heat-treatment were determined using the Brunauer-Emmett-Teller (BET) method with nitrogen adsorption/desorption isotherms at 77 K (**Table 5.3**). Both the specific surface areas and total pore volumes were increased in all samples after heat-treatment, due to the removal of dangling edge-functional groups. This is expected to enhance the catalytic activity of (L)Fe-XGnPs *via* improved mass-transfer.

Table 5.2. Elemental analysis of (L)Fe-XGnPs before (top) and after (bottom) heat-treatments

Before heat-treatment	Element (wt%)					$O/C^{a)}$
	C	N	H	O	Total	
Fe-HGnPs	$78.46^{b)}$	-	2.35	15.76	96.57	0.20
Fe-CGnPs	69.07	-	1.72	30.68	101.47	0.44
LFe-NGnPs	71.60	8.88	1.55	14.55	96.58	0.20
Fe-NGnPs	57.92	14.61	1.12	15.88	89.53	0.27
Fe-VGnPs	74.70	0.46	0.54	9.35	85.05	0.13

After heat-treatment	Element (wt%)					O/C
	C	N	H	O	Total	
Fe-HGnPs	88.30	-	0.91	3.88	93.09 $(6.91)^{c)}$	0.04
Fe-CGnPs	95.45	-	0.86	1.36	97.67 (2.33)	0.01
LFe-NGnPs	83.55	8.70	0.87	8.04	101.16 (~0)	0.10
Fe-NGnPs	75.61	9.22	0.90	6.59	92.32 (7.68)	0.09
Fe-VGnPs	81.04	-	-	1.84	82.88 (17.12)	0.02

a) The ratios of oxygen (O) to carbon (C) in the samples.
b) The standard deviation (σ).
c) The numbers in parenthesis are estimated Fe content.

Table 5.3. Brunauer-Emmett-Teller (BET) analysis of (L)Fe-XGnPs before (left) and after (right) heat-treatments using nitrogen adsorption/desorption at 77 K

Sample (X)	Before heat treatment of (L)Fe-XGnPs			After heat treatment of (L)Fe-XGnPs		
	V_{total}	D_{mean}	SSA	V_{total}	D_{mean}	SSA
H	0.42	4.56	367.21	0.47	3.97	471.21
C	0.61	3.99	790.60	0.79	3.56	886.34
L-N	0.69	4.89	567.54	0.81	4.32	753.15
N	0.28	8.57	130.93	0.37	6.50	227.85
V	0.25	7.52	134.11	0.26	4.89	214.83

V_{total}: total pore volume ($cm^3\ g^{-1}$); D_{mean}: mean pore diameter (nm); SSA: specific surface area ($m^2\ g^{-1}$).

Following the structural analysis of the (L)Fe-XGnPs, their catalytic activity was evaluated in the temperature range of 350 to 500 °C at 50 °C intervals (**Figure 5.6a, 5.5 and 5.7**). Among the (L)Fe-XGnPs samples, the Fe-NGnPs showed the highest rate of styrene (ST) formation. The conversion ratio of ethylbenzene (EB) to ST increased with increasing temperature (**Figure 5.6b**). More importantly, the catalytic activity of Fe-NGnPs did not decay, even after five uses at 450 °C (**Figure 5.6c**).
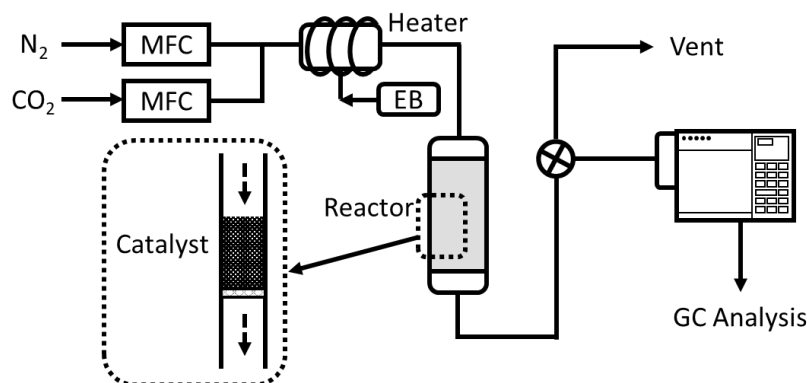

Figure 5.5. Schematic of the experimental setup. The syringe pump was used for ethylbenzene (EB) injection, and the nitrogen and carbon dioxide gases were controlled by a mass flow controller (MFC). The final products passing through the quartz reactor are analyzed by gas chromatography (GC).

The virtue of the Fe-NGnP catalyst is that is does not form by-products, such as benzene or toluene, up to 450 °C, while demonstrating ~99% selectivity. This is an important advantage for ST production because it removes the need for additional purification processes. Interestingly, when the reaction temperature approached 500 °C a side reaction occurred for all catalysts, and the rate of ST formation decreased (**Figure 5.8**). The catalytic performances of samples depended on their functional groups up to 450 °C, but at 500 °C they showed behaviors similar to those of commercially used iron oxide (Fe_xO_y)-based catalysts[2, 25] indicating that Fe sites are the primary contributors to the catalytic reaction around 500 °C. Overall, the most suitable temperature condition for (L)Fe-XGnPs was 450 °C, where it demonstrated a high rate of ST production with low energy consumption compared to other reported carbon-based catalysts (**Figure 5.6d, Table 5.4**).

To further investigate the factors affecting the ODH reaction, the active sites were divided into three parts: the metallic Fe, the defects of graphitic structure and the functional groups at the edges of GnPs. First, regarding the amount and activity of Fe, between 350-500 °C Fe_xO_y exists in the form of a magnetite (Fe_3O_4) structure (**Figure 5.9**). Magnetite has a lattice structure of Fe^{3+} (tetrahedral sites), Fe^{2+} (octahedral sites) and O^{2-} anion. Since iron oxide provides an adsorption site for EB,[26] catalysts containing large amounts of Fe typically have high conversion rates.[27] If Fe provides active sites and acts as a major contributing factor, it is reasonable to predict that Fe content will tend to be proportional to EB conversion. Based on **Figure 5.6a**, however, the Fe-HGnPs with low Fe content (4.37 wt%) also had higher conversion than Fe-VGnPs (16.82 wt%). Therefore, although the presence of iron oxide

enhances catalytic activity, it is still believed that the quantity of Fe is not a major contributing factor by itself but may produce a synergistic effect with other factors.

The defects in graphitic structure of the Fe-XGnPs' possible active sites was also investigated. During ball-milling, many carbon bonds are unzipped by the high kinetic energy. At the same time, the active carbon species along the broken edges bond with oxygen or hydrogen atoms to form edge C-O or C-H bonds.

The curvature of the carbon structure was checked using transmission electron microscopy (TEM) images (**Figure 5.10**). The formation of the open edge structure (the curvature of the edge), with its mixed sp^2 and sp^3 hybridization, leads to the partial delocalization of the electron density on its surface, which provides catalytic active sites.[1, 8, 28-29]
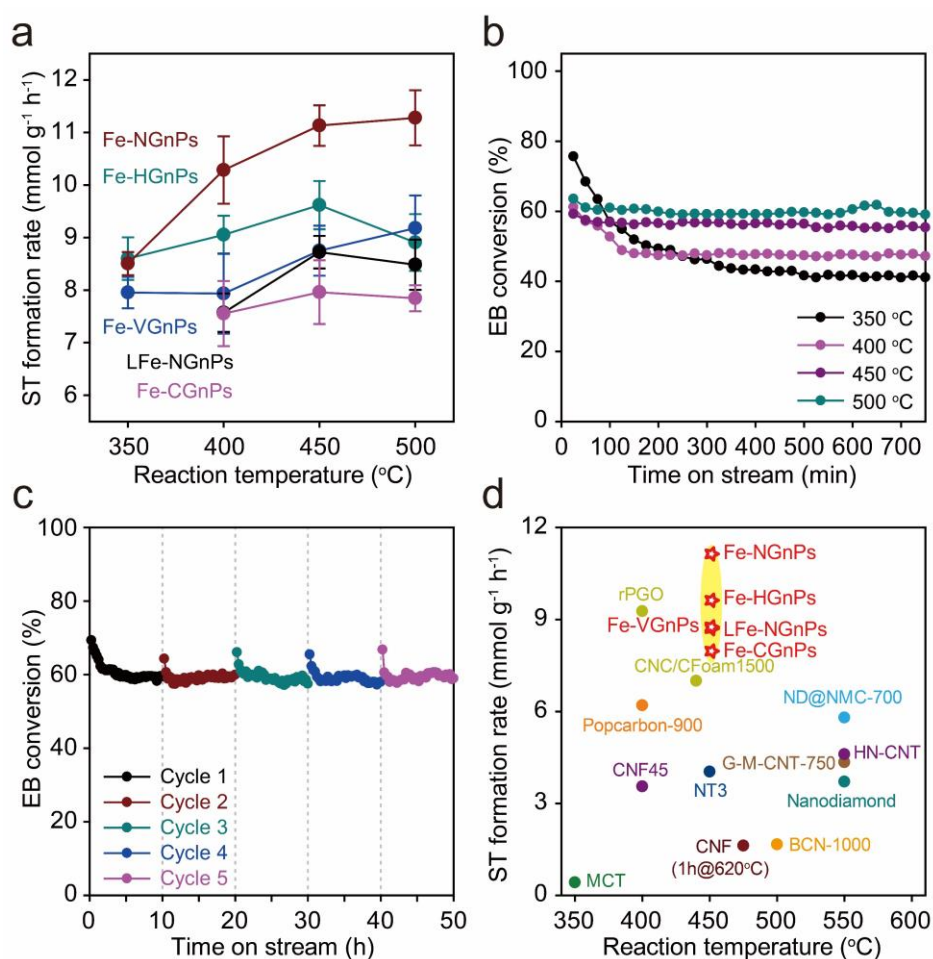
Figure 5.6. Catalytic properties of (L)Fe-XGnPs (X = H, C, N, or V) with respect to reaction duration time for the ODH of an ethylbenzene (EB) stream. **a**) The rate of styrene (ST) formation for each catalyst according to the reaction temperature. **b**) Conversion ratio of EB to ST using the Fe-NGnP catalyst with respect to reaction time and temperature. **c**) Durability test of the Fe-NGnP catalyst. **d**) Comparison of the rate of ST formation with reported carbon-based catalysts as a function of their reaction temperature (star shapes in the yellow region). Reaction conditions: 300 mg of catalyst, 100 μmol min^{-1} of EB/CO$_2$ (EB/CO$_2$ = 1) mixture, N$_2$ is a balance gas, and total flow rate is 10 ml min^{-1}.

Table 5.4. Styrene (ST) formation rate of various literature reported carbon-based ethylbenzene dehydrogenation catalysts

Catalyst	ST Production rate (mmol g^{-1} h^{-1})	Reaction temperature (°C), (SSA, m^2 g^{-1})	Reference
Fe-NGnP	11.13	450 (227.85)	*This work*
Fe-CGnP	7.96	450 (790.60)	*This work*
Fe-HGnP	9.62	450 (471.21)	*This work*
Fe-VGnP	8.75	450 (214.83)	*This work*
LFe-NGnP	8.72	450 (753.15)	*This work*
BCN-1000	1.66	500 (1449)	*Angew. Chem. Int. Ed.* **2017**, 56, 8231-8235
rPGO	9.27	400 (2613)	*Chem. Commun.* **2015**, 51, 3423-3425
Nanodiamond	3.09-4.33	550 (*300-420)	*Angew. Chem. Int. Ed.* **2010**, 49, 8640-8644
NT3	4.03	450 (271)	*Carbon* **2004**, 42, 2807-2813
CNF45	3.55	400 (52.1)	*Appl. Catal. A* **2007**, 323, 135-146
CNF(1h@620°C)	1.62	475 (58.8)	*Catal. Today* **2012**, 186, 93-98
Popcarbon-900	6.2	400 (1417)	*Chem. Mater.* **2007**, 19, 2894-2897
CNC/CFoam1500	7.0	440 (129)	*Carbon* **2013**, 60, 514-522
MCT	0.42	350 (5)	*J. Am. Chem. Soc.* **2009**, 131, 11296-11297
ND@NMC-700	5.8	550 (305)	*Catal. Today* **2018**, 301, 38-47
G-M-CNT-750	4.34	550 (477)	*ChemCatChem* **2015**, 7, 1135-1144
HN-CNT	4.6	550 (349)	*RSC Adv.* **2015**, 5, 53095-53099

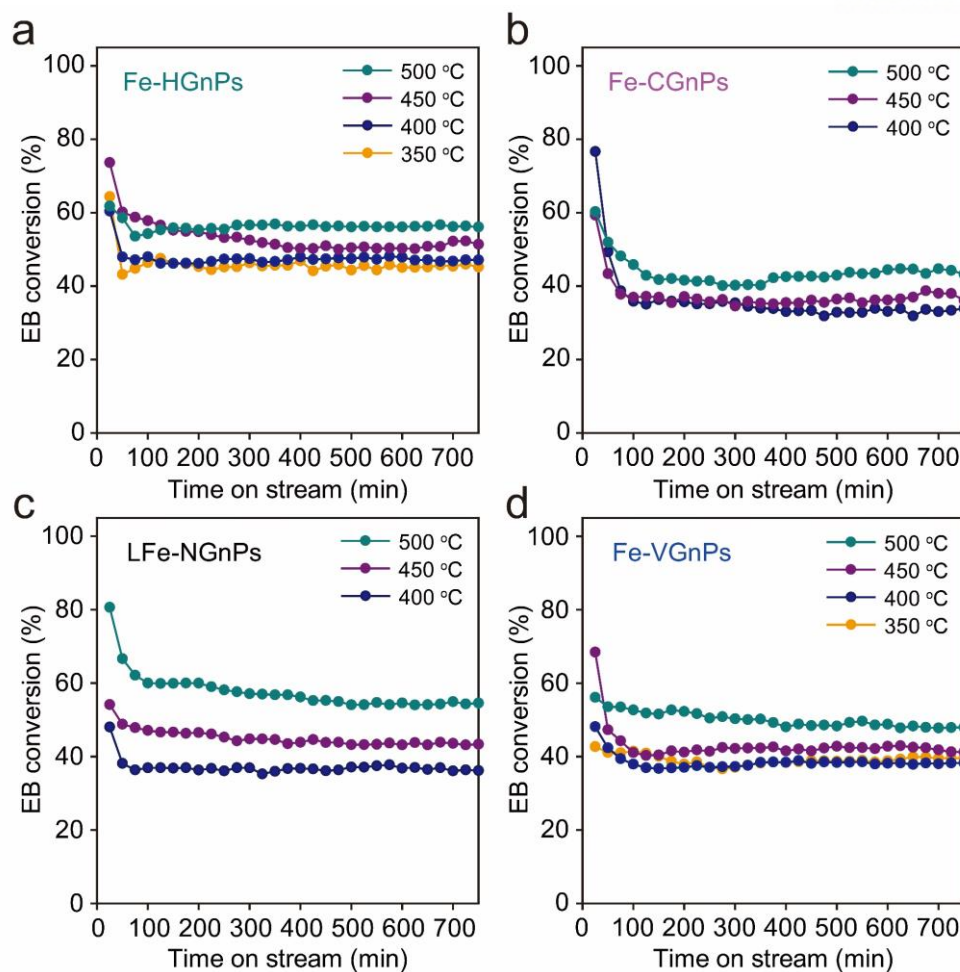*From Beijing Grish Hitech Co. (China), SN20130806165324601.

Figure 5.7. Oxidative dehydrogenation reaction of Fe-XGnPs catalysts with time and temperature. In case of Fe-CGnPs and LFe-NGnPs, the conversion was unstable at 350 °C and the graph was not shown in the graph.
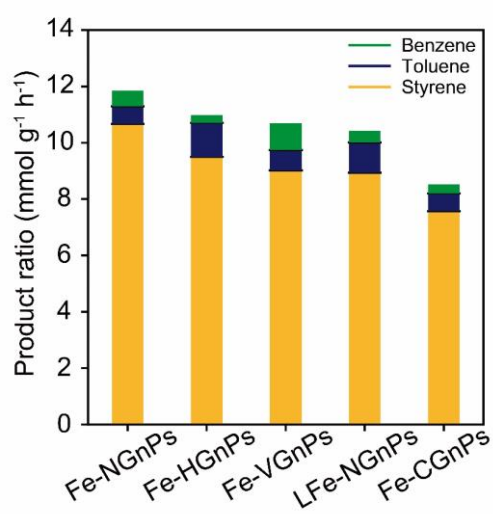

Figure 5.8. The product ratio of each catalyst from oxidative dehydrogenation reaction at 500 °C. The data were collected after 10 h reaction.
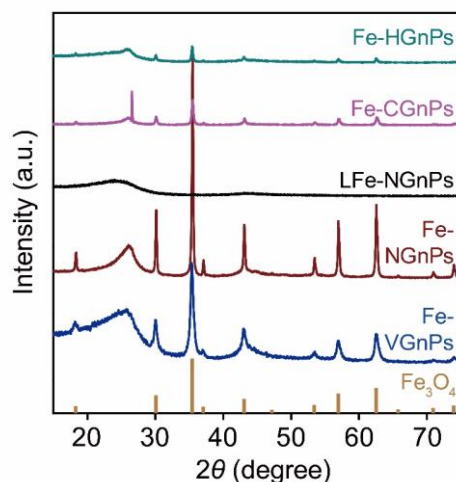
Figure 5.9. Powder X-ray diffraction patterns: Fe-XGnPs after ODH reaction (Fe₃O₄ is marked as red bar, ICDD no. 98-000-0294).
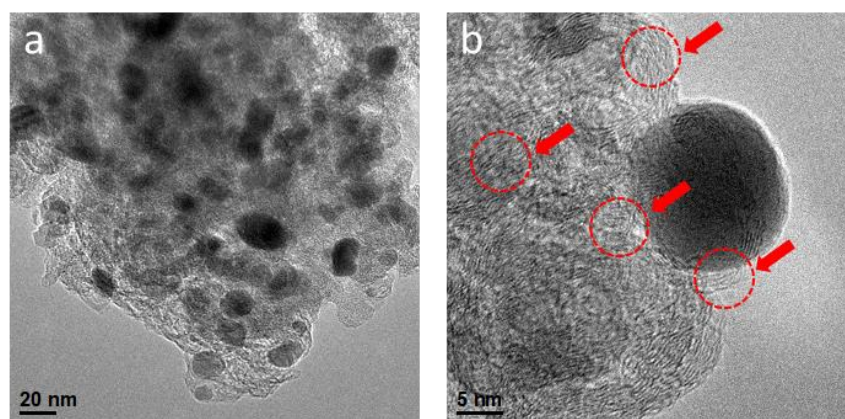
Figure 5.10. TEM images of Fe-NGnPs. a) Low magnification image. b) High magnification image. Red arrows indicate the structural curvatures.

For the Fe-HGnPs milled in the hydrogen environment, the reaction between carboradicals and hydrogen molecules is relatively fast and results in many edge C-H defects.[8] In the case of Fe-NGnPs and Fe-CGnPs, the strong kinetic energy creates many active carbon species along the cracked edge lines. When exposed to air, the active carbon species react with air moisture, resulting in oxygenated groups at their edges, causing edge delamination and producing a large interlayer distance than graphite (**Figure 5.2**).

Unlike the case described above, Fe-VGnPs milled in a vacuum condition had a relatively small amount of remaining active carbon species due to the formation of iron-carbon (Fe-C) bonds at the edges, and the LFe-NGnPs milled with 3 mm stainless steel balls had a small number of defects, as compared with Fe-NGnPs, since the balls possess a much lower kinetic energy (only 21.6% of the energy of 5 mm stainless steel balls).

77

Figure 5.11. Fourier transform infrared (FT-IR) spectra of Fe-XGnPs. The peak ranges from 1400 to 1750 cm^{-1} of the measured IR is indicated by an enlarged scale on the right graph. The ketone groups remaining in the heat-treated (700 °C) multilayers of graphene nanoplatelets are observed in the form of shoulders due to overlapping with the C=C peak.

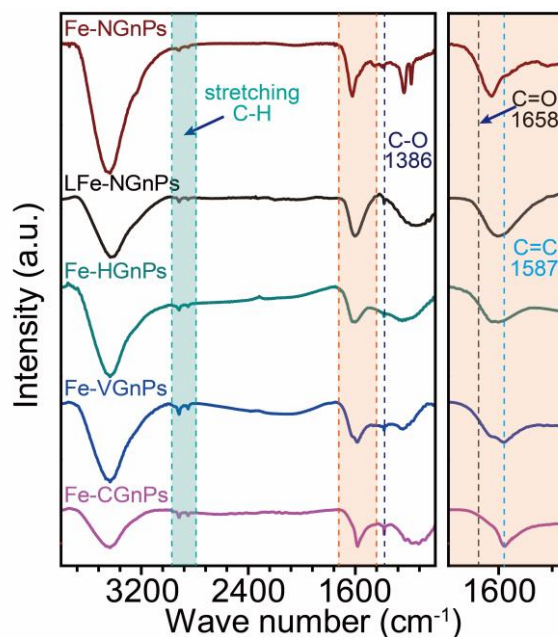In terms of functionality, it is well known that stable aromatic carbonyl (C=O) groups on carbon-based catalysts contribute to the oxidative dehydrogenation of organic substances.[3, 30-38] The C=O bonds affect electron density at the edges of the GnPs, and they can activate saturated hydrocarbons as Lewis bases.[1]

The presence of C=O bonds in the (L)Fe-XGnPs was confirmed from a Fourier transform infrared (FT-IR) spectrum (**Figure 5.11**), with a peak at 1658 cm^{-1}.[22] In the EA results (**Table 5.2**), the Fe-NGnPs exhibited the relatively larger oxygen content (O/C ratio = 0.0913), followed by Fe-HGnPs (0.0439), Fe-VGnPs (0.0227), and Fe-CGnPs (0.0142). Oxygen content after heat-treatment is mostly associated with stable aromatic C=O bonds,[22] and hence the higher O/C ratio can mainly be associated with the higher presence of C=O bonds in the samples.

As shown in **Figure 5.6a**, the rates for ST production follow a tendency similar to that of O content (C=O) (the LFe-NGnPs were not considered, to exclude the effect of Fe content). In the (L)Fe-NGnPs, the local electronic structure of the C-N bonds enhances the activation of hydrocarbon for ODH.[30, 39-40]

Based on the experimental results, among all Fe-XGnPs samples, the Fe-NGnPs showed the highest catalytic activity, mainly due to the combination of three factors: the metallic sites, edge defects, and polar functionality (aromatic N and C=O groups) at the edges of the GnPs. In our experimental results, the amount of Fe and the ratio of O/C (aromatic C=O) tended to fit the ODH reaction performance.

5.4 Conclusions

In summary, a series of (L)Fe-XGnPs were synthesized to evaluate their catalytic activity for oxidative dehydrogenation (ODH) of ethylbenzene (EB) into styrene (ST). (L)Fe-XGnPs were prepared by a simple mechanochemical reaction, which is an eco-friendly method for scalable production at low-cost for industrial application. The compositions of the catalysts can also be controlled by the reaction conditions (*e.g.,* H_2, CO_2, N_2, or vacuum). The low temperature ODH catalytic activity of Fe-XGnPs provides economic benefits and avoids unnecessary energy consumption as well as side reactions.

The experimental results can be interpreted to indicate that the ODH catalysts are affected not only by the amount of Fe, but also by the stable aromatic nitrogen and oxygen (C=O) functionalities and the ratio of edge defects on the carbon frameworks. The mechanochemical reaction used to prepare the catalysts are useful for controlling the milling environment and determining optimum conditions. Mechanochemically obtained Fe-XGnP materials can be cost-effective catalysts for ODH with high activity, selectivity and durability, and their performance suggests the design and synthesis of various other reaction catalysts. The results in this study also indicate that the simple ball-milling method can be useful for imparting various catalytic active sites and thus widening applications to various other organic reactions.

5.5 Materials

All solvents were purchased from Sigma-Aldrich Chemical Inc., unless otherwise stated. Edge-functionalized GnPs (XGnPs) were synthesized by using a pristine graphite (Alfa Aesar, natural graphite powder, 100 mesh, 99.9995% metal basis, Lot#14735).

5.6 Instrumentations

Ball-milling was performed by Pulverisette 6 (Fritsch Inc, GER). Powder X-ray diffraction (PXRD) studies were conducted with a High-Power X-Ray Diffractometer D/MAX2500V/PC (Cu-Kα radiation, 40 kV, 200 mA, λ = 1.54056 Å) (Rigaku Inc., Japan). Elemental analysis was studied by a Flash 2000 Analyzer (Thermo Scientific Inc., USA), Nitrogen adsorption isotherms was done by using the Brunauer-Emmett-Teller (BET) method on BELSORP-max (BEL Japan Inc., Japan). Thermogravimetric analysis (TGA) was conducted in air and in nitrogen atmosphere at a ramping rate of 10 °C min^{-1} by using STA 8000 (PerkinElmer Inc., USA). X-ray photoelectron spectroscopy (XPS) was collected by an X-ray Photoelectron Spectrometer K-alpha (Thermo Fisher Inc., USA). High-resolution transmission electron microscopy (HR-TEM) was performed by using a JEM-2100F microscope (JEOL Inc., Japan) under an operating voltage of 200 keV. The oxidative dehydrogenation performance was studied by Agilent 7890B gas chromatograph instrument (Agilent Technologies Inc., USA) with a DB-1 capillary column connected to a flame ionization detector (FID). Fourier transform infrared (FT-IR) was carried out by using Spectrum 100 (PerkinElmer Inc., USA).

5.7 Preparation of catalysts

5.7.1 Preparation of (L)Fe-XGnPs

XGnPs as precursor were prepared by ball-milling with the pristine graphite (5 g) and various reactants like as nitrogen gas (10 bar), carbon dioxide (dry ice, 100 g), hydrogen gas (10 bar) or vacuum condition. The container was sealed and charged after five charging-discharging cycles with Ar (10 bar) to remove air. The pristine graphite was placed into a stainless-steel container (500 mL) containing stainless steel balls (500.0 g, diameter 5 mm; LFe-NGnPs were milled by 3 mm ball with an increased loading of 15 g graphite for 10 h in the same condition) and then it was fixed in the planetary ball-mill machine and agitated at 500 rpm for 48 h. The resultant products were treated with 1 M aq. HCl solution to remove metallic impurities. Final product was freeze-dried at −120 °C under a reduced pressure (0.05 mmHg) for 48 h to yield XGnPs (NGnPs: 5.62 g; CGnPs: 6.29g; HGnPs: 5.41 g; VGnPs: 5.71g; L-NGnPs: 15.21 g).

5.7.2 Heat-treatment process of (L)Fe-XGnPs

Edge-functionalized graphene nanoplates (XGnPs, 2.0 g) was loaded on tube furnace. Those were treated in Ar atmosphere at 700 °C for 2 hours and then the resultant catalysts were collected and named as low iron containing edge-functionalized graphene nanoplatelets, Fe-XGnPs (Fe-NGnPs: 1.71 g; Fe-CGnPs: 1.68 g; Fe-HGnPs: 1.72 g; Fe-VGnPs: 1.66 g; LFe-NGnPs: 1.74 g).

5.8 Oxidative dehydrogenation reaction procedure

Oxidative dehydrogenation reaction was carried out in a fixed bed quartz reactor. 300 mg of catalyst (Fe-NGnPs, Fe-HGnPs, Fe-CGnPs, Fe-VGnPs and LFe-NGnPs) was loaded and preheated to 500 °C in N_2 flow. Ethylbenzene was injected with 0.1 mmol min^{-1} in N_2 and CO_2 gases flow (EB/CO_2 = 1, total 10 ml min^{-1}). The products were analyzed by Agilent 7890B gas chromatograph (GC) instrument with a DB-1capillary column connected to a flame ionization detector (FID). The GC calibration was done by micro liter scale syringe (Agilent gold standard, P05-G1717). The conversion (X_{EB}), and selectivity of styrene (S_{ST}) were calculated by Eq. (2) and (3).

$$X_{EB} \ (Conversion, \%) = \left(1 - \frac{EB_{out}}{EB_{in}}\right) \times 100 \ \ (2)$$

$$S_{ST} \ (Selectivity, \%) = \left(\frac{ST_{out}}{EB_{in} - EB_{out}}\right) \times 100 \ \ (3)$$

All the experiments were repeated, and **Figure 5.6a** of the main text shows the results of the triplicate experiment by calculating the mean and standard deviation.

5.9 References

(1)   Zhang, J. A.; Su, D. S.; Blume, R.; Schlogl, R.; Wang, R.; Yang, X. G.; Gajovic, A. *Angew. Chem. Int. Ed.* **2010**, *49*, 8640.

(2)   Mimura, N.; Saito, M. *Catal. Today* **2000**, *55*, 173.

(3)   Diao, J. Y.; Liu, H. Y.; Wang, J.; Feng, Z. B.; Chen, T.; Miao, C. X.; Yang, W. M.; Su, D. S. *Chem. Commun.* **2015**, *51*, 3423.

(4)   Su, D. S.; Perathoner, S.; Centi, G. *Chem. Rev.* **2013**, *113*, 5782.

(5)   Navalon, S.; Dhakshinamoorthy, A.; Alvaro, M.; Garcia, H. *Chem. Rev.* **2014**, *114*, 6179.

(6)   Jeon, I. Y.; Choi, H. J.; Ju, M. J.; Choi, I. T.; Lim, K.; Ko, J.; Kim, H. K.; Kim, J. C.; Lee, J. J.; Shin, D.; Jung, S. M.; Seo, J. M.; Kim, M. J.; Park, N.; Dai, L.; Baek, J. B. *Sci. Rep.* **2013**, *3*.

(7)   Jeon, I. Y.; Shin, Y. R.; Sohn, G. J.; Choi, H. J.; Bae, S. Y.; Mahmood, J.; Jung, S. M.; Seo, J. M.; Kim, M. J.; Wook Chang, D.; Dai, L.; Baek, J. B. *Proc. Natl. Acad. Sci. U.S.A.* **2012**, *109*, 5588.

(8)   Jeon, I. Y.; Choi, H. J.; Jung, S. M.; Seo, J. M.; Kim, M. J.; Dai, L. M.; Baek, J. B. *J. Am. Chem. Soc.* **2013**, *135*, 1386.

(9)   Jeon, I.-Y.; Choi, H.-J.; Ju, M. J.; Choi, I. T.; Lim, K.; Ko, J.; Kim, H. K.; Kim, J. C.; Lee, J.-J.; Shin, D.; Jung, S.-M.; Seo, J.-M.; Kim, M.-J.; Park, N.; Dai, L.; Baek, J.-B. *Sci. Rep.* **2013**, *3*, 2260.

(10)   Jeon, I. Y.; Choi, M.; Choi, H. J.; Jung, S. M.; Kim, M. J.; Seo, J. M.; Bae, S. Y.; Yoo, S.; Kim, G.; Jeong, H. Y.; Park, N.; Baek, J. B. *Nat. Commun.* **2015**, *6*.

(11)   Jeon, I. Y.; Bae, S. Y.; Seo, J. M.; Baek, J. B. *Adv. Funct. Mater.* **2015**, *25*, 6961.

(12)   Jeon, I. Y.; Zhang, S.; Zhang, L. P.; Choi, H. J.; Seo, J. M.; Xia, Z. H.; Dai, L. M.; Baek, J. B. *Adv. Mater.* **2013**, *25*, 6138.

(13)   Ju, M. J.; Jeon, I. Y.; Lim, K.; Kim, J. C.; Choi, H. J.; Choi, I. T.; Eom, Y. K.; Kwon, Y. J.; Ko, J.; Lee, J. J.; Baek, J. B.; Kim, H. K. *Energ. Environ. Sci.* **2014**, *7*, 1044.

(14)   Ju, M. J.; Jeon, I. Y.; Kim, J. C.; Lim, K.; Choi, H. J.; Jung, S. M.; Choi, I. T.; Eom, Y. K.; Kwon, Y. J.; Ko, J.; Lee, J. J.; Kim, H. K.; Baek, J. B. *Adv. Mater.* **2014**, *26*, 3055.

(15)   Ju, M. J.; Jeon, I. Y.; Kim, H. M.; Choi, J. I.; Jung, S. M.; Seo, J. M.; Choi, I. T.; Kang, S. H.; Kim, H. S.; Noh, M. J.; Lee, J. J.; Jeong, H. Y.; Kim, H. K.; Kim, Y. H.; Baek, J. B. *Sci. Adv.* **2016**, *2*.

(16)   Ju, M. J.; Kim, J. C.; Choi, H. J.; Choi, I. T.; Kim, S. G.; Lim, K.; Ko, J.; Lee, J. J.; Jeon, I. Y.; Baek, J. B.; Kim, H. K. *ACS Nano* **2013**, *7*, 5243.

(17)   Jeon, I. Y.; Kim, H. M.; Choi, I. T.; Lim, K.; Ko, J.; Kim, J. C.; Choi, H. J.; Ju, M. J.; Lee, J. J.; Kim, H. K.; Baek, J. B. *Nano Energy* **2015**, *13*, 336.

(18)   Xu, J. T.; Jeon, I. Y.; Seo, J. M.; Dou, S. X.; Dai, L. M.; Baek, J. B. *Adv. Mater.* **2014**, *26*, 7317.

(19)   Jeon, I. Y.; Ju, M. J.; Xu, J. T.; Choi, H. J.; Seo, J. M.; Kim, M. J.; Choi, I. T.; Kim, H. M.; Kim, J. C.; Lee, J. J.; Liu, H. K.; Kim, H. K.; Dou, S. X.; Dai, L. M.; Baek, J. B. *Adv. Funct. Mater.* **2015**, *25*, 1170.

(20)   Zhang, L.; Wu, Z. L.; Nelson, N. C.; Sadow, A. D.; Slowing, I. I.; Overbury, S. H. *ACS Catal.*

2015, *5*, 6426.

(21)   Sun, A. L.; Qin, Z. F.; Chen, S. W.; Wang, J. G. *J. Mol. Catal. A-Chem.* **2004**, *210*, 189.

(22)   Acik, M.; Lee, G.; Mattevi, C.; Pirkle, A.; Wallace, R. M.; Chhowalla, M.; Cho, K.; Chabal, Y. *J. Phys. Chem. C* **2011**, *115*, 19761.

(23)   Shard, A. G. *Surf. Interface Anal.* **2014**, *46*, 175.

(24)   Xu, J.; Jeon, I. Y.; Choi, H. J.; Kim, S. J.; Shin, S. H.; Park, N.; Dai, L. M.; Baek, J. B. *2D Mater.* **2017**, *4*.

(25)   Castro, A. J. R.; Soares, J. M.; Filho, J. M.; Oliveira, A. C.; Campos, A.; Milet, E. R. C. *Fuel* **2013**, *108*, 740.

(26)   Schule, A.; Nieken, U.; Shekhah, O.; Ranke, W.; Schlogl, R.; Kolios, G. *Phys. Chem. Chem. Phys.* **2007**, *9*, 3619.

(27)   Sekine, Y.; Watanabe, R.; Matsukata, M.; Kikuchi, E. *Catal. Lett.* **2008**, *125*, 215.

(28)   Liang, C. D.; Xie, H.; Schwartz, V.; Howe, J.; Dai, S.; Overbury, S. H. *J. Am. Chem. Soc.* **2009**, *131*, 7735.

(29)   Schwartz, V.; Fu, W. J.; Tsai, Y. T.; Meyer, H. M.; Rondinone, A. J.; Chen, J. H.; Wu, Z. L.; Overbury, S. H.; Liang, C. D. *ChemSusChem* **2013**, *6*, 840.

(30)   Zhao, Z. K.; Dai, Y. T.; Lin, J. H.; Wang, G. R. *Chem. Mater.* **2014**, *26*, 3151.

(31)   Su, C. L.; Acik, M.; Takai, K.; Lu, J.; Hao, S. J.; Zheng, Y.; Wu, P. P.; Bao, Q. L.; Enoki, T.; Chabal, Y. J.; Loh, K. P. *Nat. Commun.* **2012**, *3*.

(32)   Guo, X. L.; Qi, W.; Liu, W.; Yan, P. Q.; Li, F.; Liang, C. H.; Su, D. S. *ACS Catal.* **2017**, *7*, 1424.

(33)   Zhao, Z. K.; Dai, Y. T.; Ge, G. F.; Guo, X. W.; Wang, G. R. *RSC Adv.* **2015**, *5*, 53095.

(34)   Thanh, T. T.; Ba, H.; Lai, T. P.; Nhut, J. M.; Ersen, O.; Begin, D.; Janowska, I.; Nguyen, D. L.; Granger, P.; Cuong, P. H. *J. Mater. Chem. A* **2014**, *2*, 11349.

(35)   Zhao, Z. K.; Dai, Y. T.; Ge, G. F. *Catal. Sci. Technol.* **2015**, *5*, 1548.

(36)   Zhao, Z. K.; Dai, Y. T. *J. Mater. Chem. A* **2014**, *2*, 13442.

(37)   Qi, W.; Yan, P. Q.; Su, D. S. *Acc. Chem. Res.* **2018**, *51*, 640.

(38)   Qi, W.; Liu, W.; Guo, X. L.; Schlogl, R.; Su, D. S. *Angew. Chem. Int. Ed.* **2015**, *54*, 13682.

(39)   Zhao, Z. K.; Dai, Y. T.; Ge, G. F.; Guo, X. W.; Wang, G. R. *Phys. Chem. Chem. Phys.* **2015**, *17*, 18895.

(40)   Zhao, Z. K.; Dai, Y. T.; Ge, G. F.; Mao, Q.; Rong, Z. M.; Wang, G. R. *ChemCatChem* **2015**, *7*, 1070.

Appendix I. Curriculum Vitae

Seok-Jin Kim

School of Energy Engineering/Center for Dimension-Controllable Organic Frameworks, Ulsan National Institute of Science and Technology (UNIST), 50 UNIST-gil, Ulsan 44919, South Korea | seokjinkim@unist.ac.kr, sjkim1583@gmail.com | +82-52-217-2571

■ **Research Field**

Synthesis and application of aromatic network polymer for energy materials

■ **Education**

- Mar. 2011 – Aug. 2014	Bachelor's Degree (Energy Engineering & Material Engineering) in UNIST Advisor: Prof. *Jong-Beom Baek* & Prof. *Soon-Yong Kwon*
- Sep. 2014 –Aug. 2019	Combined Master's and Doctoral Course (Energy Engineering) in UNIST Advisor: Prof. *Jong-Beom Baek*

■ **Note**

- Mar. 2014 – Feb. 2016	Supported by ***Global Ph.D. Fellowship* (GPF)** from National Research Foundation of Korea.
- Nov. 2016 – Jul. 2017	***Pacific Northwest National Laboratory* (PNNL)**, Visiting researcher for learning liquid AFM technique.
- Nov. 2018	**2018** *Outstanding Graduate Student Award* given by the department of Energy Engineering.
- Nov. 2018	**2018** *Talent Award of Korea* given by the Ministry of Education of South Korea.

■ List of Publications

1) Cobalt Oxide Encapsulated in C_2N-h_2D Network Polymer as a Catalyst for Hydrogen Evolution

Javeed Mahmood, Sun-Min Jung, **Seok-Jin Kim,** Jungmin Park, Jung-Woo Yoo*, Jong-Beom Baek*
Chemistry of Materials **2015***, 27 (13), 4860-4864

2) Metalated graphene nanoplatelets and their uses as anode materials for lithium-ion batteries

Jiantie Xu, In-Yup Jeon, Hyun-Jung Choi, **Seok-Jin Kim,** Sun-Hee Shin, Noejung Park, Liming Dai, Jong-Beom Baek*
2D Materials **2016***, 4 (1), 014002

3) Understanding of the capacity contribution of carbon in phosphorus-carbon composites for high-performance anodes in lithium ion batteries

Jiantie Xu, In-Yup Jeon, Jianmin Ma, Yuhai Dou, **Seok-Jin Kim,** Jeong-Min Seo, Huakun Liu, Shixue Dou, Jong-Beom Baek*, Liming Dai*
Nano Research **2017**, 10 (4), 1268-1281

4) An efficient and *p*H-universal ruthenium-based catalyst for the hydrogen evolution reaction

Javeed Mahmood, Feng Li, Sun-Min Jung, Mahmut Sait Okyay, Ishfaq Ahmad, **Seok-Jin Kim,** Noejung Park*, Hu Young Jeong*, Jong-Beom Baek*
Nature Nanotechnology **2017**, 12 (5), 441

5) Macroporous Inverse Opal-like Mo_xC with Incorporated Mo Vacancies for Significantly Enhanced Hydrogen Evolution

Feng Li, Xianglong Zhao, Javeed Mahmood, Mahmut Sait Okyay, Sun-Min Jung, Ishfaq Ahmad, **Seok-Jin Kim,** Gao-Feng Han, Noejung Park*, Jong-Beom Baek*
ACS Nano **2017**, 11 (7), 7527-7533

6) Forming a three-dimensional porous organic network via solid-state explosion of organic single crystals

Seo-Yoon Bae, Dongwook Kim, Dongbin Shin, Javeed Mahmood, In-Yup Jeon, Sun-Min Jung, Sun-Hee Shin, **Seok-Jin Kim,** Noejung Park*, Myoung Soo Lah*, Jong-Beom Baek*
Nature Communications **2017**, 8 (1), 1599

7) Defect-Free Encapsulation of Fe^0 in 2D Fused Organic Networks as a Durable Oxygen Reduction Electrocatalyst

Seok-Jin Kim, Javeed Mahmood, Changmin Kim, Gao-Feng Han, Seong-Wook Kim, Sun-Min Jung, Guomin Zhu, James J De Yoreo, Guntae Kim*, Jong-Beom Baek*
Journal of the American Chemical Society **2018**, 140 (5), 1737-1742

8) A Robust 3D Cage-like Ultramicroporous Network Structure with High Gas-Uptake Capacity

Javeed Mahmood,[+] **<u>Seok-Jin Kim,</u>**[+] Hyuk-Jun Noh, Sun-Min Jung, Ishfaq Ahmad, Feng Li, Jeong-Min Seo, Jong-Beom Baek*
Angewandte Chemie International Edition **2018**, 57 (13), 3415-3420

9) Design of Ultrathin Nitrogenated Carbon Nanosheets with Abundant Single Atomic Copper Sites: Boosting Efficient and Stable Oxygen Reduction Catalysis

Feng Li, Gao-Feng Han, Hyuk-Jun Noh, **<u>Seok-Jin Kim,</u>** Yalin Lu, Hu Young Jeong*, Zhengping Fu*, Jong-Beom Baek*
Energy Environmental Science **2018**, 11, 2263-2269

10) Encapsulating Iridium Nanoparticles Inside a 3D Cage-Like Organic Network as an Efficient and Durable Catalyst for the Hydrogen Evolution Reaction

Javeed Mahmood, Mohsin Ali Raza Anjum, Sun-Hee Shin, Ishfaq Ahmad, Hyuk-Jun Noh, **<u>Seok-Jin Kim</u>**, Hu Young Jeong*, Jae Sung Lee*, Jong-Beom Baek*
Advanced Materials **2018**, 1805606

11) Low-Temperature Conversion of Alcohols into Bulky Nanoporous Graphene and Pure Hydrogen with Robust Selectivity on CaO

Gao-Feng Han, Zhi-Wen Chen, Jong-Pil Jeon, **<u>Seok-Jin Kim</u>**, Hyuk-Jun Noh, Xiang-Mei Shi, Feng Li, Qing Jiang*, Jong-Beom Baek
Advanced Materials **2019**, 1807267

12) Oxidative Dehydrogenation of Ethylbenzene into Styrene by Fe-Graphitic Catalysts

<u>Seok-Jin Kim</u>, Gao-Feng Han, Sun-Min Jung, Jong-Pil Jeon, Sun-Hee Shin, Seong-Wook Kim, In-Yup Jeon*, Jong-Beom Baek*
ACS Nano **2019**, 13, 5, 5893-5899

13) Identifying the structure of $Zn-N_2$ active sites and structural activation

Feng Li, Yunfei Bu, Gao-Feng Han, Hyuk-Jun Noh, **<u>Seok-Jin Kim</u>**, Ishfaq Ahmad, Yalin Lu, Peng Zhang, Hu Young Jeong, Zhengping Fu, Qin Zhong, and Jong-Beom Baek
Nature Communications **2019**, Accepted

■ List of Patents

- Application

1) Method of manufacturing an organic ferromagnetism from self-polymerized and the organic ferromagnetism thereof (Republic of Korea: **10-2016-0101981**)
Inventor: Jong-Beom Baek, **Seok-Jin Kim**, Javeed Mahmood

2) CATALYST COMPOSITE, METHOD FOR MANUFACTURING THE SAME AND METHOD FOR PRODUCING HYDROGEN (Republic of Korea: **10-2017-0023472,** International: **PCT/KR2017/006289,** United States of America: **15/769,658**)
Inventor: Jong-Beom Baek, **Seok-Jin Kim**, Feng Li, Javeed Mahmood

3) Nano-sized hydrogen production catalyst utilizing carboxyl group and metal bond and method for manufacturing the same (Republic of Korea: **10-2018-0079671**)
Inventor: Jong-Beom Baek, **Seok-Jin Kim**, Feng Li, In-Yup Jeon

4) Catalyst complex for hydrogen production using 3-dimensional polymer and method for producing the same (Republic of Korea: **10-2018-0094226**)
Inventor: Jong-Beom Baek, **Seok-Jin Kim**, Javeed Mahmood

5) A method for producing graphene and hydrogen using biological shells and alcohols (Republic of Korea: **10-2018-0095561**)
Inventor: Jong-Beom Baek, **Seok-Jin Kim**, Gao-Feng Han

6) Tetrahedral octaamine compound and manufacturing method thereof (Republic of Korea: **10-2018-0118627**)
Inventor: Jong-Beom Baek, **Seok-Jin Kim**, Javeed Mahmood, Ishfaq Ahmad

7) CATALYST COATED ELECTRODE, CATALYST PASTE COMPOSITION
AND METHODS OF MANUFACTURING THEREOF (Republic of Korea: **10-2019-0060139**)
Inventor: Jong-Beom Baek, **Seok-Jin Kim**, Javeed Mahmood

- Registration

1) Diquinoxalino[2,3-a:2',3'-c]phenazine-2,3,8,9,14,15-hexaamine(DPH) Monomer and Method for preparing Catalysis Complex using the same (Republic of Korea: **10-1793453**)
Inventor: Jong-Beom Baek, **Seok-Jin Kim**

■ Conference Presentations

- '*Direct Solvothermal Synthesis of Boron and Nitrogen-Doped Graphene*' in **the 5th A3 Symposium on Emerging Materials: sp² Nanocarbon for Energy 2014** (Tianjin, China, Oct. 18-22. 2014).

- '*Two-Dimensional Network Polymers: Poly(isocyanate) from Self-Polymerizable Monomers*' in **Korean Chemical Society conference** (Go-Yang, Apr. 15-17. 2015).

- '*Encapsulation of Cobalt Oxide in Conjugated Network Polymer as a Catalyst for Hydrogen Evolution*' in **Korean Chemical Society conference** (Dae-Gu, Oct. 14-16. 2015).

- '*Encapsulated Cobalt Oxide in 2D Conjugated Network Polymer as a Hydrogen Evolution Catalyst*' in **Korean Society of Industrial and Engineering Chemistry conference** (Jeju, Nov. 04-06. 2015).

- '*Encapsulated Metal Particle with Robust Two Dimensional Framework Providing Stable High Performance Catalyst*' in **2ⁿᵈ GPF conference** (Seoul, Dec. 22. 2015).

- '*Encapsulation of Iron Particle in Conjugated Two Dimensional Framework as Catalyst for Oxygen Reduction Reaction*' in **Korean Chemical Society conference** (Go-Yang, Apr. 20-22. 2016).

- '*East Asia and Pacific Summer Institutes for U.S. Graduate Students (EAPSI)*' Korea 2016 (Seoul, Aug. 5. 2016).

- '*Encapsulated Cobalt Oxide in Conjugated Network Polymer as a Catalyst for Hydrogen Evolution Reaction*' in **IUPAC-PSK-40** (Jeju, Oct. 04-07. 2016).

- '*Nitrogenated 2D Framework Structures as New Anode Materials for Lithium-ion Batteries*' in **IUPAC-FAPS 2017 Polymer Congress** (Jeju, Oct. 11-13. 2017).

- '*Fe⁰ Cocooned in 2D Organic Networks as a Durable Oxygen Reduction Electrocatalyst*' in **7ᵗʰ EuCheMS Chemistry Congress** (Liverpool, UK., Aug. 26-30, 2018).

- '*Encapsulation of Fe⁰ in 2D Fused Aromatic Networks as an Oxygen Reduction Electrocatalyst*' in **2018 MRS Fall meeting & exhibit** as SESSION CHAIR (Boston, USA., Nov. 25-30, 2018).

Appendix II: Permission from Cited Journal Paper in This Thesis

■ Chapter II. Two-dimensional polymer encapsulated zero-valent iron nanoparticles as a durable oxygen reduction electrocatalyst

Reprinted (adapted) with permission from (Defect-Free Encapsulation of Fe^0 in 2D Fused Organic Networks as a Durable Oxygen Reduction Electrocatalyst, *J. Am. Chem. Soc.* **2018**, *140* (5), 1737-1742). Copyright (2018) American Chemical Society.

■ Chapter III. A Robust 3D Cage-like Ultramicroporous Network Structure with High Gas-Uptake Capacity

Reprinted (adapted) with permission from (A Robust 3D Cage-like Ultramicroporous Network Structure with High Gas-Uptake Capacity, Angew. *Chem. Int. Ed.* **2018**, *57* (13), 3415-3420). © WILEY-VCH Verlag GmbH & Co. KGaA, Weinheim

JOHN WILEY AND SONS LICENSE
TERMS AND CONDITIONS

Apr 28, 2019

This Agreement between Mr. Seok-Jin Kim ("You") and John Wiley and Sons ("John Wiley and Sons") consists of your license details and the terms and conditions provided by John Wiley and Sons and Copyright Clearance Center.

License Number	4577930669197
License date	Apr 28, 2019
Licensed Content Publisher	John Wiley and Sons
Licensed Content Publication	Angewandte Chemie International Edition
Licensed Content Title	A Robust 3D Cage-like Ultramicroporous Network Structure with High Gas-Uptake Capacity
Licensed Content Author	Jong-Beom Baek, Jeong-Min Seo, Feng Li, et al
Licensed Content Date	Feb 27, 2018
Licensed Content Volume	57
Licensed Content Issue	13
Licensed Content Pages	6
Type of use	Dissertation/Thesis
Requestor type	Author of this Wiley article
Format	Print and electronic
Portion	Full article
Will you be translating?	No
Title of your thesis / dissertation	Synthesis of Multidimensional Organic Network Structures and Their Applications to Energy Materials
Expected completion date	Aug 2019
Expected size (number of pages)	115
Requestor Location	Mr. Seok-Jin Kim 50, UNIST-gil, Eonyang-eup Engineering Blvd. 104-708 Ulju-gun, Ulsan 44919 Korea, Republic Of Attn: Mr. Seok-Jin Kim
Publisher Tax ID	EU826007151
Total	0.00 USD

■ Chapter V. Mechanochemically Induced Fe-Graphitic Nanoplatelets as Catalysts for the Oxidative Dehydrogenation

Reprinted (adapted) with permission from (Oxidative Dehydrogenation of Ethylbenzene into Styrene by Fe-Graphitic Catalysts, *ACS Nano* **2019**, 13, 5, 5893-5899). Copyright (2019) American Chemical Society.

Acknowledgement

It's been 9 years since I was 20 years old that I spent time walking around the Gamak-pond. I thought it would be a frog in a well surrounded by mountains, but what I learned and experienced at UNIST gave me access to a bigger world, and it became a place to grow as a scientist who could be compared to the world. During my Ph.D. course, my parents supported me silently. I have not been able to visit them often because I have a lot of shortages, but I'll keep in touch with you and be reborn as a filial son. I would like to present my graduation thesis to my sisters, brothers, relatives, and friends.

By the time I got my Ph.D., I thought I'd be able to realize everything and confidently say I'm an expert in a field, but I think I've come to see more things to learn. And what I realized during my five-year degree was that I couldn't do all of my research or work alone. I would like to express my gratitude to those who have supported me in the last chapter of the paper.

I've been with Professor Baek Jong-beom, who taught me, for seven years since I was an intern. Sometimes he was strict, sometimes like a father, and he corrected my unstable graduate life. Especially, I learned a lot from taking a walk during lunch time at PNNL. Encouraging me not to be daunted by the lonely and lonely life of America and guiding my thesis, I think, has changed a lot in this important period of my life. Thanks to him, I came across a new world and I was able to run with a wide range of eyes. Professor Myoung Soo Lah, who evaluated my graduation, and with his keen insight and deep advice, he taught me the right attitude of a researcher, and Professor Hoi Ri Moon, who has always been warmly greeted and sincerely encouraged by me since I was an undergraduate, taught me the right attitude of an educator. Professor Guntae Kim taught me how to get and deliver creative ideas, and Professor In-Yup Jeon who was CDCOF research lab member taught me passionate research life and leadership.

I would also like to thank the PNNL's labs. Professor Jim De Yoreo, who gave full support to all of my PNNL life, has taught a lot about what a respected scientist has the attitude. Dr. Jinhui, who often spent half a day with me who knew nothing about AFM, Dr. Shuai, who took me to the emergency room when I was sick and greeted me at the MRS Society with a pleasant greeting, Dr. Yongsoon Shin, who gave me a lot of advice over lunch with my advisor professor, friends Jiajun and Guomin, who agonized over AFM and talked deeply about career paths, Dr. Hongkyung Lee, who taught me how to draw my thesis figures and traveled with me, Dr. Hyung-Seok Lim, who has always sincerely consulted my concerns, and Dr. Jaewon Lee, who has made me proud of my research in materials science.

And CDCOF members, Dr. Seo-Yoon, who was the first to welcome me, Dr. Hyun-Jeong, who pioneered electrochemistry in our lab, Jongyeol, who gave me lots of advice from the lab, Dr. Sun-Min, who was always surprised, Dr. Jeong-Min, who was responsible, missed 11th-year Sun-Hee, Dr. Javeed, who was the best friend and pillar, Ahyoung Kim, an intern alliance who works hard in Illinois, Ishfaq, who gave praise and support every day, Many-Knowledgeable Yoon-Kwang, Dancing god-dancing king, Soo-Young, Lab master, Haman Kardon, Jong-Pil, stylish Young Hyun, a sportsman in a neighboring village, Do Hyung, Boo-Jae who helped out at every important moment, and Lab-SCV Hyuk-Jun, Seong-Wook, who got lots of nagging but followed well, tall Hyun Yeol, and Won Jun, who was curious, and to many cute interns who are worried about their studies, Dr. Dongwook Kim who is always support me, to anyone I may have omitted, my apologies: I appreciated your efforts nonetheless. I will walk on the path of learning with the attitude of '三人行 必有我師焉 (When three people walk down the street, there must be a teacher among them) ' to be a respected Ph.D.

May 2019,
Seok-Jin Kim

감사의 글

20살 때부터 가막못을 거닐며 시간을 보낸 지 어느덧 9년이라는 시간이 지났습니다. 산으로 둘러 쌓여 우물 안 개구리가 될 거라 생각했지만, UNIST에서 배우고 경험한 것들은 더 큰 세상을 접하게 해주었고, 세계와 견줄 수 있는 과학자로 성장할 거름이 되어주었습니다. 박사학위를 진행하는 동안 묵묵히 응원해주신 부모님, 제가 부족한 것이 많아 자주 찾아 뵙지 못했지만 앞으로는 자주 연락 드리며 효자로 거듭나겠습니다. 큰누나, 작은누나, 자형들, 친척, 친구들에게도 졸업 논문이나마 감사함을 표하고 싶습니다.

박사 학위를 받을 때쯤이면 만물을 깨닫고 한 분야의 전문가라고 자신 있게 말할 수 있을 것 같았지만 오히려 배워야 할 부분들을 더 많이 보이게 된 것 같습니다. 5년의 학위 과정동안 깨달은 점이 있다면, 모든 연구나 일이든 혼자 힘으로는 할 수 없다는 것이었습니다. 연구를 하면서 저에게 든든한 버팀목이 되어주고 아낌없이 지원해주신 분들께 논문의 마지막 장에 감사의 말을 전하고자 합니다.

저를 지도해주신 백종범 교수님, 아무것도 모르던 학부생 시절 다짜고짜 인턴으로 찾아 뵌 지가 7년이 흘렀습니다. 때로는 엄격하게, 때로는 아버지처럼 챙겨 주시며 저의 불안정했던 대학원 생활을 바로잡아 주셨습니다. 특히, PNNL에서 함께 점심시간동안 산책을 하며 많은 것을 배웠습니다. 외롭고 쓸쓸했던 미국생활에 기죽지 않도록 격려해 주시고 논문을 한 문장, 한 문장 지도해주신 것이 제 인생의 중요한 시기에 많은 변화를 가져온 것 같습니다. 교수님 덕분에 새로운 세계를 접하게 되었고, 넓어진 안목과 함께 달려올 수 있었습니다. 그리고 제 졸업 심사를 평가해주신 나명수 교수님, 예리한 통찰력으로 연구하시는 모습과 깊이 있는 조언들로 저에게 올바른 연구자의 태도를, 문회리 교수님께선 제가 학부생 때부터 항상 따뜻하게 인사를 받아 주시며 진심 어린 격려를 해주시는 모습으로 올바른 교육자의 자세를 가르쳐 주셨습니다. 김건태 교수님께선 창의적인 아이디어를 얻고 전달하는 방법을, CDCOF연구실 맥가이버 '인엽이형' 전인엽 교수님으로부터 열정적인 연구 생활과 리더십을 배울 수 있었습니다.

그리운 PNNL의 연구실 분들에게도 감사의 말을 전해드립니다. 연구생활의 모든 것을 전폭적으로 지지해주신 Jim De Yoreo 교수님, 많은 이들에게 존경받는 과학자는 어떤 면모를 갖추고 있는지 많은 것을 배울 수 있었습니다. AFM에 대해 아무것도 모르던 저와 함께 자주 반나절의 귀중한 시간을 보내며 가르쳐준 Jinhui박사님, 아플 때 응급실까지 태워주고 MRS학회에서 반갑게 인사한 Shuai박사님, 함께 AFM으로 고민하고 진로에 대해 깊은 얘기를 나눈 친구 Jiajun과 Guomin, 지도교수님과 함께 점심시간 산책을 하며 많은 조언을 해 주신 신용순 박사님, 논문 그림 그리는 방법을 가르쳐주고 여행도 함께한 이홍경 박사님, 항상 제 고민을 진진하게 상담해 주시던 몸짱 임형석 박사님, 재료과학 연구에 자부심을 느끼게 해 주신 이재원 박사님께도 감사의 말을 전합니다.

그리고 가족같이 함께 했던 CDCOF 멤버들, 가장 먼저 반갑게 맞이해준 서윤누나, 전기화학을 개척하고 가신 현정누나, 실험실에 애정을 갖고 관리해준 민정누나, 옆에서 많

은 조언을 해줬던 종렬이형, 항상 오른쪽 옆자리를 지키며 도와준 선민누나, 책임감 강한 정민누나, 그리운 11동기 선희, 최고의 친구이자 기둥이 되어 준 javeed, 일리노이에서 열공하는 인턴동맹 아영이, 매일 칭찬과 응원을 해준 ishfaq, 박학다식한 윤광이형, 춤신춤왕 수영누나, 랩마스터, 함안카돈 별명부자 종필thl, 스타일리쉬 트렌디가이 영현이형, 이웃사촌 만능 스포츠맨 도형이형, 중요한 순간마다 발벗고 도와준 부재형, 연구실 SCV혁준이, 잔소리 많이 했지만 잘 따라와준 성욱이, 장신 현열이, 호기심 많은 원준이, 그리고 학업에 고민 많은 귀염둥이 인턴 학생들, 같은 연구실은 아니지만 제 연구에 큰 도움을 주신 김동욱 박사님과 여기서 언급 못 드린 모든 분들에게도 부끄럽지 않은 박사가 되도록 '삼인행 필유아사언(三人行 必有我師焉)' 자세로 배움의 길을 걷겠습니다.

2019년 푸른 5월,
김석진 드림